THE ZINC/BROMINE FLOW BATTERY:

FUNDAMENTALS AND NOVEL MATERIALS FOR TECHNOLOGY ADVANCEMENT

A thesis submitted in partial fulfilment of requirements for the degree of

Doctor of Philosophy

by

Gobinath Pillai Rajarathnam

The University of Sydney

Faculty of Engineering & Information Technologies

School of Chemical & Biomolecular Engineering

2016

Supervisor: Prof. Anthony Vassallo

To Amma and Appa.

Summary

Redox flow batteries are a promising solution for solving intermittency challenges and increasing uptake of renewable power sources such as wind and solar. In particular, zinc/bromine batteries are an attractive option for large-scale electrical energy storage due to their relatively low cost of primary electrolyte and high theoretical specific energy of 440 Wh kg^{-1} of zinc bromide electrolyte. However, inefficient materials of construction hinder practical utilization of this capability and reduce power delivery. Challenges include inefficient electrodeposition and stripping in the zinc half-cell.

The work presented in this thesis aims to overcome these limitations by providing an understanding of the fundamental physical and electrochemical processes governing interactions within the bulk electrolyte and at the electrode–electrolyte interface. Suitable alternative materials to improve system performance are developed *via* electrochemical investigations (voltammetry, impedance spectroscopy), physical characterization (scanning electron microscopy, X-ray diffraction) and molecular modelling (density functional theory).

It is shown that conventional chloride-based supporting electrolytes employed to maintain electrolyte conductivity during charging significantly influence the morphology of zinc electrodeposits generated. High chloride concentration causes removal of zinc from the bulk, causing coulombic losses in the system. Following from this point, it is shown that sulfates, phosphates or even a higher proportion of bromides, are suitable alternative supporting electrolytes capable of improving performance. Single-halide type tetrahedral zinc complexes exist in conventional electrolytes, and a previously unreported Raman vibrational band at 220 cm^{-1} is identified and assigned to the $[ZnBr_2Cl(H_2O)]^-$ complex.
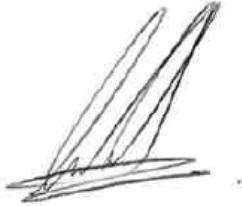
Alternative ionic liquid additives are also investigated, and it is proven that while they are conventionally considered to be spectators in the zinc half-cell, the reality is in fact otherwise due to the effects of their chemical structures. Studies using hybrid ionic liquid mixtures indicate that each half-cell benefits from the use of different compounds. Cost is an important consideration for battery system, and adding expensive ionic liquids would increase unit electrolyte costs, however improved performance could lead to a lower normalized cost per kW and kWh of the battery. It is expected that the approaches and findings presented in this thesis contribute towards an increased understanding of Zn/Br systems, aiding and guiding the future search for novel materials to further improve this technology.

Statement of Originality

I hereby declare that the intellectual content of this thesis is my original work unless stated otherwise, and that all assistance received in preparing this thesis and sources have been acknowledged. No part of this work has been submitted to any institution for the award of a degree. Chapter inputs from collaborative work are outlined as follows (as well as acknowledged in the next section):

- Chapter 1: All work carried out by the author under the supervision of Prof. Anthony Vassallo.

- Chapter 2: All work carried out by the author under the supervision of Prof. Anthony Vassallo, with the use of some benchtop full-cell experimental data provided by Martin Schneider (School of Chemical and Biomolecular Engineering, The University of Sydney).

- Chapter 3: All work carried out by the author under the supervision of Prof. Anthony Vassallo and Dr. Alejandro Montoya (School of Chemical and Biomolecular Engineering, The University of Sydney).

- Chapter 4: All work carried out by the author under the supervision of Prof. Anthony Vassallo.

- Chapter 5: All work carried out by the author under the supervision of Prof. Anthony Vassallo, with the use of some Raman experimental data provided by Matthew Suprawinata (School of Chemical and Biomolecular Engineering, The University of Sydney).

- Chapter 6: All work carried out by the author under the supervision of Prof. Anthony Vassallo using electrolytes provided, and SEM images taken, by Max Easton (School of Chemistry, The University of Sydney).

- Chapter 7: All work carried out by the author under the supervision of Prof. Anthony Vassallo.

- Chapter 8: All work carried out by the author under the supervision of Prof. Anthony Vassallo.

Gobinath Pillai Rajarathnam

8th July 2016

List of Publications

This thesis contains work which has been accepted or submitted for publication and in external conferences, and edited/expanded for use in the following chapters:

Chapter 1**:**

- G. P. Rajarathnam and A. M. Vassallo, "Storing Electricity", Chapter 1, The Zinc/Bromine Flow Battery: Materials Challenges and Practical Solutions for Technology Advancement, 1st ed., p. 97, Springer Singapore, Singapore, (2016).

Chapter 2**:**

- G. P. Rajarathnam and A. M. Vassallo, "Description of the Zn/Br RFB System", Chapter 2, The Zinc/Bromine Flow Battery: Materials Challenges and Practical Solutions for Technology Advancement, 1st ed., p. 97, Springer Singapore, Singapore, (2016).

Chapter 3**:**

- G. P. Rajarathnam, A. Montoya, and A. M. Vassallo, The Influence of a Chloride-Based Supporting Electrolyte on Electrodeposited Zinc in Zinc/Bromine Flow Batteries, *Journal of The Electrochemical Society* (2016). *Manuscript submitted*.

- G. P. Rajarathnam, A. Montoya, and A. M. Vassallo, The Interactions Between Chlorides and Zn (001) Surfaces in Zinc/Bromine Flow Battery Electrolytes, in *229th Meeting of the Electrochemical Society*, The Electrochemical Society, San Diego, California, USA (29th May–2nd June 2016).

Chapter 4**:**

- G. P. Rajarathnam, M. Schneider, X. Sun, and A. M. Vassallo, The Influence of
  Supporting Electrolytes on Zinc Half-Cell Performance in Zinc/Bromine Flow
  Batteries, *Journal of The Electrochemical Society*, **163**, A5112–A5117 (2016).

Chapter 5**:**

- G. P. Rajarathnam, M. Easton, M. Schneider, A. Masters, T. Maschmeyer, and A.
  M. Vassallo, The Influence of Ionic Liquid Additives on Zinc Half-Cell
  Electrochemical Performance in Zinc/Bromine Flow Batteries, *RSC Advances*, **6**,
  27788–27797 (2016).

- G. P. Rajarathnam, M. Schneider, M. E. Easton, and A. M. Vassallo,
  Electrochemical Characterization and Comparison of Three Bromine-
  Sequestering Agents for Zinc/Bromine Flow Battery Applications (Paper No.
  3133088), in *APCChE 2015 Congress incorporating Chemeca 27 Sept – 01 Oct
  2015*, Melbourne, Australia (2015).

- G. P. Rajarathnam, M. Schneider, M. E. Easton, and A. M. Vassallo,
  Electrochemical Performance of Three Novel Bromine-Sequestering Agents for
  Zinc/Bromine Flow Battery Electrolytes, in *228th Meeting of the Electrochemical
  Society*, The Electrochemical Society, Phoenix, Arizona, USA (2015).

Chapter 6**:**

- G. P. Rajarathnam, M. D. Suprawinata, and A. M. Vassallo, Raman Analysis of
  Electrolyte Speciation in Zinc/Bromine Flow Batteries, in *Oz Energy Future
  Conference*, University of New South Wales, Sydney, Australia (4-6th July
  2016).

Chapter 7**:**

- <u>G. P. Rajarathnam</u>, and A. M. Vassallo, Half-Cell Electrochemical Performance of Hybridized Ionic Liquid Additives for Zinc/Bromine Flow Battery Applications, in *229th Meeting of the Electrochemical Society*, The Electrochemical Society, San Diego, California, USA (29th May–2nd June 2016). *Manuscript accepted.*

Chapter 8**:**

- <u>G. P. Rajarathnam</u> and A. M. Vassallo, "Strategies for Studying and Improving the Zn/Br RFB", Chapter 6, The Zinc/Bromine Flow Battery: Materials Challenges and Practical Solutions for Technology Advancement, 1st ed., p. 97, Springer Singapore, Singapore, (2016).

Authorship Attribution Statement

In addition to the statements above, in cases where I am not the corresponding author of a published item, permission to include the published material has been granted by the corresponding author.

Gobinath Pillai Rajarathnam

8th July 2016

As supervisor for the candidature upon which this thesis is based, I can confirm that the authorship attribution statements above are correct.

Prof. Anthony Vassallo

8th July 2016

Author's Note

I have seen some authors choose to add a witty quote at the beginning of their thesis, while others prefer to go with a wise saying. Personally, I find myself inclined to include one or the other as well. However, I believe it would be more meaningful to share something which attempts to explain part of the strong motivational force I feel to pursue my chosen field of research.

When I first started working with flow batteries in August 2013 for my PhD, I took it to be just an interesting project that happened to be available and an opportunity to expand my engineering knowledge and skills via research. I soon learnt the ability to harness and store electricity is one of the most powerful tools we have at our disposal to quite literally change the world around us.

Below is a brief essay I wrote one afternoon in May 2015 as part of an entry for an energy storage conference scholarship. I'm including this here as a reminder to myself, and to share with the reader, on the importance of each and every individual's contribution towards improving the world as we know it.

"A vision and role for energy storage in our shared future"

Knowledge sees its full potential when it is used to improve the lives of those who need it most. On the most fundamental level, it is unfair that we essentially live in a world where the gap between those who live with almost everything and those who subsist on almost nothing are in an ever-widening drift. There are many intrinsically-linked reasons for such a disparity, and I believe the lack of readily-available and reliable access to energy – regardless electricity, heat, light or otherwise – is a strong contributing factor. I strongly believe it is possible to alleviate, and even turn around, the end result of these aspects via technology – specifically, energy storage.

My vision for energy storage is shared by many others in the scientific and wider communities: the ability to economically harness, store and use energy in its various forms will play an important role in the shift towards a promising solution to the triple bottom line issues which currently plague sustainable progress at a global level – regardless first- or third-world country. Social, economic and environmental benefits are all possible, and practical, with increased funding to develop and test new and improved ways of storing energy.

We can improve the lives of poor farmers who can adopt better farming practices, leaving their children free to attend school instead of having to toil in the fields because their parents cannot afford to pay for additional labor. Rural clinics can afford to stock medicine requiring refrigeration and fewer people will suffer from diseases which should not be allowed to run rampant in this day and age of impressive technology. People living in earthquake-prone areas, or those where other natural disasters frequently hit, need not continue living in devastation because power lines become cut-off. Emergency response teams leading disaster-relief efforts will be able to deploy telecommunications, triage and other essential services within minutes of arrival at incident sites.

Overall, the possibilities to improve the quality of life across the board are effectively limitless, and this is all made possible with the intelligent push towards and use of saving energy until we need to use it at the right moment. In a world where each individual aspires to be different from the rest, I genuinely hope my vision for our shared energy future is not unique. We do not have the luxury of time or capacity for selfishness in this matter.

Acknowledgements

Doing a Ph.D. has been one of the best decisions of my life, and I would like to thank all the people who have helped make this an enjoyable and productive journey.

I will forever be grateful to my supervisor Prof. Tony Vassallo for being an excellent role model. His guidance and creation of numerous opportunities for me to grow as a researcher, as well as his invaluable advice and open door policy, have been instrumental in building my confidence towards technological research and development. I genuinely look forward to using my skills and knowledge to help improve the lives of those with the greatest need.

Contents

List of Tables

xxi

List of Figures

List of Abbreviations

ac: Alternating current

BSA: Bromine sequestration agent

cNEB: Climbing image nudged elastic band (used in DFT calculations)

COP: Cross-over potential

CV: Cyclic voltammetry

DC: Differential capacitance

DFT: Density functional theory

DP: Deposition potential

EDL: Electrical double-layer

EEI: Electrode–electrolyte interface

EES: Electrical energy storage

EIS: Electrochemical impedance spectroscopy (ac impedance spectroscopy)

FWHM: Full width at half maximum

HDPE: High-density polyethylene

IL: Ionic liquid

LSV: Linear sweep voltammetry

MEMBr: N-methyl N-ethyl morpholinium bromide (BSA)

MEPBr: N-methyl N-ethyl pyrrolidinium bromide (BSA)

ML: Monolayer (units of surface coverage)

MP: Methfessel–Paxton (smearing, used in DFT calculations)

NOP: Nucleation overpotential (difference between DP and COP)

OCP: Open-circuit potential

OCV: Open-circuit voltage

PAW: Projector-augmented wave

QBr: Quaternary bromide (ammonium salt, used as BSA)

SCF: Self-consistent field (used in DFT calculations)

SEM: Scanning electron microscopy

SHE: Standard hydrogen electrode

SoC: State-of-charge (available energy level in a battery, %)

RFB: Redox flow battery

VASP: Vienna Ab-initio Simulation Package (DFT software)

WH: Williamson–Hall (method for determining crystal size *via* XRD peak analysis)

XRD: X-ray diffraction

ZBB: Zinc/bromine battery

ZHC: Zinc-halide complex

1. Storing Electricity

1.1. Chapter introduction

This chapter presents an overview of the need for energy storage at the utility-scale. The role and attractiveness of redox flow battery systems in enabling grid-integration of renewable energy sources to resolve intermittent flux issues and resolve challenges against uptake faced by such sources is detailed herein. This is done *via* a general introduction of flow battery technology, with highlights of different types of established as well as recently developed redox flow battery systems. The current technological and commercial status of the Zn/Br system is discussed. This leads into an introduction of the various potential avenues of investigation to improve the performance and thus the commercial viability of the Zn/Br flow battery. A case is made for the need to adopt novel design approaches and actively seek better materials of construction for the next generation of Zn/Br batteries. Finally, the organizational structure of this thesis is explained with regard to fundamental studies and operational improvements to both zinc and bromine half-cells.

1.2. Energy storage and flow batteries

Incorporating renewable power sources into the existing electricity grid is a challenge, due to the variable nature of many renewable sources of power such as solar photovoltaics and wind power generators. The importance of electrical energy storage (EES) to alleviate this issue[1,2] has prompted many reviews and analyses of storage options[3–8] and work using net energy analysis to understand and predict the outcomes from integrating EES with renewables.[9] The potential of battery technology as a solution to this problem is well understood.[10] Among the recently most-downloaded

articles from the Journal of Power Sources[11] alone, almost two out of every three articles downloaded in a 90-day period are related to lithium-based batteries (e.g. Li-ion) and studies carried out to improve the technology, indicating sustained popularity in that area among many research groups around the world. Nevertheless, many alternative battery technologies potentially offer lower costs in the long term, such as redox flow batteries (RFBs), especially where high specific energy is not required, such as in stationary, grid-connected battery storage.

Redox flow batteries belong to a class of secondary rechargeable batteries that operate based on the redox reactions of electrochemically active species present in an electrolyte solution. They can be charged by a range of power sources and subsequently discharged to power external loads. RFBs have the potential to solve utility-scale EES issues in order to achieve good integration of intermittent renewable power sources (e.g. solar, wind) with existing grid networks *via* load-levelling[12] and even by deployment in remote telecommunication sites.[13] Improvements in RFB technology would also facilitate the rapid decentralization of renewable energy production and contribute to solving generation and distribution issues surrounding rural electrical power systems.[14] Qualities such as ease of scalability, modularity of system components and high degree of operational flexibility[15] serve to increase the attractiveness of RFBs for utility-scale EES.

In recent years, many varieties, combinations and generations of RFBs have been proposed, reviewed and/or further developed, including all-vanadium (all-V)[16] and other V-based systems,[17] hydrogen/bromine (H/Br),[18,19] all-chromium (all-Cr),[20] all-cobalt,[21] zinc/cerium (Zn/Ce),[22–25] sodium/iodine (Na/I),[26] all-copper (all-Cu),[27–29] iron/air (Fe/air),[30] zinc/polyiodide,[31] iron/bromine (Fe/Br),[32] polythiophene,[33] aqueous-based lithium/bromine (Li/Br),[34] and even an iron/vanadium (Fe/V) system

operating on multiple redox couples.[35] More recently, a metal-free organic–inorganic aqueous RFB using 9,10-anthraquinone-2,7-disulphonic acid and the bromine–bromide redox couple has been proposed and tested,[36–38] together with a screening study of promising molecules for use within the system.[39] However, the current high manufacturing, operating and maintenance costs of some potential RFBs reduce their attractiveness for large-scale EES. Despite these potential challenges, the zinc/bromine (Zn/Br) RFB has many benefits that make it attractive for utility-scale EES if scale-up and manufacturing can deliver a competitively priced battery. It is acknowledged that market forces and government policies also play a significant role in the uptake and widespread implementation of EES technology, with recent valuation work in the area,[40] but this aspect lies outside the scope of the present work and is left to another technical review.

1.3.Present status of Zn/Br systems

There is significant scope and warrant for focus on developing the next generation of zinc/bromine batteries (ZBBs) to reach their commercial potential. However, ZBBs currently receive less attention than other RFBs, despite being one of the main systems to undergo heavy development for about two decades beginning in the 1970s.[41–50] Well-known issues, such as dendrite formation on the zinc electrode during electroplating leading to electrical shorting, as well as corrosion of electrodes and battery casings due to bromine seeping into the materials of construction, are now largely addressed. Other problems persist, however, such as modest operational efficiency, relatively short battery cycle lifespan and high potential for self-discharge if stored in the charged state for an extended period of time.[51] By July 2015, commercially available Zn/Br RFB units were manufactured and sold by these four companies around the world: RedFlow Ltd.,[52] Premium Power Corp.,[53] Primus

3

Power[54,55] and ZBB Energy Corp..[56] On the basis of technical information obtained from the manufacturers, Zn/Br batteries have a specific energy of approximately 60–85 Wh kg^{-1},[52,56] which is less than 20% of their theoretical maximum specific energy of 440 Wh kg^{-1}.[57,58] Furthermore, these values are still less than the 100 Wh kg^{-1} target set by industry at the turn of the century for improvement within a decade.[49] This has significant implications for technology uptake, as higher specific energies are directly related to lighter batteries capable of storing more energy. Improvements to the practical specific energy of Zn/Br RFB systems, even to 180 Wh kg^{-1}, which is more than twice that of the best currently available commercial systems, still only utilizes about 40% of the maximum theoretical specific energy possible for such systems.

One of the great attractions of the ZBB as a strong candidate for low-cost EES is the potentially low cost of electrolyte. Specifically, it can be expected that, based on the price of raw materials, ZBBs would incur lower overall production costs than other, more expensive RFBs such as the all-vanadium battery. Both bromine and zinc are commodity chemicals, already manufactured at industrial scale. Although both zinc and bromine prices fluctuate, the price of Br$_2$ is approximately US$1620 per ton (from 2006 prices)[59] and zinc has a spot price of about US$2050 per ton,[60] after adjustment for inflation.[61] Recent calculations in the context of the North American market suggest that ZBBs currently have capital costs comparable to all-V systems on the basis of power capacity, whereas the latter offer slightly higher energy capacity for the same capital.[62]

Based on the price of raw materials stated above, a 3 M ZnBr$_2$ electrolyte results in an approximate cost of US$875 per ton. Consequently, the specific energy cost for ZBBs operating at a practical upper limit of 85 Wh kg^{-1} is approximately US$74 kWh^{-1}. The overall value is likely to be significantly higher when the costs of construction

materials, labor, transportation, secondary electrolytes, additional additives and other associated overhead costs are factored in. Independent studies in 2012 of annual storage costs based on life-cycle analysis calculated that Zn/Br RFBs have unit storage costs of US\$1300 kWh^{-1} and future replacement costs of US\$390 kWh^{-1} that are higher than costs for all-V (US\$900 kWh^{-1} and US\$270 kWh^{-1}, respectively).[63] The cost of Li-ion systems has significantly reduced over the past 2 years, from a storage cost of US\$900 kWh^{-1}[63] down to a range of US\$200–700 kWh^{-1}.[64] It is expected that the costs of commercial ZBBs will further decrease in the near future with the rapid drive towards low-cost materials and manufacturing methods in countries such as China.[65] There are also important design, manufacturing and other considerations involved prior to promoting the widespread uptake of this technology.[66]

1.4. The future of Zn/Br RFB research

The key to moving forward with RFB research lies in the fact that there is allowance for some degree of separation between power and energy components in the same system.[51] However, this capability is complicated for the case of ZBBs as the energy of the system can only be harnessed effectively in the presence of a highly efficient power delivery configuration. Electrochemical energy possessed by the ZBB is based on the electrolyte, whereas power delivery is dependent on the operating behavior and efficiency of the electrode–separator cell stack. In particular, bromine-side electrochemical kinetics are rate-limiting compared to the zinc-side reaction, and thus significantly determine battery performance.

Subsequent research, either directly or indirectly related to ZBBs following major work carried out in the 1970s and early 1980s, has been mostly focused on materials development, such as proposing and identifying suitable complexing agents for bromine sequestration in ZBBs[67] to vanadium-based RFBs,[68] as well as identifying

5

suitable electrolytes that improve ZBB operation.[69] Although there have also been studies testing wide ranges of electrode materials and design methods, the relative volume of publications suggests that the prime focus has been on comparing multiple batches of modified electrolytes with slight variations in compositions between each, primarily because the electrochemistry of electrolyte solutions is typically easier to study than modifications to electrode–separator cell stack design configuration. This explains why the cell stack is usually the most expensive part of the battery unit,[51] due to both the cost of electrode and membrane separator materials required for construction and the difficulty in manufacturing them for that purpose.

A number of publications within the last decade have reviewed the status of a wide range of RFBs and rechargeable batteries in general,[15,51,70–75] as well as batteries for specific systems, such as the all-V RFB.[16,76–78] However, there has been no dedicated general or technical review of ZBBs for more than two decades. To this end, a technical review book on the topic and technology has been prepared and published.[79] The purpose of this book was to identify, thematically categorize, discuss and analyze in detail the physical and electrochemical challenges holding back Zn/Br RFB technology from evolving into the next generation with improved practical specific energy and performance, "smarter" materials of construction and optimized operation *via* various design and control engineering strategies. Insights provided from the wide range of literature surveyed in this book were applied to pinpoint the barriers to future development of ZBB technology and to formulate practical investigative pathways in order to renew efforts towards developing and optimizing the next generation of ZBBs. In particular, the objective was to identify experimental avenues geared towards developing solutions that are highly practical and can be implemented immediately to

have significant impact on ZBB development in the short term. These discussions are presented in various chapters across the book.

1.5. Problem statement and thesis question

It is necessary to improve Zn/Br RFB performance (specific energy, power, operating efficiencies, etc.) in order to increase commercial competitiveness of such systems and viability for utility-scale electrical energy storage. However, current strategies focusing on electrode functionalization are insufficient to significantly improve the state of this technology, and operational benefits can be achieved by the strategic use of electrolyte additives. The work presented in this thesis aims to answer the following question:

"What are some beneficial compounds for Zn/Br battery performance, and what are their roles and influences in achieving this effect?"

1.6. Organization of this thesis

The technical gaps and challenges currently facing Zn/Br RFB improvement can be broadly classified and viewed as some focal points that can be used as a base for ZBB research work to offer potentially high likelihood of quick and significant improvements. First and foremost, there is an imperative to obtain and confirm a good understanding of the underlying electrochemistry and physical processes governing ZBB operation. This is especially important for the electrode–electrolyte interface (EEI) because that is where charge transfer occurs. On the basis of knowledge of such processes, it is then possible to employ novel materials to boost the occurrence and rate of desired reactions while suppressing undesirable side reactions. It is also important to understand the impacts of various electrolyte additives on ZBB operation, whether as supporting electrolytes or for bromine sequestration. Non-uniformity of

zinc electrodeposition and de-plating, specifically dendritic phenomena, during the charging and discharging phases are indicative of uneven activity along electrode surfaces and constitute an issue requiring specific solutions tailored to the ZBB operating environment. These aspects of technology development are studied *via* a range of electrochemical and molecular modelling techniques – such as impedance spectroscopy and periodic density functional calculations – to understand and characterize the influences of novel/alternative materials.

To this end, this thesis is organized into the following seven chapters:

- Chapter 1: An introduction to the need and challenges of energy storage, and the viability of flow batteries as a potential solution.

- Chapter 2: Operational details of the Zn/Br system, including detailed descriptions of the system components and reviewing previous work of each aspect.

- Chapter 3: Experimental characterization and molecular modelling studies to understand the influence of chloride-based supporting electrolytes on electrodeposited zinc obtained in the zinc half-cell during the ZBB charging process.

- Chapter 4: Investigating and comparing the use of alternative supporting electrolytes against the conventional chloride-based option in the zinc half-cell.

- Chapter 5: Identifying the type and relative proportion of zinc complexes in conventional electrolytes, including Raman vibrational assignment of a previously unreported complex.

- Chapter 6: Identifying the roles and influences of conventional and alternative ionic liquids (intended for bromine-sequestration purposes) on zinc half-cell performance.

- Chapter 7: Studying the behavior of zinc and bromine half-cells when utilizing electrolytes containing hybridized ionic liquid formulations (for bromine-sequestration purposes), together with a normalized cost-benefit analysis of the resultant impacts on electrochemical performance.

- Chapter 8: Overall conclusions and recommendations for future work based on the findings from investigations presented in this thesis, as well as a discussion on the outlook of Zn/Br RFB technology.

2. Description of the Zn/Br RFB System

2.1. Chapter abstract

In order to make beneficial changes to the Zn/Br flow battery system, it is necessary first to understand its present structure and functional status, including the level of performance for typical systems, the operating mechanisms as well as the conventional materials and methods of construction. The previous chapter introduced and discussed the need for reliable large-scale electrical energy storage and the role of redox flow batteries for such purposes. This chapter describes the physical architecture of the Zn/Br system (i.e. electrode stack, membrane separator, electrolyte flow schematic), as well as the conventional electrolyte solution employed and the dominant chemical redox reactions occurring during charge and discharge processes at each electrode. Design considerations are detailed, such as the safe storage and treatment of bromine evolved, together with important operating practices such as tracking state-of-charge. Finally, electrochemical and overall operational performance characteristics are discussed with regard to maximizing the specific energy of the Zn/Br flow battery and scaling-up next-generation systems from benchtop testing to commercial use.

2.2. Physical architecture

The Zn/Br redox flow battery (RFB) is a modular system comprising a cell stack containing functional electrodes attached to current collectors (separated *via* membranes), electrolyte storage tanks/reservoirs, delivery pumps and pipes. The RFB relies on the electrolyte circulation system to deliver electrochemically active species to electrode surfaces in order to achieve charge transfer and cause electrical current to flow. A simple Zn/Br unit cell is illustrated in Figure 2-1, with multiple such cells combined in series to create a practical battery.
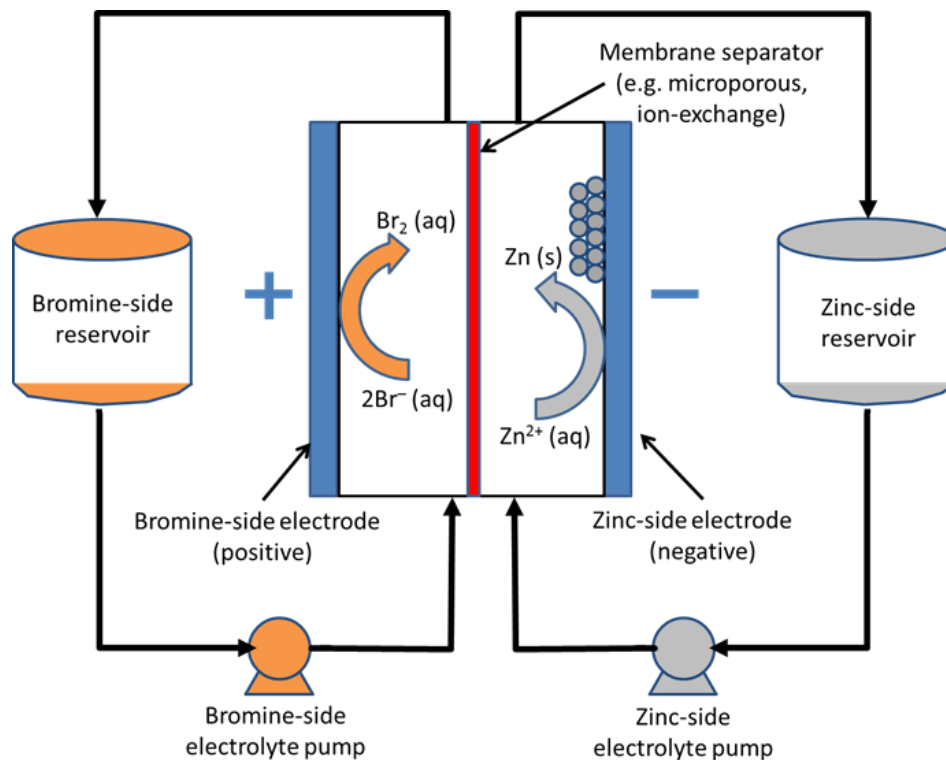
Figure 2-1. A simple Zn/Br unit cell (with electrolyte reservoirs and pumps) during charging process, with positively polarized bromine-side and negatively polarized zinc-side electrodes.

2.3. Electrolyte composition

The main electrolyte used in zinc/bromine batteries (ZBBs) is zinc bromide ($ZnBr_2$) dissolved in water to form an aqueous solution, with the same formulation being used in circulatory loops servicing both the cathode and anode during operation. $ZnBr_2$ is the primary electrochemically active species that interacts with the electrodes to participate in charge-transfer reactions that allow the system to function as an energy storage device. The $ZnBr_2$ present is typically of high concentration, ranging between 1–3 M,[45] with the possibility of even higher concentration up to 4 M.[41] Significant variation in this amount is a direct result of the stage of the charge/discharge cycle at which the battery is, with the concentration decreasing significantly as charging progresses and Zn^{2+} is plated-out while Br^- is oxidized to Br_2, then climbing back up again as the battery is discharged and the original $ZnBr_2$ concentration is restored.

11

A potential–pH (Pourbaix) diagram for a 2.5 M ZnBr$_2$ primary electrolyte solution was constructed using OLI Studio software (version 9.2, OLI Systems, Inc.) and is presented in Figure 2-2. The Pourbaix diagram follows on from the previous point about zinc plating out and provides an illustration linked to the electrode reactions subsequently presented and discussed in section 2.4. The stability ranges of zinc species provide an explanation towards how species limitations influence the electrochemical windows used in Zn/Br batteries.
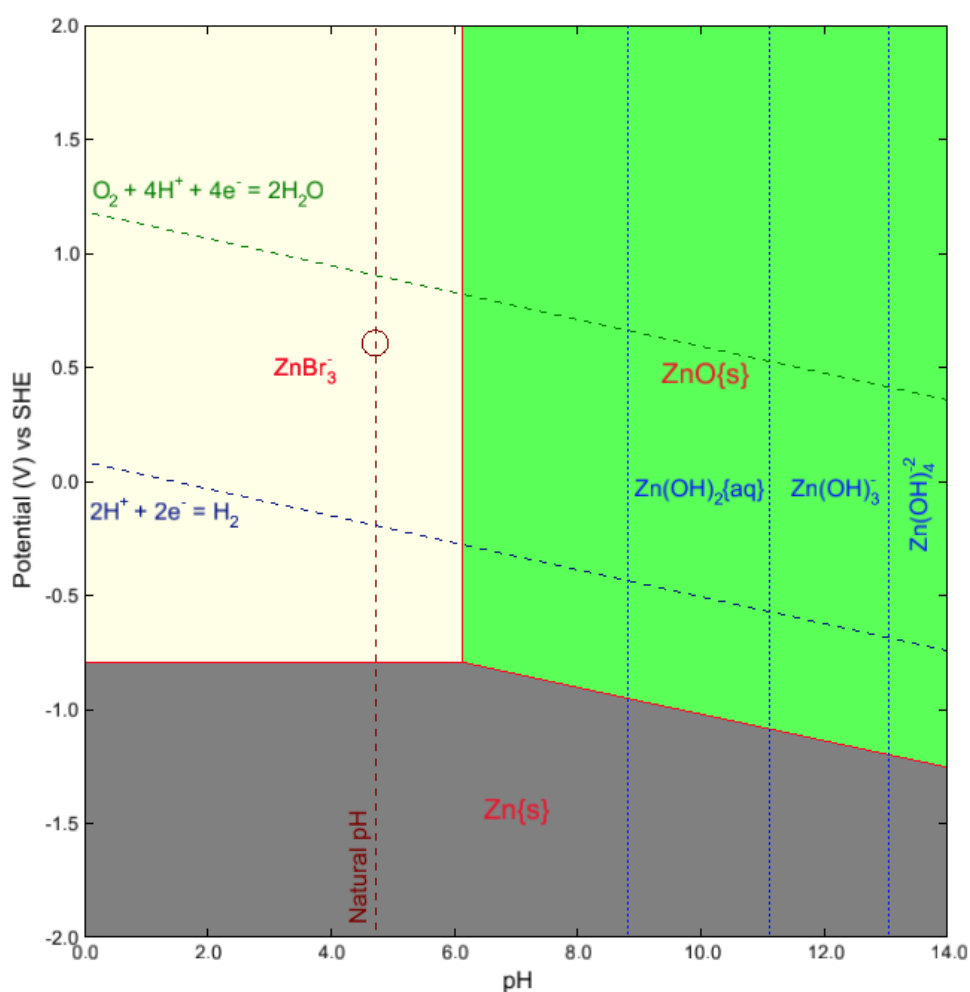
Figure 2-2. Pourbaix diagram (potential vs pH) of a 2.5 M ZnBr$_2$ electrolyte solution, indicating stability regions of various Zn-based predominant species.[1]

---

[1] The various speciation stabilities of Zn were calculated using the Margules ion exchange model at standard conditions of 25°C and 1 atm across a pH range of 0–14 (adjusted using HBr and KOH) between potentials of –2 V and 2 V versus standard hydrogen electrode (SHE). The "AQ (H$^+$ ion)" thermodynamic framework present within OLI Studio was utilized and redox chemistry calculations

The evolution of bromine from bromide anions during charging is an important process in ZBB operation. Due to the toxic and corrosive nature of bromine, a complexing agent is added to the electrolyte to sequester bromine into an alternate phase with low vapor pressure. This sequestration prevents bromine escaping from solution as a vapor and interacting with the system's environment in its elemental form. The bromine that evolves is typically complexed with a quaternary bromide salt (QBr) such as N-methyl N-ethyl pyrrolidinium bromide (MEP) or N-methyl N-ethyl morpholinium bromide (MEM) [80], which are illustrated in Figure 2-3 (on the left and right, respectively).

N-methyl N-ethyl pyrrolidinium bromide (MEP)   **N-methyl N-ethyl morpholinium bromide (MEM)**
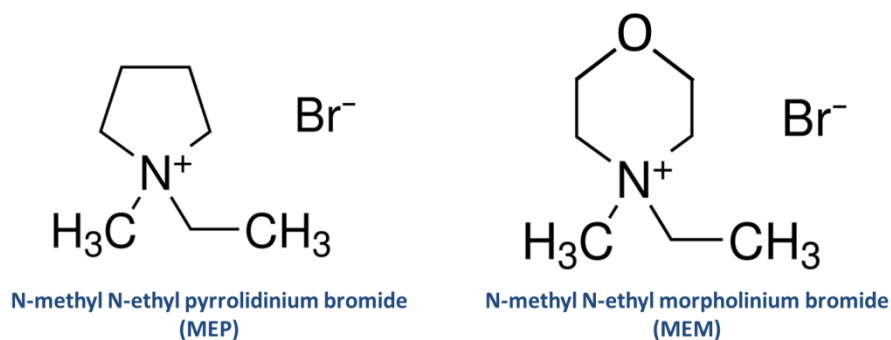
Figure 2-3. Structures of the N-methyl N-ethyl pyrrolidinium bromide (MEP, left) and N-methyl N-ethyl morpholinium bromide (MEM, right) ionic liquids conventionally used to sequester bromine during the Zn/Br RFB charging process.

The sequestered elemental bromine is stored safely in an oily phase that remains separate from the main aqueous electrolyte due to the higher specific gravity of the sequestered phase. The concentration ratio of QBr to $ZnBr_2$ generally employed is approximately 1:3,[45,81] hence a 3 M $ZnBr_2$ electrolyte solution could typically contain 1 M of bromine sequestering agent (BSA). Effective sequestration can result in bromine concentrations in the main electrolyte falling to values as low as 0.1 M.[41]

---

were included for all subsystems present. The stability regions for different Zn-based species and their phases are indicated on the diagram, with solid lines representing solid phases and dotted lines indicating aqueous phases. The natural pH of the electrolyte is also indicated on the figure, as well as aqueous lines indicating the evolution of hydrogen and reduction of oxygen (together with the relevant equations).

Other solvents such as propionitrile[82–84] have also been tested but have exhibited lower conductivity and higher toxicity and flammability,[57] giving rise to the popularity of QBr compounds as the preferred alternative for bromine sequestration in Zn/Br systems. However, concerns regarding the compatibility of MEM and MEP with various bromide reactions have prompted recent work to find suitable alternatives.[85]

Figure 2-4 shows a possible 3D molecular arrangement of gas-phase MEPBr and two sequestered Br_2 molecules. The structure is optimized by carrying out first-principles periodic density functional calculations using projector-augmented wave (PAW) potentials[86,87] for describing electron–ion interactions, within the Vienna Ab-initio Simulation Package (VASP) software.[88]
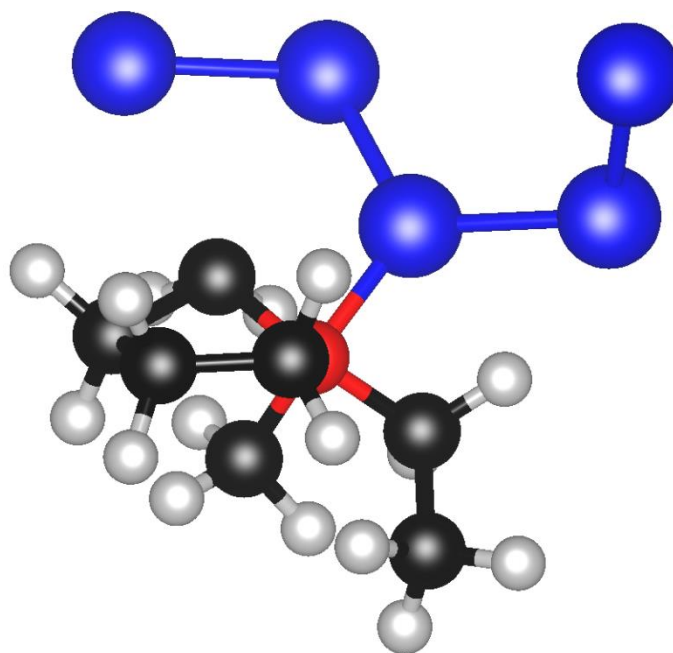
Figure 2-4. Possible structure (optimized *via* periodic density functional calculations) of MEPBr and two sequestered Br_2 molecules, with the color convention for atoms: black for carbon, grey for hydrogen, red for nitrogen and blue for bromine.

Figure 2-5 shows a possible 3D molecular arrangement of gas-phase MEMBr and two sequestered Br_2 molecules, using density functional calculations similar to those used for MEPBr with two Br_2 in Figure 2-4. These structures provide visual clarity of the

relative sizes and 3D configurations for BSAs, aiding understanding of the sequestered structure subsequently presented and discussed in section 2.4.
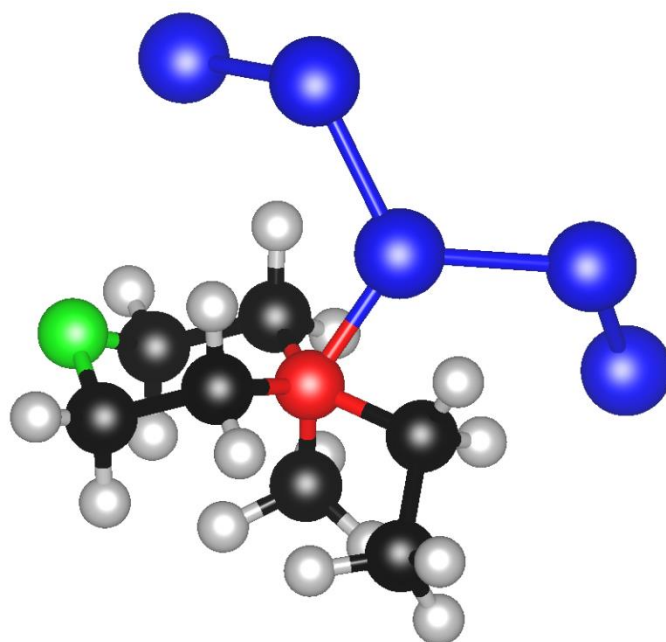
Figure 2-5. Possible structure (optimized *via* periodic density functional calculations) of MEMBr and two sequestered Br_2 molecules, with the color convention for atoms: black for carbon, grey for hydrogen, red for nitrogen, blue for bromine and green for oxygen.

It is vital that a well-controlled narrow pH range between 1 and 3.5 is maintained during ZBB operation. While the Pourbaix diagram suggests the region of Zn^{2+} species stability is below pH 6, it does not consider the presence of bromine sequestering agents (typically ionic liquids), the addition of which would influence solution behavior and pH range for practical battery operation. Zinc deposits with a moss-like appearance[41,89] can be observed with weakly acidic and basic electrolytes, whereas more acidic environments cause significant gaseous hydrogen evolution[41] that would in turn expedite zinc corrosion. Consequently, significant drops in coulombic efficiency can be expected on deviation from this working pH range due to charge being lost when protons are converted to H_2 gas instead of through the primary charge carriers of the battery. Hydrogen evolution is common in conventional Zn/Br batteries

and is known to occur concurrently (to a smaller extent) with zinc electrodeposition. The hydrogen formation is usually suppressed in conventional Zn/Br batteries due to the use of different electrode substrates (e.g. graphite) and the presence of organic additives such as the ionic liquids used for bromine sequestration. Hence hydrogen evolution is not expected to significantly complicate zinc half-cell operation unless accelerated due to the presence of other species, as will be subsequently investigated and discussed in chapter 4 of the thesis.

Conventional Zn/Br round-trip cell energy efficiency is based on both the coulombic and voltaic efficiencies, with coulombic efficiency generally influenced by the electrolyte formulation and voltaic efficiency by the membrane and electrodes used. Improving conductivity improves coulombic efficiency and the overall energy efficiency. Competing or parasitic chemical or electrochemical reactions can have significant impact on coulombic efficiency, and improvements to both voltaic and coulombic efficiencies are required for overall improvement in cell performance. It is common practice to introduce other electrochemically active species to boost operating efficiency and ionic activity by increasing the electrolyte's conductivity. An important implication to consider when introducing any type of additive is the corresponding increase in the weight of electrolyte present in the ZBB unit. Unless the compound is highly effective in increasing the electrochemical efficiency of important processes, it could negatively influence the specific energy of the system and raise production costs.

Common supporting additives include potassium chloride and ammonium-based chlorides and bromides.[50,57] These secondary electrolytes are usually added in smaller quantities than the main electrolyte and should be neutral salts in order to avoid undesirable changes to the acidic electrolyte's working pH range.[45] The type of

additive used can influence the behavior of the system. For instance, zinc electrowinning from zinc chloride baths has been found to produce rough and porous deposits.[90]

A Pourbaix diagram for a 2.5 M $ZnBr_2$ primary electrolyte solution containing 0.9 M $ZnCl_2$ as a supporting electrolyte was constructed and is presented in Figure 2-6 using a methodology similar to the calculation for pure $ZnBr_2$ presented in Figure 2-2. Interestingly, there appears to be no significant change in the dominant Zn-based species, with only slight shifts in the natural pH (becoming slightly more acidic) and the vertical pH lines (slightly more basic) separating different ionic species. Bromine and chlorine redoxes are discussed in detail in subsequent sections and chapters of this thesis when investigating suitable supporting electrolyte alternatives.
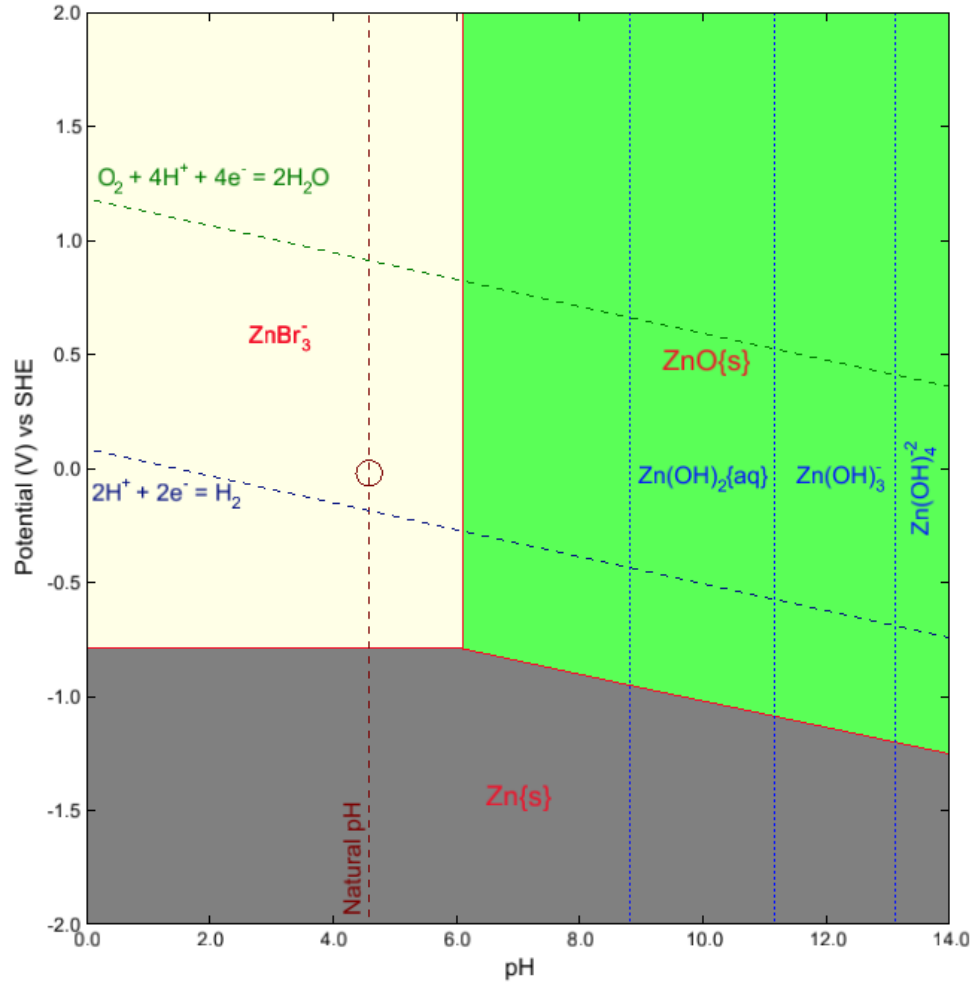
Figure 2-6. Pourbaix diagram (potential vs pH) of a solution containing 2.5 M $ZnBr_2$ (primary electrolyte) and 0.9 M $ZnCl_2$ (secondary electrolyte), indicating stability regions of various Zn-based predominant species.

2.4. Zn/Br electrode reactions

Electrodes used in ZBB cell stacks are bipolar, where a single electrode has a "positive" and "negative" side. Materials of construction for these electrodes include metals and carbon-plastic composites.

2.4.1. The zinc-side electrode

In essence, the zinc half-cell of the ZBB behaves very similarly to an electroplating system. During the charging process, cationic zinc comes out of the aqueous solution

to be electroplated onto the negative side of the bipolar electrode in the cell stack,[57] as shown by Eq. 2-1:

$$Zn^{2+} + 2e^- \rightarrow Zn, E^0 = -0.76\,V\,vs\,SHE \qquad \text{[Eq. 2-1]}$$

The reverse occurs during discharge of the battery as the electroplated zinc loses two electrons to the bipolar electrode and dissolves back into aqueous solution.

2.4.2. The bromine-side electrode

During charging, bromide anions are converted to bromine which is subsequently complexed with a QBr and stored safely as a separate liquid phase,[45] as shown by Eqs. 2-2 and 2-3:

$$2Br^- \rightarrow Br_2 + 2e^- \qquad \text{[Eq. 2-2]}$$

$$Br_2 + QBr \rightarrow Br_2 - QBr\,complex \qquad \text{[Eq. 2-3]}$$

The QBr–polybromide complex is removed from the vicinity of the electrode surface by constant circulation of the electrolyte within the battery (via pumps) during the charging process. Similarly, electrolyte circulation is used to transport the complex from storage within the tanks/reservoirs to the electrode surface for charge transfer to occur. The formation of polybromide changes the kinetics and potential of the bromine/bromide redox, while the bromine sequestration would cause reactions in that half-cell to become sluggish due to the addition of an additional sequestration/dissociation step during charge/discharge.

Additionally, monobromide ions have been found to react with aqueous bromine being evolved during charging to form tribromide ions and higher polybromides,[91,92] as shown by Eqs. 2-4 to 2-6:

$$Br^- + Br_2 \rightarrow Br_3^- \qquad \text{[Eq. 2-4]}$$

$$Br_3^- + Br_2 \rightarrow Br_5^-$$
<div align="right">[Eq. 2-5]</div>

$$Br_5^- + Br_2 \rightarrow Br_7^-, etc.$$
<div align="right">[Eq. 2-6]</div>

During discharge, bromine dissociates from the QBr complex and is reduced to the anionic bromide form, as shown by Eqs. 2-7 to 2-8:

$$Br_2 - QBr \; complex \rightarrow Br_2 + QBr$$
<div align="right">[Eq. 2-7]</div>

$$Br_2 + 2e^- \rightarrow 2Br^-, E^0 = +1.065 \, V \, vs \, SHE$$
<div align="right">[Eq. 2-8]</div>
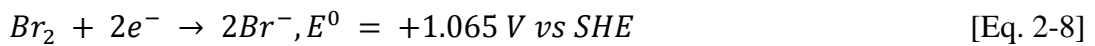
2.4.3. Overall battery reaction

When the ZBB is charged, the overall chemical reaction involves the reduction of zinc and evolution of bromine, as shown by Eq. 2-9:

$$ZnBr_2 \rightarrow Zn + Br_2$$
<div align="right">[Eq. 2-9]</div>

Similarly, zinc and bromine recombine to form ZnBr$_2$ when the ZBB is discharged, as shown by Eq. 2-10:

$$Zn + Br_2 \rightarrow ZnBr_2, E^\circ = +1.828 \, V \, vs \, SHE$$
<div align="right">[Eq. 2-10]</div>

Based on the individual half-cell reaction potentials, the theoretical electrochemical potential offered by a single Zn/Br cell should be approximately 1.828 V. This value is the Nernstian potential under zero current flow. However, the presence of internal inefficiencies and various resistance contributions seen in practice are expected to result in slightly lower cell voltage values. Another important performance metric for Zn/Br systems is current density, which is the amount of current passing through a unit area of an electrode surface. The current density, in turn, has a direct influence on the electrode capacity (i.e. energy per unit area) as well as the operating efficiency of the overall system.

While it is agreed that the bromide-side redox is generally considered limiting for the overall full-cell, the zinc half-cell is generally neglected during research and development efforts of the Zn/Br system although that half-cell also influences overall cell performance. This explains the rationale for pursuing investigations within the zinc half-cell in the present work as part of a larger fundamental investigation into the Zn/Br system.

An example of how battery voltage and current within a bench-scale Zn/Br system change during full-cell charge/discharge cycling is presented in Figure 2-7. This curve was obtained from 2 hours of charging followed by 2 hours of discharge phase under a current density of 20 mA cm^{-2} using graphite-coated carbon nanotube-embedded high-density polyethylene electrodes and a battery solution comprising 2.5 M ZnBr$_2$ primary electrolyte and 1 M MEP.
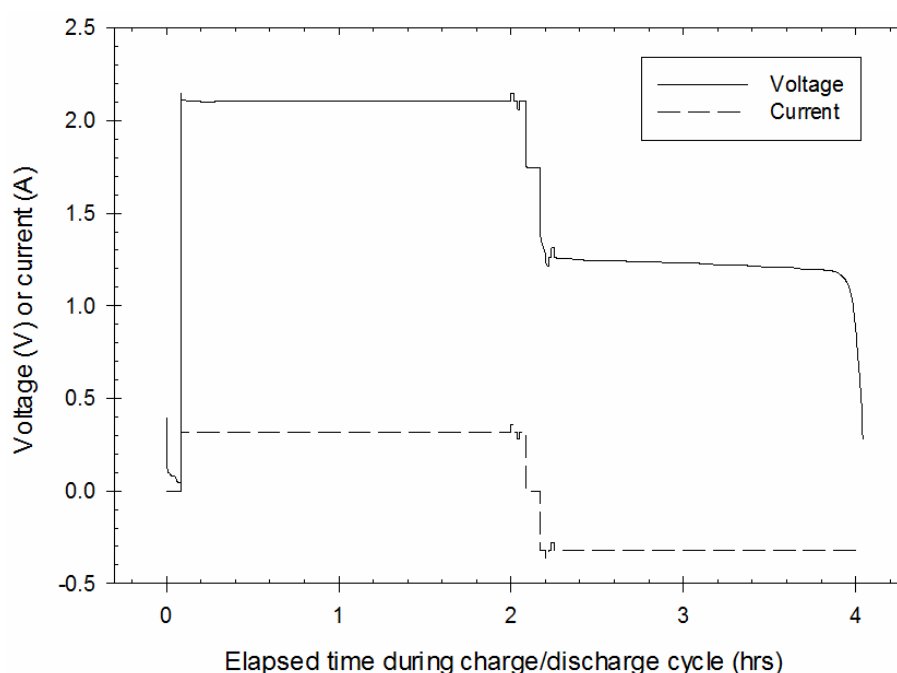
Figure 2-7. Profiles of transient battery voltage and current during full-cell charge/discharge cycling of a bench-scale Zn/Br system.[2]

---

[2] Experimental data kindly provided by Martin Schneider of the Energy Storage Group at the University of Sydney.

An example of how the energy balance and total capacity of the Zn/Br battery in Figure 2-7 change during charge/discharge cycling is presented in Figure 2-8. These figures illustrate the relationship between energy balance and total capacity, as well as the practical drop between charging and discharging voltage and current.
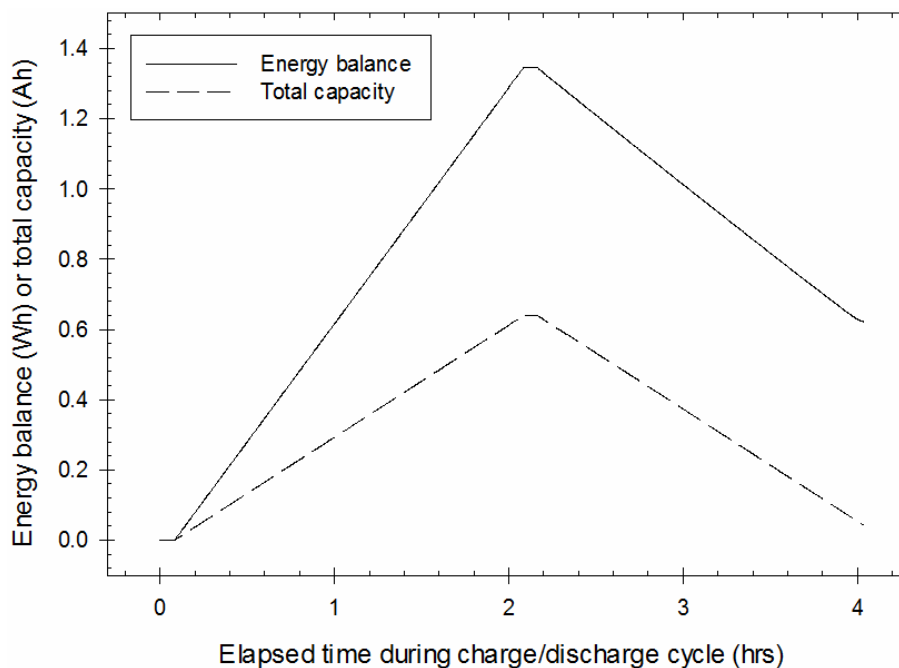
Figure 2-8. Profiles of transient energy balance and total capacity during full-cell charge/discharge cycling of a bench-scale Zn/Br system.[3]

2.5. Fundamental studies of full- and half-cell Zn/Br systems

2.5.1. Revisiting zinc-side electrochemistry and zinc electrodeposition morphology

On the basis of a reasonable understanding of Zn/Br redox flow battery systems obtained from this chapter, it is possible to formulate a sound strategy to carry out in-depth studies of each Zn/Br half-cell (i.e. the zinc and bromine sides). The knowledge obtained from such investigations would in turn enable the testing and identification

---

[3] Experimental data kindly provided by Martin Schneider of the Energy Storage Group at the University of Sydney.

22

of methods to individually optimize each half-cell to achieve significantly better overall performance. A deeper understanding of zinc-side electrochemical processes occurring in the Zn/Br during charge/discharge cycling, based on collating and reviewing relevant literature pertaining to this area from the field of flow batteries and others (industrial electroplating, etc.) is required. Understanding the problems faced by earlier generations of Zn/Br systems due to the utilization of metallic electrodes increases the attractiveness and viability of employing carbon-based electrode stacks instead, primarily due to cost considerations. It is also necessary to a detailed look at zinc-side redox mechanisms and the kinetics of related reactions, leading into methods of catalytically enhancing electrode performance. These aspects are separately detailed in recent work reviewing this area.[93]

The electrochemical performance of the zinc half-cell is strongly linked to the quality and morphology of zinc electrodeposits generated during the charging phase. The structure of the zinc plating also dictates performance characteristics such as efficiencies, charge densities and peak current values during the subsequent discharge phase. In addition to deeply analyzing the considerations arising from chemical reactions occurring at the zinc-side electrode, it is also necessary to understand the underlying reasons regarding why different zinc plating morphologies are obtained under different conditions and how certain behavior such as dendritic growth can be detrimental to Zn/Br performance. Such considerations are reviewed in depth by recent work in the area.[94] Promising methods for solving such issues can be identified from a wide range of literature including studies directly related to redox flow batteries as well as from the highly established electroplating industry. In particular, the primary means of controlling zinc crystal structure involves the use of organic additives to achieve a specific growth template and rate. Weighing the merits and drawbacks of

alternative strategies such as controlling deposition rates is an important step during such developments.

2.5.2. Bromine-side electrode functionality

As with establishing a sound understanding of zinc-related physical and electrochemical processes in order to achieve optimal performance in the zinc half-cell, a similar approach can be taken for in-depth study of the bromine half-cell. The aim of such an endeavor includes the development of novel strategies and/or adapting existing methods of optimizing the Br^-/Br_2 redox to suit the Zn/Br electrochemical environment, thereby significantly improving Zn/Br system performance. Such an endeavor begins with a detailed review[95] of literature pertaining to relevant studies of reactions at the bromine-side electrode (both for within the Zn/Br system as well as different but related environments) to establish strong understanding of the fundamental physical and electrochemical processes that occur during charge and discharge phases of the battery. Understanding the materials challenges for conventional Zn/Br systems would allow for the assessment of viability of opportunities to improve electrode functionality through methods such as strategic catalyst doping leading to enhanced electrochemical performance.

2.6. Bromine storage, treatment and toxicity

Depending on the state-of-charge (SoC) during the charge/discharge cycle of the ZBB, bromine exists in various forms within the electrolyte solution: as elemental bromine upon charging (i.e. Br_2), monobromide, tribromide, pentabromide or higher. Of these, aqueous elemental bromine is volatile and risks escaping into the external environment as a gas in the event of containment breaching. This is avoided by sequestering the Br_2 into a complex liquid phase using a suitable QBr, thereby lowering its vapor pressure

and likelihood of escape. Information about bromine toxicity is readily available in material safety data sheets.[96] Contact with gaseous elemental bromine is hazardous to health as it is damaging to the eyes and skin. It is detectable by its strong suffocating odor and can be fatal if inhaled as it damages the respiratory system. Bromine is also harmful to the environment, especially to aquatic life. Consequently, the safe operation of Zn/Br RFBs is an important factor influencing the uptake of the technology for utility-scale electrical energy storage.

2.7. The membrane separator

The membrane separator is an integral component in the Zn/Br RFB as it serves as a barrier that prevents cross-contamination of electrochemically active species in the system, as well as reducing possible electrical contact across electrodes. An electrochemical requirement of the system is to minimize the diffusion of Br_2 to electroplated Zn as much as reasonably possible, to prevent self-discharge of the ZBB when it is charged but left unused for an extended period of time. The occurrence of self-discharge would in turn lead to lower coulombic efficiency of the system. This self-discharge mechanism is attributed to the action of aqueous bromine evolved on the bromine side migrating to the zinc-side electrode through the membrane separator because it is a neutral species and subsequently oxidizing the electroplated zinc, thus causing the battery to discharge itself.[97] Thermodynamically, bromine is an effective corrosion agent of zinc, indicating the severity of problems faced by the ZBB if the issue is left unchecked.[98] This is avoided by the use of independent circulatory loops for the aqueous zinc bromide electrolyte on both sides of the bipolar electrode stack, together with a microporous film or ion exchange membrane serving as a separator.[99]

Two possibilities have been proposed to explain the principles governing bromine diffusion though membranes: it is possible that (a) the action of bromine complexes

wetting the separator provides a pathway for elemental bromine to diffuse through or (b) there exists an equilibrium between the bromine in the aqueous phase diffusing through the separator and that in the bulk electrolyte.[89] Studies comparing various ion-exchange membranes have shown that diffusion coefficients of bromine have a wide range of values between 1.44×10^{-10}–3.74×10^{-10} cm^2 s^{-1} [89] and 1.52×10^{-8}–2.28×10^{-8} cm^2 s^{-1}.[100] While ion-exchange membranes are highly selective for certain ions, the mass transport rate of neutral species across them is largely dependent on the frictional or hydrodynamic resistance,[101] resulting in a significantly small (and yet existing) flux. In one set of studies,[89] it was also found that the rate of bromine diffusion through the separator in the presence of aqueous and complex phases could be twice as high as that in the presence of an aqueous phase alone. Diffusion through a membrane can be linked to the degree of wetting, and depending on the chemical structure of the membrane used, that wetting could be higher in the presence of a complex phase compared to a purely aqueous phase.

Due to the nature of bromine diffusion described above, requirements for membrane separators are stringent because a high degree of selectivity is necessary to differentiate between bromide ions and ionic zinc which should be allowed to pass through. This differentiation refers to the importance of ensuring ions useful to each half-cell remain in their respective half-cells. The membrane separator also serves as a barrier against the migration of bromine into the zinc-side region, whether in the elemental form or complexed with QBr. As an extension to different interactions with various species, membranes need to be as chemically inert as possible and not participate in undesirable side-reactions such as promoting degradation of the electrolyte. It is also imperative that membranes used can withstand the harsh operating environment of ZBBs for reasonably extended periods of time. Durability is thus an important factor when

selecting the appropriate membrane for use in the system. Various materials with specific properties have been tested for use in ZBBs, including microporous plastic separators such as polyolefin Daramic®.[102,103] Comparisons between uncoated and fluorine-treated Asahi SF-600 membranes have shown that the latter displayed improved selectivity against bromine diffusion.[89] For the case of plastic-silica composite separators, it has been found that higher silica loading levels result in lower membrane resistivity and higher bromine flux, consequently contributing towards improved coulombic and energy efficiencies.[104]

Stable but more expensive cation-exchange systems such as Nafion® have also been tested[105] and found to be more effective at reducing bromine transport through the separator than their microporous counterparts, because bromide species are mostly present as anionic Br_3^- and Br_5^- complexes.[45] The success of such ion-exchange membranes has prompted a recent review[106] and spurred further work to incorporate multiple such membranes into a single working unit for use in RFBs.[107] Another class of functionalized separators includes sulfonated polysulfone membranes which have been demonstrated as performing better than those constructed *via* grafting of organic substrates.[108] The sulfonated polysulfone membranes performed better due to chemical resistivity against the electrolyte used in the zinc-based redox battery studied, whereas up to 30% weight loss was observed for grafted membranes, thereby leading to reduced performance compared to the former type.

Membranes constructed from zeolites have also been tested in a vanadium-based system and found to provide a high degree of selectivity based on ion size,[109] leading to the transport of desirable species while restricting others. Based on the discussion of results from testing the zeolites in that study, the excellent adsorption characteristics of zeolites are a likely basis for the high degree of selectivity to the point of stopping

27

almost all ion transport except for those of a particular size. Interestingly, tests carried out in all-V RFBs involving surfactant-functionalized ion-exchange membranes indicate that the amount of water passing through the membrane can be controlled, while also improving overall system performance.[110]

Studies of V/Br systems have also found that the ratio of different bromine sequestering agents (MEP and MEM) used in solution have direct influence on voltaic efficiencies due to variation in membrane-related resistances.[111] With motivation from these findings, pursuing similar functionalization work for Zn/Br RFB membranes as well achieving a suitable balance using mixed BSAs could prove beneficial in the short- to intermediate-term with regard to improved energy efficiencies.

It is recognized that optimization of separators and study of electrochemical phenomena at the ZBB membrane is an important part of the development process, such as novel graphene oxide–Nafion composite materials.[112] However, this aspect is left for another review and future work focusing on membrane technology for RFB applications.

2.8. Accurate determination of SoC

Determining the SoC accurately and reliably should be considered an integral aspect of ZBB research as it provides a useful pathway towards tracking the degree of impact on battery performance of changes to electrolytes and electrodes. Surprisingly, although SoC is also a clear indicator of whether the full extent of the system's energy storage capacity is being utilized,[113] this is a relatively rarely discussed issue in the literature surveyed. Accurate monitoring of SoC is of high importance and significance as SoC is a direct result of the primary and secondary electrochemical and physical processes occurring within the ZBB as the cyclic charge/discharge operation

progresses. With accurate monitoring, therefore, it would be possible to conclusively determine which electrochemically active species cause, dominate and contribute to these processes at any given point in time, thereby indicating which processes might create operational bottlenecks.

A significant proportion of literature pertaining to SoC measurement strategies was published within the past decade, motivated primarily by work carried out on batteries for electric vehicles. Although the open-circuit voltage (OCV) method has been used for ZBBs,[114] there are no standard methods in particular. It is increasingly clear, however, that some of the underlying principles and logic might be adapted for use in Zn/Br RFBs regardless of whether the original work was intended for nickel/metal hydride (NiMH), nickel/cadmium (Ni–Cd) or Li-ion systems. Several methods have been developed to measure the SoC of energy storage systems, particularly batteries, including ampere–hour counting, Kalman filters, internal resistance measurement and heuristic techniques based on charge/discharge characteristics.[114] Most direct methods such as OCV and coulometry are too simplistic to robustly handle complex and dynamic systems such as lead/acid batteries.[115] By extension, it can be expected that these methods would pose similar problems in ZBBs due to their relatively complex system configurations.

Relatively recent work on improving the Coulomb counting approach has demonstrated its effectiveness at determining SoC, making it the most convenient method at present.[116] Yet this approach of current integration possesses inherent drawbacks as it does not account for the effects of operating temperature fluctuations or deviations due to operating inefficiencies, hence discharge tests are the only completely reliable means of confirming whether the SoC measurement is correct.[117] This drawback has prompted work to improve the method by applying regular and

extended Kalman filters (algorithms used to make reasonable estimates from noisy data) which make corrections for drifts in system behavior[118] and have been proved to be accurate within 2–3%[119,120] when estimating SoC in lead/acid batteries. Extended Kalman filters have also been shown to provide good SoC estimations in Li-ion batteries when applied to data obtained *via* transient cell voltage[121,122] and OCV[123] measurements. Other direct methods, such as measuring individual half-cell conductivity and tracking changes in electrolyte color during charging or discharging of vanadium RFBs, have also been proved to be simple yet effective strategies.[124]

The sensitivity and non-destructive nature of electrochemical impedance spectroscopy (EIS) makes it an attractive method for use in SoC measurement of secondary batteries,[125,126] with the possibility of on-line measurement[114] to avoid disrupting battery operation each time a measurement is required. For instance, changes in temperature influences viscosity and mobility of ions in solution, which can be picked up by EIS measuremnets. The benefits of EIS have prompted some successful work involving the modelling of voltage behavior in NiMH batteries based on the concept of impedance.[127] There has also been work to improve fractional system identification in conjunction with Randles' model of lead/acid battery impedance behavior,[128] as well as study of the impact of changes in SoC on the linearity of applied current (stepwise variation of the cell voltage) in Li-ion batteries.[129] Voltage drops occurring at the beginning of discharge cycles in lead/acid batteries have been found to influence the methods and results of SoC calculations[130] and are quite possibly an important phenomenon to keep in view for ZBBs. By extension, it is also necessary to account for other phenomena exhibiting similar behavior (i.e. spikes or drops) upon commencement of charging or discharge of the system, in order to obtain an accurate SoC value.

Adaptive algorithms incorporating hysteresis phenomena have proved effective at estimating SoC in NiMH batteries when calculated using directly obtainable data such as OCV.[131] It is to be noted that measuring the OCV as a means of determining state of charge can be influenced by the battery chemistry and materials under consideration, particularly those which undergo two-phase versus one-phase (solid solution) discharge and charge processes. Comprehensive models have been proposed that account for cycle ageing and temperature effects in Li-ion systems, thereby addressing these requirements for dynamic monitoring of battery performance.[132] It follows that combining these various algorithms could potentially produce highly robust SoC predictions.

The use of artificial neural networks has been shown to be quite effective and computationally efficient in on-line SoC determination for lead/acid,[133] NiMH[134] and Li-ion[135] batteries. Independent studies have applied fuzzy logic mathematics to successfully predict SoC in Li-ion batteries[136] as have various systems based on data obtained from Coulomb counting and/or EIS.[137] Self-learning mechanisms incorporating fuzzy neural networks as well as cerebellar-model-articulation and learning controllers are particularly adept at estimating the SoC of systems with nonlinear discharge characteristics.[138] An adaptive neuro–fuzzy inference combination has also been shown to produce fairly reliable SoC estimates.[139] From the numerous publications proposing algorithms for computational efficiency, it has been shown that a combination of even a few of these functions is capable of producing superior SoC estimation methods[140] compared to present simpler approaches. Besides these complex approaches, some effective strategies have been proposed relatively recently to minimize errors produced by simple methods using a sliding mode observer in batteries for hybrid electric vehicles.[141]

The high sensitivity of EIS to sources of resistance linked to the states of charge and health of a battery makes EIS an extremely useful tool for measuring these properties[126] and it is likely to be suitable for adaptation into ZBB systems. Regardless of the specific method employed, whether under constant current (galvanostatic) or constant potential (potentiostatic at open-circuit or non-zero potential with respect to a reference electrode), the basis of EIS as a tool for tracking SoC relies on interpreting changes in impedance spectra. Based on currently available literature, the use of EIS in monitoring SoC is primarily limited to Li-ion cells, with some studies also covering lead/acid batteries and nickel-based systems.[125,126] Characteristic inductive loops at particular frequencies and marked changes have been observed in the low frequency range ($\leq$1 Hz) during EIS of lead/acid cells.[125,142,143] The longer a battery's charge duration, the higher the degree of depletion of ions involved in redox processes at the respective electrodes, which would in turn lead to impedance contributions attributed to Warburg diffusion limitations observed at lower frequencies. Warburg impedance measurements can be significantly affected by flowing or stirred electrolytes at different flowrates due to possible differences in homogeneity of the solution and thicknesses of diffusion layers close to the electrode surface. By extension, it is possible that some of these principles could be applied when studying the aqueous-based Zn/Br RFB.

Characteristic resonance frequencies have been noted for Ni/Cd and NiMH cells where the impedance shifts from inductive to capacitive behavior as a function of SoC.[144] This is an interesting and potentially useful phenomenon that could be utilized when adapting EIS for use in ZBB systems. However, the fact remains that EIS by itself contains too many variables and many possibly valid interpretations of impedance spectra. Further studies involving lead/acid batteries have confirmed the usefulness of

EIS in determining SoC and state-of-health, but with the important caveat that the information obtained can only be considered reliable if combined with self-learning tools and/or additional algorithms.[145] Combining the sensitivity of EIS with fuzzy logic has been shown to further improve accuracy in determining SoC.[146]

2.9. Maximizing practical specific energy of the system

Although there are many conventional and innovative methods of determining SoC, a concurrent main objective should be to achieve maximum utility of the electrolyte's energy capacity. Surprisingly, this important issue is not discussed in the literature despite having direct bearing on the time it takes to charge a Zn/Br RFB and on the practical specific energy of the system. Therefore the issue is briefly highlighted here. Under ideal conditions, the entire stock of primary ions in the primary $ZnBr_2$ electrolyte should be involved in charge-transfer reactions at the electrodes in order to obtain full utility from a given amount of electrolyte solution. Unfortunately, due to the aqueous nature of the electrolyte solution, practical limitations on the charging and discharging durations of the battery exist in normal operation.

Since the Zn/Br RFB relies on the transport of ions to and from the electrode surfaces, some Zn^{2+} and Br^- ions would still remain in solution after charging has progressed for an extended period of time, with their concentrations reduced to low levels. This situation makes it impractical to continue charging, due to low diffusion rates that would produce only small increments in SoC, meaning that full depletion of the electrolyte is inefficient. Consequently, even if 70% maximum SoC is reached, 30% of the capacity is still not utilized despite being physically available. Thus there is an imperative for future designs to seek out methods to increase the practically attainable maximum SoC.

2.10. Moving from bench scale to large/utility scale

Migration from developing and testing the new generation of ZBBs from bench to utility-scale operation poses a number of challenges that must be addressed for the technology to be commercially competitive. Factors that will be of prime concern include the purity of electrolyte obtained (whether it be on the large scale or laboratory scale), as contaminants at even parts-per-million concentrations might result in hydrogen generation, accelerated degradation of electrode performance or poisoning of the electrolyte solution. Similarly, the quality of electrodes used would influence the rate at which the cell stack requires replacement, thereby directly affecting the maintenance and operating costs of the utility-scale system.

Cell architecture is an important factor influencing flow battery performance. Challenges include design considerations to minimize pumping losses during construction of large-scale systems. An issue unique to flow batteries is the presence of shunt currents. These currents arise through electrical pathways formed through the flow channels feeding each cell. The individual cells are electrically connected in series; however, the electrolyte flows through a manifold in parallel, thereby allowing current to flow between cells through the electrolyte. In practice, this effect is minimized through the use of narrow channels for electrolyte delivery.

Emerging technologies such as 3D-printing are already being investigated[147] and seem to hold much promise for constructing the next-generation of RFB systems, and flexible Zn/Br RFBs have also recently been developed and tested.[148] 3D printing has significant potential including mass-fabrication of system components, promoting advances in cell architecture which were previously complicated due to reasons such as the need for multiple interconnected parts. Furthermore, the final operating environment needs to be given due consideration, with such considerations as suitable

heating/cooling strategies to control battery temperatures and achieve optimal operating efficiencies. It is clear that optimizing the system at bench-scale using intelligent materials and predictive control is an appropriate strategy to reduce sources of inefficiencies prior to scale-up. Other challenges, such as power conversion and matching to fluctuations in charging sources and applied loads, will also need to be addressed.

3. The Influence of a Chloride-Based Supporting Electrolyte on Zn(001) Surfaces

3.1. Chapter abstract

A combination of analytical techniques and molecular modelling methods was used to study the influence of chloride-based supporting electrolytes on zinc electrodeposit surfaces in the zinc half-cell of zinc/bromine flow batteries. Scanning electron microscopy and X-ray diffraction analysis of zinc electrodeposits obtained during charging show that increasing $ZnCl_2$ concentration influences crystallinity and changes the preferred orientation from (004) at 0.5M to (101) at 2M. Analysis using periodic density functional methods indicates that the binding energy of Cl to the Zn(001) surface depends more strongly on surface coverage than on binding site location. Solvation increases the stability of Cl binding to the surface. The binding energies of Cl with and without water solvation are between 288–327 kJ mol^{-1} and 249–288 kJ mol^{-1}, respectively, for coverages between 0.11–0.33 ML. The binding of Cl leads to Zn surface buckling and decreases surface uniformity. Binding at 0.33 ML and above results in surface instabilities, leading to the formation of surface cavities due to significant vertical displacement of surface Zn sites.

3.2. Chapter introduction

The work presented in this chapter builds upon the understanding of the Zn/Br system presented in Chapter 2 and focusses on understanding the interactions between solutes with electrodeposited zinc in the zinc half-cell in a Zn/Br RFB. The degree of zinc deposit compactness has direct influence on battery performance[149] and current efficiencies are linked to the morphology of electrodeposits.[90] Compactness of zinc deposits is related to improvements in plating density and higher surface coverage

which results in lesser zinc remaining on the electrode after practical discharge is complete. Even during the later stages of discharge there will be a higher local current density required if an overall galvanostatic discharge is to be maintained. Uniform zinc plating is necessary to achieve good current densities as it effectively utilizes the available electrode surface area. Conversely, poor deposition with dendritic features or kink sites reduces current densities even for high-conductivity electrodes. Dendrites also risk puncturing the separating membrane in full-cell systems. In order to make beneficial changes to the Zn/Br system, it is first necessary to understand the fundamental reactions occurring between species already existing in conventional electrolyte solutions. Specifically, it is important to identify which components might potentially be influencing zinc deposition negatively and use this information to seek suitable alternatives in order to improve battery performance.

Chloride-based additives such as potassium chloride, sodium chloride and ammonium-based chlorides[50,57,150] can be included as supporting electrolytes to maintain ionic conductivity of the solution when the primary electrolyte ions are depleted during charging. The reduction of chlorine (Eq. 3-1) occurs as follows:[151]

$$Cl_2 \text{ (aq)} + 2e^- \rightarrow 2\ Cl^- \text{ (aq)}, E° = +1.36 \text{ V vs SHE} \qquad \text{[Eq. 3-1]}$$

Chlorides are presently considered suitable for use as secondary electrolytes as chlorine has a higher reduction potential than bromine (difference of 0.29 V vs SHE) and is not expected to interfere with the bromine-side redox process during battery operation. However, there exists a possibility that the use of chlorides could have negative effects on zinc half-cell performance, given that zinc is susceptible to corrosion by chloride-containing species[152] and aqueous chlorine is effective at leaching solid zinc.[153] It has long been known that zinc chloride concentration has a major influence on the surface roughness of zinc deposits obtained from such

solutions,[154] and it has been reported that zinc electrowon from zinc chloride solutions produced rough deposits which were also porous.[90] Chlorides have been found to influence the characteristics of zinc deposits above concentrations of 500 mg L^{-1},[155] which is of relevance to the present work as conventional Zn/Br secondary electrolytes can have significantly higher chloride concentrations. There has also been recent work to replace chloride-based additives with other anions,[156] including perchlorates,[157] with positive results.

The use of ethylene diamine and ammonia additives to inhibit chloride adsorption onto the electrode surface has shown that controlling the electrical double-layer is a key factor influencing zinc deposit structure.[158] This inhibition occurs by altering the nucleation mechanism and growth rate, influencing the homogeneity of crystal size distribution. Electrochemical impedance spectroscopy (EIS) investigations of zinc deposition from chloride-based electrolytes have also indicated that chlorides could potentially be adsorbed onto the zinc surface.[159] Nucleation overpotential for the deposition of zinc from 3 M $ZnCl_2$ electrolytes is slightly higher than for $ZnBr_2$ electrolytes of similar concentration,[160] indicating that chlorides reduce the zinc deposition and stripping efficiency. Zinc bromide complexes also have lower stability constants but faster kinetics compared to those of zinc chloride. Comparison of zinc deposits from pure chloride-based electrolytes against those with citrate additive in zinc/polyaniline batteries has shown the latter to produce smoother deposits whereas the former promotes dendritic growth,[161] indicating inhibition of negative effects caused by chlorides. The reason stated in literature for obtaining the smoother deposits was that citrate decreases exchange current density and increases the Tafel slope, lowering dendrite formation and the rate at which zinc corrodes.

The experimental observations described above may be explained *via* molecular modelling of the interactions between Cl and zinc surfaces. Previous literature involving density functional theory (DFT) calculations and Zn(001) is limited to Zn adatom migration across that surface.[162] To the best of our knowledge, however, studies on interactions between Cl/Cl$_2$ and the Zn(001) surface have not been reported. Furthermore, most DFT studies related to energy storage have been carried out for lithium-based systems whereas few exist for zinc-based batteries, such as the zinc/air battery.[163] The characteristics of the interaction between Cl and Zn surfaces such as surface restructuring, binding energies and Cl surface diffusion paths have not been determined.

DFT has been used to study the interactions of Cl with different metallic surfaces as well as those exhibiting metallic behavior. Cl is reported to migrate rapidly across graphene surfaces with negligible energy barrier if it is bound to graphene with a significant binding energy, and chlorination of graphene at high coverage results in a buckled surface.[164] DFT and experimental investigations involving Au(111) found that Cl coverages above 0.33 monolayer result in surface saturation and system instabilities as Au atoms are removed from the surface to form an Au–Cl compound (a complex superlattice), ostensibly resulting in a more energetically stable configuration, and that Cl preferentially binds above fcc sites.[165,166] A similar saturation behavior is reported for Cl above Cu(111).[167] DFT investigations of halogen-metal interactions with the (111) surface of metals such as Pd, Pt, Cu and Au, found that halogen−metal binding energies varies inversely with the size of the halogen atoms.[168] Cl binds to metals altering the morphology of the surface[165,166] and creates surface vacancies at high coverage.[169]

The present work combines analytical techniques with periodic DFT approaches to study the influence of chloride-based supporting electrolyte concentration on zinc electrodeposit surfaces in the zinc half-cell of Zn/Br flow batteries. Experimental evidence is reported on the effect that chlorides have on zinc electrodeposits during and after the charging phase. This is followed by DFT analysis on the influence of surface coverage on a Zn(001) surface. Zn deposition on carbon involves nucleation followed by 3-dimensional growth, which is a process very different from that on Zn(001). However, modelling was performed on the Zn(001) surface as the objective of this study is to investigate interactions between Cl and the final zinc surface, particularly to understand any corrosive behavior, whereas the growth mechanism itself is not the focus. This investigation provides insights and builds a foundation for explaining some fundamental processes occurring within the Zn/Br system, especially at the electrode–electrolyte interface. This is an important linking step for when subsequent studies are carried out for interactions in the aqueous phase and when the influences of other ions are considered. The findings presented herein are expected to influence future Zn/Br electrolyte formulation, which is a fundamental aspect of battery design, as well as strategies developed to reduce the negative impacts chlorides may have on system operation.

3.3. Methodology

3.3.1. Preparation and characterization of zinc electrodeposits from Zn/Br cell charging

Solutions of 2.25 M $ZnBr_2$ (Merck, 98%) primary electrolytes were prepared with 3 concentrations of $ZnCl_2$ (VWR, 98%) supporting electrolyte: 0.5, 1 and 2 M. The zinc salts used were dried in a vacuum oven at 50°C for over 5 days prior to preparation of

testing solutions. 0.8 M N-methyl N-ethyl pyrrolidinium bromide was added to each solution to reflect the conventional molarity of BSAs in Zn/Br systems.[45,81] Zinc was electrodeposited from each solution onto graphite-coated carbon plastic electrode sheets (RedFlow Ltd., Brisbane, Australia) for 10 minutes at a current density of 20 mA cm^{-2} using a Neware battery cycler. Zinc electrodeposition using two- (battery) and three- (half-cell) electrode systems would differ in their influence of the field configuration between working and counter electrodes, hence the electrodeposition studied in this chapter uses the former configuration in keeping with practical battery operating conditions. Zinc electrodeposit morphology is also influenced by overpotential which in turn can vary locally due to the current density distribution. Consequently, deposition was carried out using electrodes with a relatively small 0.3 cm^2 exposed area to minimize such effects. Solutions were magnetically stirred at 300 rpm during electrodeposition to promote homogeneity while the ambient temperature was maintained at 25±1.5°C. Zinc deposits were kept in a vacuum environment prior to characterization to prevent oxidation. Scanning electron microscopy (SEM) was carried out with a JCM-6000 NeoScope Benchtop SEM operating at 15 kV. X-ray diffraction (XRD) analysis was performed with a Shimadzu S6000 using a Cu-Kα target (40 kV, 30 mA), scanning from 30–80° at 5° min^{-1} with a step size of 0.02°. The XRD data obtained was analyzed using the PDF4+ software database for peak identification. The Williamson–Hall method[170,171] was used to analyze XRD peak data and compare the relative sizes of zinc crystals obtained during electrodeposition as the presence of chlorides in the electrolyte increases. LaB$_6$ was used as a standard reference material (NIST SRM 660a) due to its well-defined peaks, and the full width at half maximum (FWHM, β) is calculated as a function of the diffraction angle θ, as follows (Eq. 3-2):

$$4\eta \times \sin\theta + \frac{k\lambda}{D} = \sqrt{\beta_{Observed}^2 - \beta_{Instrument}^2} \times \cos\theta \qquad \text{[Eq. 3-2]}$$

where η is the zinc crystal strain, θ the reflection angle (°), k a constant, λ the Cu-Kα X-ray wavelength (1.54056 Å), D the zinc crystal size (Å), $\beta_{Observed}$ the FWHM at each indexed plane of electrodeposited zinc crystal and $\beta_{Instrumental}$ the instrument contribution calculated using a function obtained via LaB$_6$ reference. The constant k is herein assigned an arbitrary value of unity for the purpose of semi-quantitative comparison in the present work. Consequently, comparisons are made with respect to the ratio of zinc crystal sizes obtained between each of the electrolytes studied.

3.3.2. Electronic calculations

The binding energy of Cl ($E_{b,v}^{Cl}$) with the surfaces exposed to a vacuum region was calculated to quantify the interactions with the Zn surface following (Eq. 3-3):

$$E_{b,v}^{Cl} = [n_{Cl} \times E_{Cl} + E_{slab} - E_{Cl-Slab}] / n_{Cl} \qquad \text{[Eq. 3-3]}$$

where n_{Cl} is the number of Cl species above the Zn surface, E_{Cl} is the energy of an isolated Cl species, E_{slab} is the energy of the bare slab, $E_{Cl-Slab}$ is the total energy of the slab with Cl bound above the surface. A positive binding energy (i.e. $E_{b,v}^{Cl} > 0$) indicates a stable bound state, with larger binding energies indicating more stable structures compared to those with lower values. The ratio of bound Cl to the number of zinc sites on the top-most layer is defined as surface coverage (θ_{Cl}) and has units of monolayer (ML).

The electronic energies were obtained using periodic density functional theory (DFT) using the Vienna Ab-initio Simulation Program, VASP,[88] in the MedeA® software environment.[172] Projector-augmented wave (PAW) potentials[86,87] were used to describe the electron-ion interactions and the Kohn-Sham equations are solved *via* the

generalized gradient-corrected Perdew-Burke-Ernzerhof method[173] using the GGA-rPBE functional.

A Zn bulk model with space group P63/mmc was used as the initial structure. The atomic positions were fully relaxed by allowing the cell volume and cell shape to change with no symmetry constraints. A plane-wave basis represented by a kinetic energy cut-off of 500 eV and a Γ-centered k-point mesh in the Brillouin zone for the self-consistent field (SCF) interaction of (18×18×9), equivalent to a mesh point spacing of (0.149, 0.149, 0.139) Å^{-1} were used. Convergence of the atomic relaxation was achieved when the forces acting on all atoms were lower than 0.02 eV Å^{-1}. The DFT-relaxed cell parameters of $a = b = 2.68$ and $c = 5.17$ Å are slightly longer than the experimental values of $a = b = 2.66$ and $c = 4.94$ Å.[162] Isolated Cl and Cl_2 were minimized in a cubic cell with length 10 Å using spin-polarized wavefunctions and a Gaussian smearing of 0.001 eV at the gamma point.

A (3×3)-Zn(001) slab model with five Zn layers repeated in all directions with a gap spacing of 15 Å was created from the DFT-relaxed bulk model. Binding of Cl was studied on one side of the slab and a dipole correction was applied to remove any spurious artificial electrostatic interactions arising from the slab periodicity. A k-mesh of (3×3×1) corresponding to an x and y spacing of 0.301 Å^{-1} and z spacing of 0.242 Å^{-1} was used for all structural optimizations using a second-order Methfessel-Paxton (MP) smearing[174] of 0.2 eV. Sensitivity analysis with planewave cutoff energies from 300–700 eV revealed that truncation at 400 eV was a suitable practical value since the absolute energy of $E_{b,v}^{Cl}$ above 400eV changed only by 14.3 meV (about 1.4 kJ mol^{-1}) even at the highest coverage studied in this work ($\theta_{Cl} = 0.33$ ML). The bottom three Zn-layers of the slab were fixed while all other atomic species were relaxed. It is observed that the first, d_{12}, and second, d_{23}, interlayer spacing of the bare slab expanded

from the DFT-bulk relaxed spacing of 2.59 Å to $d_{12} = 2.65$ Å and $d_{23} = 2.71$ Å respectively. Sensitivity analysis showed that allowing the third layer to relax changed d_{23} only by 0.01 Å, while there was no effective change (<0.01 Å) to the third, d_{34}, interlayer spacing.

The climbing image nudged elastic band (cNEB) method[175] was used to calculate minimum energy pathways of Cl diffusion and Cl–Cl surface recombination using at least five images between initial and final states. Convergence of the cNEB was achieved when the force of the band was lower than 0.05 eV Å^{-1}. In order to ascertain the nature of the transition states, the image with the highest energy obtained with the cNEB technique was further optimized to a transition state structure, which in almost all cases resulted in no further refinement to the image obtained with cNEB technique.

Continuum solvent effects increase the binding energy of halogens to metal surfaces,[176,177] reducing surface energies[178] attributed to electrostatic interactions.[179] Explicit water molecules in the vicinity of the surface reduces polarizability of chlorides,[180] which could explain the increase in Cl–metal binding energies. Since the Zn/Br RFB electrolyte environment is aqueous, and the zinc electrodeposits generated during system operation are exposed to water, the solvation effect on Cl binding energies was determined. Consequently, solvation effects were included by using the implicit solvation model developed by Henning and co-workers, and implemented in the VASPsol[178] routine. The VASPsol implicit solvation model was deemed suitable as the objective of this study was to investigate binding energies, and water is not expected to be a reactant. In this work, the dielectric constant was set to 78.5 to simulate water at 25°C.[181] The binding energy of Cl ($E_{b,w}^{Cl}$) with the Zn(001) surface exposed to a continuum solvent medium was also calculated using Eq. 3-3, with energy values obtained in the water-solvated medium.

3.4. Results and discussion

3.4.1. Characterization of zinc electrodeposits: SEM and XRD

Figure 3-1 shows SEM micrographs of zinc electrodeposits obtained during the charging phase of the zinc half-cell from electrolytes containing different chloride concentrations under a current density of 20 mA cm^{-2}. The action of Cl is suggested as a potential reason for the morphological differences observed, with increasing concentration of chlorides further altering zinc deposit morphology. Lower $ZnCl_2$ concentration produces deposits which exhibit highly crystalline regions and contain zinc crystals generally in the range of 5–10 µm. Increasing that concentration produces crystals generally larger than 10 µm, with multiple zinc clusters and lower uniformity and smoothness. This observation provides evidence for the strong influence of chloride-based supporting electrolytes on the size and morphology of zinc electrodeposits obtained in Zn/Br RFBs during charging. Specifically, a greater chloride concentration is observed to contribute to zinc surface buckling and kinking. This influence could be *via* (a) direct action of Cl on the electrodeposited zinc surfaces, and/or (b) different zinc–chloride complexes (the types, degrees and behaviors of which are concentration-dependent).
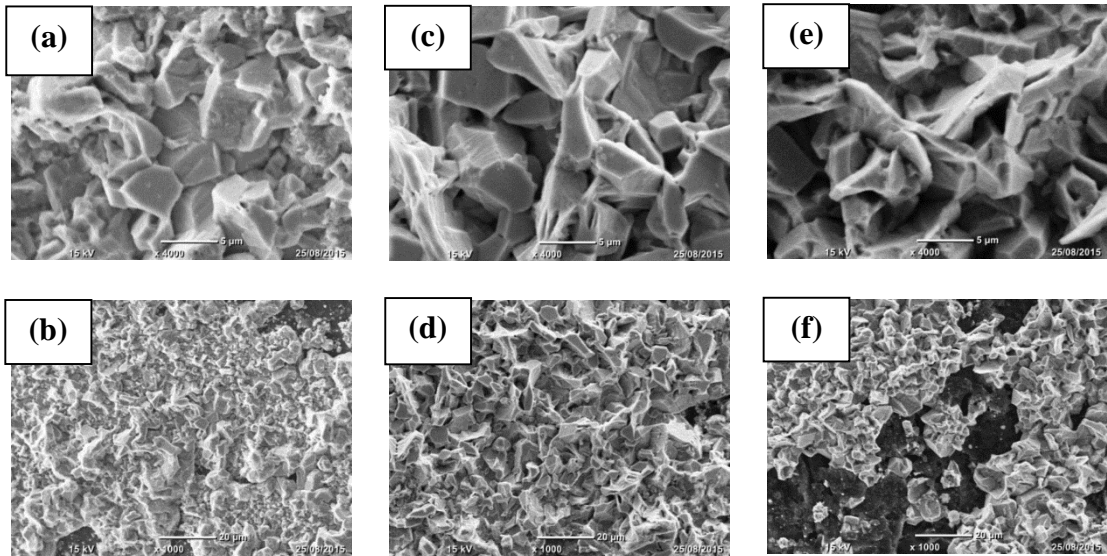
Figure 3-1. SEM images at different magnifications of zinc electrodeposited on graphite electrodes after 10 minutes of charging the Zn/Br cell at a current density of 20 mA cm^{-2} from solutions containing 2.25 M ZnBr$_2$ primary electrolyte, 0.8 M MEP and (a, b) 0.5 M, (c, d) 1 M or (e, f) 2 M ZnCl$_2$ supporting electrolyte.

Diffractograms of zinc electrodeposits obtained from electrolytes with different concentrations of ZnCl$_2$ supporting electrolyte are presented in Figure 3-2. The orientations of zinc deposits obtained from each of the solutions tested were identified using PDF card #04-014-0230 present in the PDF4+ database and crystal orientations were compared upon standardized baseline correction using software. The crystal orientations observed are consistent with the morphology observed *via* SEM. The electrolyte with the lowest ZnCl$_2$ concentration (0.5 M) produced crystals with a strong preference for the (004) orientation. Doubling that concentration to 1 M yielded electrodeposits with a (101) preferred orientation and a close secondary preference for the (002) configuration. The highest ZnCl$_2$ concentration of 2 M produced crystals which strongly favored the (101) orientation, which is consistent with a previous report that higher chloride concentrations give rise to zinc deposits favoring this configuration.[182] XRD peaks associated with the (102) and (103) orientations were also observed in some combination for all the electrolytes tested, which is consistent

46

with earlier findings using solutions containing $ZnCl_2$ and HCl.[90] Since zinc half-cell electrochemical performance (e.g. current densities) are potentially linked to crystal orientation,[90,149] promoting crystal growth with a preference for orientations associated with good performance could be an important step in future research aimed at improving battery operation. Previous investigations have shown that there can be significant variation in the preferred orientation of zinc electrodeposits depending on supporting electrolyte composition.[156] It is noted that there exists a difference when moving from zinc electrodeposits obtained from solutions of NaCl in that study and $ZnCl_2$ solutions in the present work, with the results suggesting the possibility that cations have a role in influencing the preferred zinc deposit orientation.
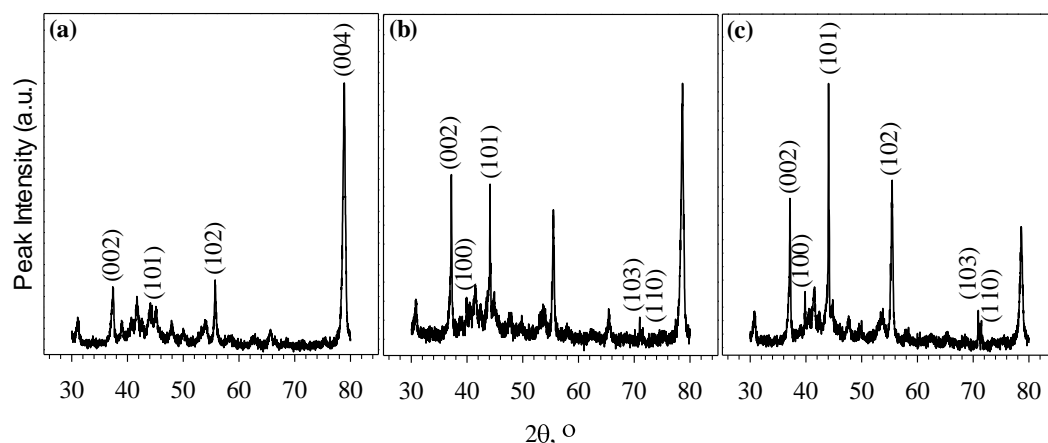
Figure 3-2. Raw diffractograms (with Miller indices of zinc peaks indicated) from XRD analysis of zinc electrodeposited on graphite electrodes after 10 minutes of charging the Zn/Br cell at a current density of 20 mA cm^{-2} from solutions containing 2.25 M $ZnBr_2$ primary electrolyte, 0.8 M MEP and (a) 0.5 M, (b) 1 M or (c) 2 M $ZnCl_2$ supporting electrolyte.

Diffraction peaks obtained for deposits from solutions containing lower concentrations of $ZnCl_2$ supporting electrolyte are slightly broader than those for higher concentrations, and analysis of the peak data showed that the peaks slightly shift towards lower 2θ values (on the order of 0.01–0.1°) as $ZnCl_2$ concentration is increased. Broadening of peaks can arise from various factors, and are primarily attributed to the size and strain within a crystal lattice[183,184] once instrument-induced

47

effects[185] are accounted for. Given the zinc morphology in Figure 3-1, it is possible that crystallite size is a more likely reason for the peak broadening observed. In the present work, broader peaks suggest the presence of non-uniform strain while negative shifts of *2θ* indicate the presence of uniform strain.[171] The non-uniform strain at low concentrations could be attributed to localized action of chlorides on some zinc clusters while a greater presence of chloride increases interactions with a higher proportion of the electrodeposited zinc.

Williamson–Hall analysis of XRD peak data indicates that both the average crystal size and strain of zinc electrodeposits obtained becomes larger as the concentration of $ZnCl_2$ supporting electrolyte increases. Compared to zinc crystals produced from solutions with 1 M $ZnCl_2$, those obtained from solutions with 0.5 M $ZnCl_2$ were about 38% smaller while electrolytes containing 2 M $ZnCl_2$ generated zinc crystals about 322% larger. This change in electrodeposited zinc crystal size based on $ZnCl_2$ concentration employed suggests a possible phenomenon whereby chlorides and/or chloride-based ionic species actively alter the morphology of electroplated zinc, either *via* direct action upon the electrodeposited zinc and/or coordination with zinc ions in solutions. Results from molecular modelling of the former phenomenon (i.e. interactions between Cl and zinc deposits) are presented in sections 3.4.2 and 3.4.3 of this work.

3.4.2. Site selectivity and surface coverage effects of Cl on Zn(001)

Given the approximately 290 mV difference in redox potentials, in the event of sudden spikes in cell potentials, there is a possibility of Cl_2 gas evolution in the bromine half-cell, hence the energetics of Cl_2 close to the surface has been studied. While there might exist some oxidation of zinc, in a flow system the continuous plating of zinc would likely result in more fresh layers of zinc present during and at the end of the

charging process, hence the choice of a pure Zn surface for this initial study. Consequently, the combined presence of Cl and an open-circuit cell (i.e. no external load applied) would result in the diffusion of Cl across to the zinc half-cell and potentially result in the interactions studied in the present work.

A preference for generating zinc electrodeposits with basal plane reflections is associated with solutions containing lower concentrations of $ZnCl_2$, as described in section 3.4.1. This preference is the basis for selecting the Zn(001) surface for molecular modelling in the present work, where the site selectivity of Cl on the Zn(001) surface was determined by calculating the binding energy, E_b^{Cl}, at different symmetrical sites.

Figure 3-3. shows top and side views of the DFT-relaxed geometries of Cl bound at $\theta_{Cl} = 0.11$ ML above the surface bridge sites (between two Zn sites), three-fold hollow fcc sites (between three Zn species, with a Zn site directly below in the second layer) and atop Zn sites (above a Zn site). Cl was found to be unstable above three-fold hollow sites containing no Zn sites directly below in the second layer (hcp sites) since the Cl spontaneously diffuses towards the closest bridge or fcc site. The binding energy of Cl with the surface exposed to a vacuum gap, $E_{b,v}^{Cl}$, and exposed to a water environment, $E_{b,w}^{Cl}$, is provided in Figure 3-3.. Table 3-1 summarizes the following information: maximum displacement of the zinc atom in the topmost layer due to the binding of Cl, r_{ClZn-d_2}, as determined from the average height of the displaced second Zn layer; the minimum separation distance between Cl bound to the Zn(001) surface, r_{Cl-Cl}; the minimum Zn–Cl bond length, r_{Zn-Cl}; and the corresponding d_{12}, $E_{b,v}^{Cl}$, and $E_{b,w}^{Cl}$ values. The minimum distance between Cl bound to the surface is not tabled as it

is consistently 8.04 Å, as indicated on the corresponding figure for coverage at 0.11 ML.

(a) Bridge
$E_{b,v}^{Cl} = 288$ kJ mol⁻¹
$E_{b,w}^{Cl} = 306$ kJ mol⁻¹

(b) fcc
$E_{b,v}^{Cl} = 286$ kJ mol⁻¹
$E_{b,w}^{Cl} = 302$ kJ mol⁻¹

(c) Top
$E_{b,v}^{Cl} = 284$ kJ mol⁻¹
$E_{b,w}^{Cl} = 327$ kJ mol⁻¹
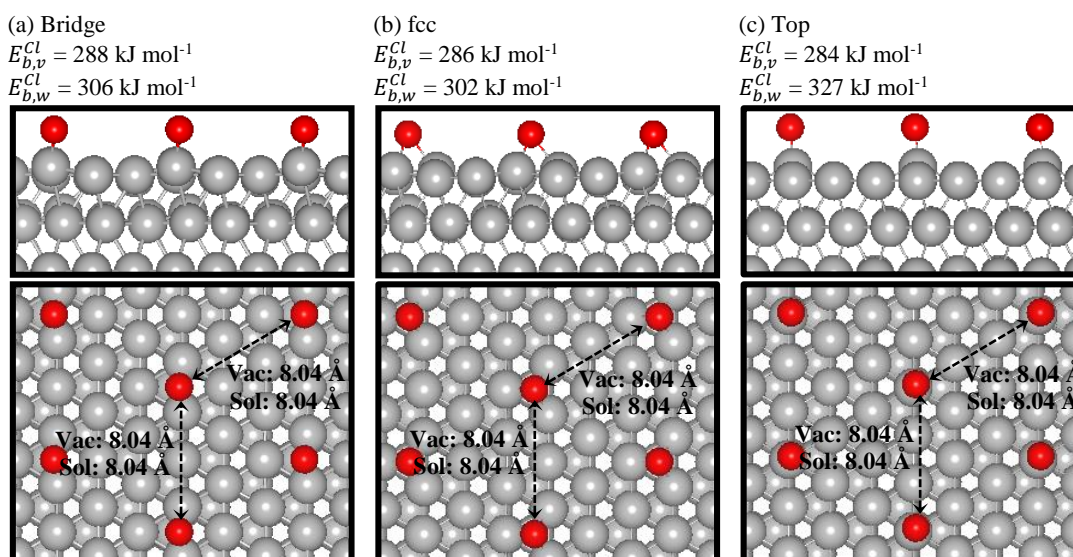
Figure 3-3. Side (images on the top row) and top (images on the bottom row) views of Cl bound to the Zn(001) surface above three different sites at $\theta_{Cl} = 0.11$ ML: a) bridge, b) fcc, and c) top. Cl and Zn atoms have been colored red and grey, respectively, for clarity. Binding energies relative to Cl under vacuum ($E_{b,v}^{Cl}$) and when water-solvated ($E_{b,w}^{Cl}$) are listed for each configuration, and Cl–Cl distances are shown. The Visualization for Electronic and Structural Analysis (VESTA)[186] software was used in the preparation of molecular configurations.

Table 3-1. $E_{b,v}^{Cl}$ and $E_{b,w}^{Cl}$, with r_{Zn-Cl}, d_{12} and r_{ClZn-d_2} distances, for bridge, fcc and atop binding configurations at 0.11 ML coverage.

Configuration	r_{Zn-Cl} (Å)	Vacuum			Solvated		
		$E_{b,v}^{Cl}$ (kJ mol⁻¹)	d_{12} (Å)	r_{ClZn-d_2} (Å)	$E_{b,w}^{Cl}$ (kJ mol⁻¹)	d_{12} (Å)	r_{ClZn-d_2} (Å)
Bridge	2.59	288	2.63	3.04	306	2.65	2.98
fcc	2.75	286	2.63	2.88	302	2.64	2.83
Top	2.34	284	2.67	3.33	327	2.64	3.29

The $E_{b,v}^{Cl}$ at 0.11 ML is between 284–288 kJ mol⁻¹, indicating a weak preference to bind on the top, bridge and fcc sites. It was found that there exists a negligible energy barrier (<1 kJ mol⁻¹) above the endothermicity of the Cl diffusing process from one site to the other, indicating that Cl is highly mobile. This high mobility is attributed to the small differences in binding energies leading to a low energy of reaction, and a small

interaction energy between Cl species at the surface since the r_{Cl-Cl} of 8.04 Å is long enough to avoid strong surface interactions. The $E_{b,v}^{Cl}$ is in the range of 44–48 kJ mol^{-1} larger than the experimental[187,188] 240 kJ mol^{-1}, and 5–9 kJ mol^{-1} larger than the calculated (in this work) 279 kJ mol^{-1} binding energy of Cl in the $Cl_{2(g)}$ molecule, showing a preference of Cl to be bound to the Zn surface.

The binding of Cl causes vertical displacements of Zn sites resulting in a nascent buckling of the Zn(001) surface, thus reducing its uniformity. This phenomenon is quantified by comparing the vertical displacement of Zn sites closest to the surface-bound Cl against the average displacement of other Zn sites in the surface layer. The average surface Zn displacements increased only slightly (by ~0.02 Å) compared with the relaxed d_{12} interlayer distance due to the positive and negative Zn displacements. This positive and negative surface Zn displacement is more pronounced in the surface with Cl on the bridge and fcc sites as seen in Figure 3. The largest displacements are observed for Zn sites under and immediately adjacent to Cl. For instance, the distance to the second layer (r_{ClZn-d_2}) of the Zn site binding Cl is in all cases longer than the d_{12} values, with binding to the top site generating the largest Zn displacement ($r_{ClZn-d_2} = 3.33$ Å). Binding above fcc locations gives slightly longer Cl–Zn equilibrium distances ($r_{Zn-Cl} = 2.75$ Å) compared to those above bridge and top sites, which are 2.59 and 2.34 Å, respectively.

Solvation has more influence on the binding energy of Cl than on its geometrical configuration. No variations in r_{Cl-Cl} are observed and there is a slight decrease in surface Zn displacements. However, $E_{b,w}^{Cl}$ varies between 302–327 kJ mol^{-1}, which is 14–43 kJ mol^{-1} larger than under vacuum. The $E_{b,w}^{Cl}$ is 21–46 kJ mol^{-1} larger than the calculated (in this work) 281 kJ mol^{-1} binding energy of Cl in the $Cl_{2(aq)}$ molecule,

showing a preference of Cl to be bound to the Zn surface. Although the difference in $E_{b,v}^{Cl}$ between sites is near the uncertainty of our approach, the top site is thermodynamically preferred when solvent effects are included. The energy barrier above the endothermicity of reaction of Cl diffusion from one site to the other is negligible, indicating that Cl is highly mobile even in the presence of a continuum solvent environment.

The surface coverage dependence of E_b^{Cl} was analysed by increasing the number of Cl species on the (3×3) surface slab to $\theta_{Cl} = 0.22$ ML and $\theta_{Cl} = 0.33$ ML. Figure 3-4 shows top and side views of equilibrated Cl species bound to the Zn(001) surface at $\theta_{Cl} = 0.22$ ML and Table 3 provides the corresponding thermodynamic and selected geometrical parameters. It is clear from Figure 3-4 that Cl at $\theta_{Cl} = 0.22$ ML binds above bridge surface sites forming six-membered Cl rings (Figure 3-4a), in parallel rows above bridges (Figure 3-4b) and Cl in zig-zag rows above bridges and atop sites (Figure 3-4c). The distance between the closest Cl sites depends on the adsorbed configuration, but ranges between 4.30–4.82 Å in the six-membered rings, between 4.00–4.05 Å in the parallel rows and 4.11–6.27 Å in the zig-zag rows. r_{ClZn-d_2} and r_{Cl-Cl} distances, together with the relevant $E_{b,v}^{Cl}$ and $E_{b,w}^{Cl}$ values, are listed for each configuration in Table 3-2. The $E_{b,v}^{Cl}$ are between 270 and 278 kJ mol⁻¹, which again shows a weak preference for a particular binding configuration. The $E_{b,v}^{Cl}$ values at 0.22 ML are similar to the calculated DFT binding energy of Cl in $Cl_{2(g)}$, and about 6–18 kJ mol⁻¹ lower than those at $\theta_{Cl} = 0.11$ ML, indicating that interaction between surface Cl species weakens the Cl–surface binding. The decrease in $E_{b,v}^{Cl}$ as θ_{Cl} increases is due the long range interaction between surface Cl as the r_{Cl-Cl} decreases

from 8.04 Å at 0.11 ML to 4.00 Å at 0.22 ML. The interlayer surface relaxation (d_{12})

at 0.22 ML is similar to those observed at 0.11 ML.

a) Bridges in 6-membered Rings
$E_{b,v}^{Cl}$ = 278 kJ mol^{-1}
$E_{b,w}^{Cl}$ = 298 kJ mol^{-1}

b) Bridges in Rows
$E_{b,v}^{Cl}$ = 273 kJ mol^{-1}
$E_{b,w}^{Cl}$ = 293 kJ mol^{-1}

c) Tops and Bridges in Rows
$E_{b,v}^{Cl}$ = 270 kJ mol^{-1}
$E_{b,w}^{Cl}$ = 302 kJ mol^{-1}
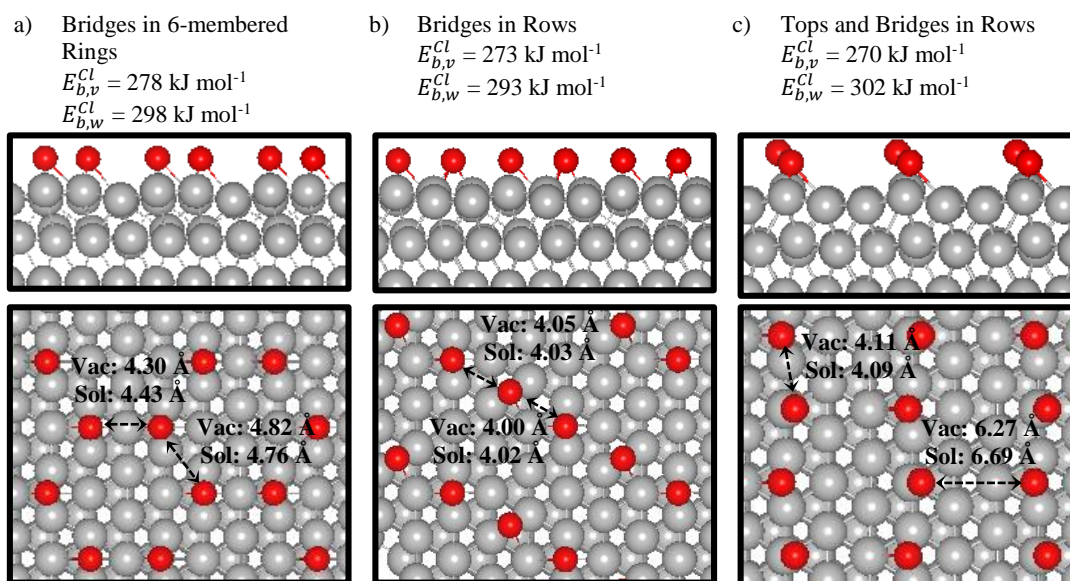
Figure 3-4. Side (images on the top row) and top (images on the bottom row) views of Cl bound to the Zn(001) surface above various sites at θ_{Cl} = 0.22 ML. Binding energies relative to Cl under vacuum ($E_{b,v}^{Cl}$) and when water-solvated ($E_{b,w}^{Cl}$) are listed for each configuration, and Cl–Cl distances are shown.

Table 3-2. $E_{b,v}^{Cl}$ and $E_{b,w}^{Cl}$, with r_{Cl-Cl}, r_{Zn-Cl}, d_{12} and r_{ClZn-d_2} distances, for binding configurations at 0.22 ML coverage.

Configuration	Vacuum					Solvated				
	$E_{b,v}^{Cl}$ (kJ mol^{-1})	r_{Cl-Cl} (Å)	r_{Zn-Cl} (Å)	d_{12} (Å)	r_{ClZn-d_2} (Å)	$E_{b,w}^{Cl}$ (kJ mol^{-1})	r_{Cl-Cl} (Å)	r_{Zn-Cl} (Å)	d_{12} (Å)	r_{ClZn-d_2} (Å)
Bridges in 6-membered Rings	278	4.30	2.46	2.69	2.99	298	4.43	2.56	2.65	2.92
Bridges in Rows	273	4.00	2.44	2.67	3.00	293	4.02	2.46	2.66	2.99
Tops and Bridges in Rows	270	4.11	2.24	2.71	3.37	302	4.09	2.31	2.69	3.36

The $E_{b,w}^{Cl}$ is between 293–302 kJ mol^{-1}, which is 15–32 kJ mol^{-1} larger than the $E_{b,v}^{Cl}$

values. Solvation effects leads to Cl species which are more strongly bound to the

surface. Similar to the above observations at θ_{Cl} = 0.11, there is a thermodynamic

preference of Cl to bind atop Zn sites. The effect of solvation on the geometrical

parameters is relatively small; d_{12} of solvated structures generally decreases slightly

53

by 0.01–0.04 Å compared to the d_{12} under vacuum, the r_{Cl-Cl} changes upon solvation by about 0.02–0.13 Å, while the range of r_{ClZn-d_2} increases from 0.22 Å to 0.25 Å. The $E_{b,w}^{Cl}$ is 12–21 kJ mol^{-1} larger than the calculated binding energy of Cl in the Cl$_{2(aq)}$ molecule, showing a preference of Cl to be bound to the Zn surface.

Figure 3-5 shows top and side views of three Cl-bound Zn(001) surface configurations at $\theta_{Cl} = 0.33$ ML. It is clear that binding in rows above top sites is favorable at this level of coverage, forming structures with raised zinc (Figure 3-5a), binding above bridge sites (Figure 3-5b), and in six-membered Cl rings with an additional central Cl (Figure 3-5c). The significant vertical displacements of Zn sites when Cl is bound to atop sites may explain the buckling of zinc electrodeposit surfaces observed experimentally in the present work. The level of buckling depends on chloride concentration within the electrolyte, with higher concentrations leading to more buckling sites on the surface. The r_{ClZn-d_2}, r_{Zn-Cl} and r_{Cl-Cl} distances, together with the relevant $E_{b,v}^{Cl}$ and $E_{b,w}^{Cl}$ values are listed in Table 3-3 for each configuration. The $E_{b,v}^{Cl}$ ranges from 249 kJ mol^{-1} to 279 kJ mol^{-1}, and are lower by up to 39 kJ mol^{-1} than those at $\theta_{Cl} = 0.11$ ML due to a surface Cl–Cl interaction that weakens the binding with the surface.

a) Tops in Rows with Raised Zn
$E_{b,v}^{Cl} = 279$ kJ mol^{-1}
$E_{b,w}^{Cl} = 293$ kJ mol^{-1}

b) Bridges and Tops in Rows
$E_{b,v}^{Cl} = 261$ kJ mol^{-1}
$E_{b,w}^{Cl} = 288$ kJ mol^{-1}

c) Tops in Rows
$E_{b,v}^{Cl} = 249$ kJ mol^{-1}
$E_{b,w}^{Cl} = 295$ kJ mol^{-1}
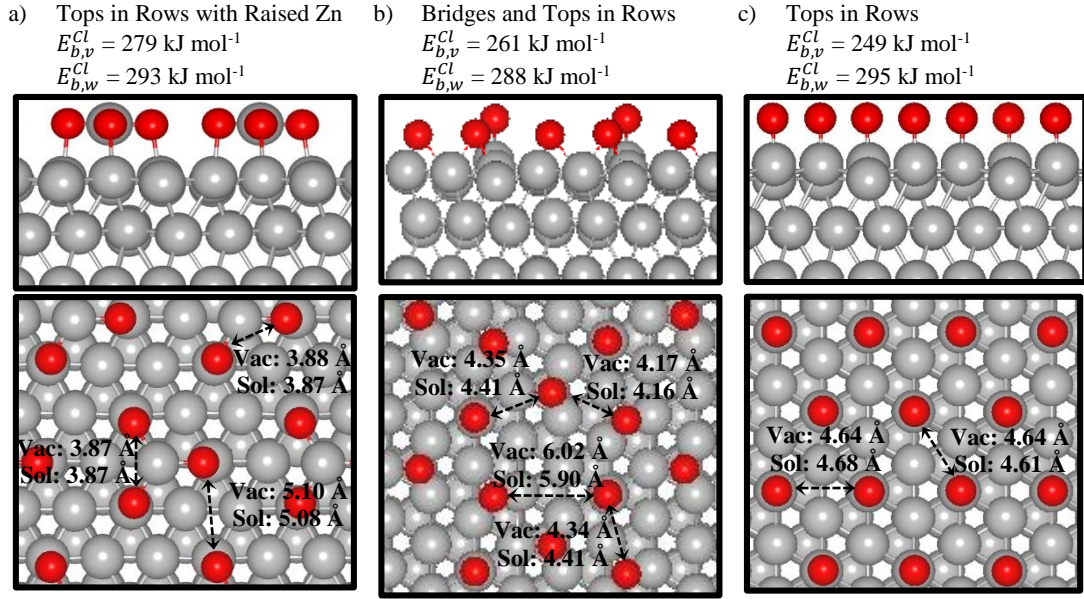
Figure 3-5. Side (images on the top row) and top (images on the bottom row) views of Cl bound to the Zn(001) surface above different sites at $\theta_{Cl} = 0.33$ ML. Binding energies relative to Cl under vacuum ($E_{b,v}^{Cl}$) and when water-solvated ($E_{b,w}^{Cl}$) are listed for each configuration, and Cl–Cl distances are shown.

Table 3-3. $E_{b,v}^{Cl}$ and $E_{b,w}^{Cl}$, with r_{Cl-Cl}, r_{Zn-Cl}, d_{12} and r_{ClZn-d_2} distances, for binding configurations at 0.33 ML coverage.

Configuration	Vacuum					Solvated				
	$E_{b,v}^{Cl}$ (kJ mol^{-1})	r_{Cl-Cl} (Å)	r_{Zn-Cl} (Å)	d_{12} (Å)	r_{ClZn-d_2} (Å)	$E_{b,w}^{Cl}$ (kJ mol^{-1})	r_{Cl-Cl} (Å)	r_{Zn-Cl} (Å)	d_{12} (Å)	r_{ClZn-d_2} (Å)
Tops in Rows with Raised Zn	279	3.87	2.23	2.87	5.42	293	3.87	2.23	2.88	5.68
Bridges and Tops in Rows	261	4.17	2.21	2.72	3.39	288	4.16	2.29	2.69	3.30
Tops in Rows	249	4.64	2.20	2.71	3.19	295	4.61	2.27	2.69	3.18

When a Zn is coordinated to three Cl species, the Zn is lifted from the surface to form a stable configuration with the highest $E_{b,v}^{Cl}$, as seen in Figure 3-5a, and the largest r_{ClZn-d_2} displacement of 5.42 Å. Such cavitation actions are of great interest and relevance to Zn/Br battery operation, and are hence studied in greater detail in section 3.4.3. The interlayer distance relaxations of the first and second layers at 0.22 and 0.33ML are similar to those at 0.11ML, while r_{Cl-Cl} varies from 3.87–4.64 Å for structures at 0.33 ML under vacuum.

Consistent with behavior at lower coverages, Cl binding above top sites at 0.33 ML is more favorable than those with binding above bridges and fcc sites when the Cl-bound Zn(001) system is solvated. This tendency once again prompts migration of Cl to bind above atop sites. $E_{b,w}^{Cl}$ ranges from 288–295 kJ mol^{-1}, which is 9–44 kJ mol^{-1} larger than that under vacuum. d_{12} of solvated structures change slightly by 0.01–0.03 Å from structures under vacuum. Solvation slightly changes r_{Cl-Cl} by 0.01–0.03 Å, while changes to r_{ClZn-d_2} vary from 0.01–0.16 Å.

It is observed that Cl are no longer bound to the surface when the surface coverage is above 0.33 ML. This saturation behavior of Cl above $\theta_{Cl} = 0.33$ ML is similar to previous reports from studies of Cl over Au(111)[165,166] and Cu(111)[167] surfaces.

3.4.3. Reactions of Cl above the Zn(001) surface

The formation of Cl$_2$ at $\theta_{Cl} = 0.22$ ML and the formation of ZnCl$_3$ at $\theta_{Cl} = 0.33$ ML as possible de-chlorination paths from the Cl-Zn(001) surfaces was studied. The desorption of Cl$_2$ at $\theta_{Cl} = 0.22$ ML was studied with an initial configuration with Cl forming zig-zag rows above bridge and atop sites (Figure 3-4c) and a final configuration with Cl$_2$ equilibrated far above (4.90 Å) the Zn(001) surface. The desorption process is endothermic by 303 kJ mol^{-1} and 262 kJ mol^{-1} in the presence and in the absence of solvation effects, respectively, with negligible energy barriers above the endothermicity of the reaction. Consequently, Cl-Zn(001) is structurally more stable than bare Zn(001) with Cl$_2$ present above the surface, and Cl$_2$ formation from the Cl-bound Zn(001) is thermodynamically and kinetically limited. Our test calculations showed that relaxing the Cl$_2$ molecule starting from a distance of less than 3.7 Å from the surface leads to spontaneous dissociation at the surface. This dissociative behavior indicates that although Cl$_2$ is stable if located beyond a certain distance from the Zn(001) surface, there is no molecular adsorption of Cl$_2$ as it moves

closer to the surface. Similar dissociative and subsequent binding interactions have been reported for the case of chlorine with graphene.[164]

This zinc-removal process as $ZnCl_3$ is studied at $\theta_{Cl} = 0.33$ ML when three Cl are bound to the same zinc site, beginning from the structure shown in Figure 5c and moving into the configuration showed in Figure 5a. Figure 3-6 shows the energy minimum pathway of Cl converging above the same zinc site and subsequently displacing a Zn site away from the surface. Only three Cl are shown in this example to increase clarity of this process. Top and side views are shown for the initial (Figure 3-6a), transition (Figure 3-6b) and final (Figure 3-6c) configurations. The equilibrium Zn–Cl bond length between Cl and the raised zinc atom in the final structure is 2.23 Å, r_{ClZn-d_2} is 5.67 Å, and the energy barrier for this process is 21 kJ mol^{-1} when solvated and 1 kJ mol^{-1} under vacuum. The $E_{b,v}^{Cl}$ is 279 kJ mol^{-1} when the nascent $ZnCl_3$ is 3 Å above the Zn(001) cavity, decreasing to 257 kJ mol^{-1} when that vertical distance is 4 Å, and to 199 kJ mol^{-1} at 5 Å. However, $E_{b,w}^{Cl}$ remains constant at ~291 kJ mol^{-1} even as that distance between nascent $ZnCl_3$ and the Zn(001) surface cavity is increased from 3–5 Å. The removal of zinc from the Zn(001) surface is exothermic under vacuum and creates structures which are 89 kJ mol^{-1} more stable, and slightly endothermic when solvent effects are included, 9 kJ mol^{-1}. This indicates that above $\theta_{Cl} = 0.33$ ML and with small Cl–Cl separation distances, especially when there are more than two Cl bound to the same zinc, it is thermodynamically and kinetically possible for the zinc atom to be removed and a vacancy created on the Zn(001) surface. This finding of a changing metal surface *via* action of Cl is similar to that of a recent study on the removal of Cu from Cu(111) as CuCl molecules due to the action of Cl.[189]

a) Initial, $E_{r,v} = 0$ kJ mol^{-1}
$E_{r,w} = 0$ kJ mol^{-1}

b) Transition, $E_{r,v} = +1$ kJ mol^{-1}
$E_{r,w} = +21$ kJ mol^{-1}

c) Final, $E_{r,v} = -89$ kJ mol^{-1}
$E_{r,w} = +9$ kJ mol^{-1}
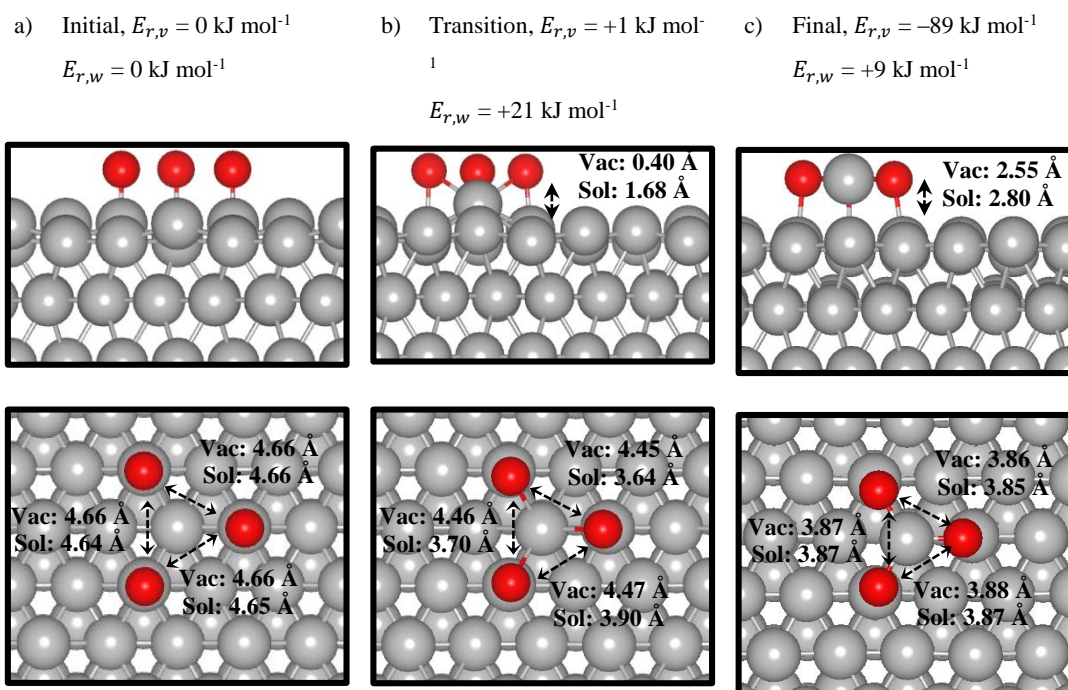
Figure 3-6. Cl converging above the same zinc atom at $\theta_{Cl} = 0.33$ ML and raising it above the Zn(001) surface. Side (images on the top row) and top (images on the bottom row) views are shown for the: a) initial structure with relative binding energy under vacuum and when solvated ($E_{r,v}$ and $E_{r,w}$, respectively) set to 0 kJ mol^{-1}, b) transition structure with $E_{r,w}$ of +21 kJ mol^{-1} and $E_{r,v}$ of +1 kJ mol^{-1} compared to initial structure, and c) final structure of ZnCl$_3$ raised above the Zn(001) cavity with overall $E_{r,w}$ of +9 kJ mol^{-1} and $E_{r,v}$ of −89 kJ mol^{-1} compared to initial structure. Only three Cl are shown in this figure to increase clarity of this process. Zero of binding energy is set for that of Cl initially located one atom space away from target zinc atom while all other values are expressed relative to it.

The binding of Cl to the Zn(001) surface above top sites leading to increased buckling of the zinc surface at higher chloride concentrations provides some explanation towards some experimentally observed phenomena at the zinc-side electrode in a previous study (described in Chapter 4).[156] The size of ions forming the electrical double-layer (EDL) influences the degree of electrode coverage, thereby influencing the rates of reactions occurring at the electrode surface,[151] with larger ions forming EDLs with larger effective thickness.[190] It is proposed that the presence of chlorides in high concentrations leads to dense packing of EDL species, which in turn leads to pronounced capacitive behavior and lower zinc half-cell energy efficiency. Furthermore, the rearrangement of electrodeposited zinc on the surface due to the

action of Cl is a potentially contributing factor towards lower charge efficiency due to Coulombic losses, possibly via removal of zinc atoms from the surface.

3.5. Chapter conclusions

Zinc electrodeposits obtained during the charging phase of a Zn/Br RFB were characterized to investigate the possibility of chloride-based supporting electrolytes influencing zinc-side processes. The presence of chlorides decreases the crystallinity and morphology of zinc electrodeposits compared to those obtained from pure primary electrolytes, as observed *via* SEM. XRD showed that increasing chloride concentration changes the preferred crystal orientation of zinc from basal orientations to the (101) configuration. The findings presented in this work demonstrated how chloride-based supporting electrolytes are able to significantly influence electrodeposition behavior in the zinc half-cell of Zn/Br RFBs.

DFT calculations indicate that Cl preferentially binds to the Zn(001) surface above bridge, fcc and top sites. Accounting for solvent effects (in this case, water at 25°C), $E_{b,w}^{Cl}$ and $E_{b,v}^{Cl}$ range from 288–327 kJ mol^{-1} and 249–288 kJ mol^{-1}, respectively, for $\theta_{Cl} = 0.11$–0.33 ML. Cl is able to migrate across the Zn(001) surface with relatively low energy barriers and Cl–Zn(001) binding energies decrease with higher surface coverage levels. Zinc could be removed from the Zn(001) surface by Cl at 0.33 ML, creating cavities on the surface. The energy barrier for this process at $\theta_{Cl} = 0.33$ ML is 21 kJ mol^{-1} when water-solvated and 1 kJ mol^{-1} under vacuum. Additionally, the de-chlorination of Cl-bound Zn(001) to form Cl$_2$ is unfavorable as it results in the formation of structures which are 303 kJ mol^{-1} and 262 kJ mol^{-1} less stable when water-solvated and under vacuum, respectively. Zinc removal is of relevance to Zn/Br battery operation, as it raises concerns regarding the possibility of high concentration of

chlorides damaging and removing electrodeposited zinc during/after charging, thereby reducing battery performance due to coulombic losses.

DFT predictions of Cl potentially contributing to buckling and damaging of zinc surfaces are consistent with physical observations from SEM and XRD analyses. The present DFT work is carried out for Cl under vacuum and in the water-solvated phase, and provides an important foundation towards explaining phenomena observed within more complicated aqueous systems in the presence of other electrolyte species. It is expected that these findings will prompt further research on alternative supporting electrolytes which do not bind as strongly as Cl does to the electrodeposited zinc surface and instead positively influence zinc plating and stripping processes during the charging and discharging phases of the Zn/Br battery, respectively. Although the present study focusses on the interactions between Cl and Zn(001), it is also potentially relevant and adaptable to other types of flow batteries and systems involving metal deposition from electrolytes containing halogens, as well as corrosion of zinc surfaces due to the action of Cl.

The next chapter builds upon the findings and implications of this study by investigating potential alternatives to chloride-based electrolytes for improved zinc half-cell performance.

4. The Influence of Supporting Electrolytes on Zinc Half-Cell Performance

4.1. Chapter abstract

Five supporting electrolytes were studied for their viability as alternatives in the zinc half-cell of a zinc/bromine (Zn/Br) flow battery. The secondary electrolytes studied included sodium salts of the following anions: Br^-, SO_4^{2-}, $H_2PO_4^-$ and NO_3^-, which were compared against the conventionally employed Cl^-.

Cyclic voltammetry and Tafel analysis showed improved electrochemical performance from electrolytes containing $NaBr$, Na_2SO_4 and NaH_2PO_4. Consequently, these chemicals are proposed as potential alternatives in future Zn/Br design work. Electrochemical impedance spectroscopy revealed that the lowering of charge-transfer resistance and diffusion limitation was the contributing reason towards improved performance from those electrolytes.

Scanning electron microscopy and X-ray diffraction of zinc electrodeposits obtained during charging showed the type of supporting electrolyte present alters zinc crystallinity. Generation of smaller crystals was related to observations of good half-cell performance during voltammetry. Mossy deposits were linked with higher nucleation overpotentials between zinc plating/de-plating. The well-performing Na_2SO_4 supporting electrolyte produced mossy deposits, suggesting that contrary to common assumption, such deposition behavior is possibly unrelated to poor zinc-side performance.

While the proposed compounds are intended for Zn/Br flow battery applications, they are possibly adaptable to other types of flow batteries utilizing the Zn^{2+}/Zn redox couple.

4.2. Introduction

The work presented in this chapter builds upon the findings presented in Chapter 3 by searching for suitable alternatives to chloride-based supporting electrolytes in order to improve Zn/Br system performance. As discussed in earlier chapters, dendrite formation during the charging phase has long been a major observation and source of concern during the design of RFBs which employ zinc electrodeposition, with various strategies employed to minimize this issue.[41,45,67,69] Dendrites increase operational risks by causing problems such as short circuiting of cells. It is also beneficial to promote efficient electrodeposition and stripping of zinc during the charge and discharge phases, respectively, in order to maximize the coulombic efficiency of the system. Further improvements can be achieved by minimizing undesirable side-reactions which cause coulombic losses in the system.

An important factor influencing zinc electroplating behavior is the electrolyte composition.[191] This dependency includes the type and amount of supporting electrolyte used in the Zn/Br battery to maintain conductivity when the primary electrolyte (i.e. $ZnBr_2$) is depleted during charging. The acidic nature of Zn/Br electrolytes limits the use of chemicals which would significantly alter the narrow working pH range.[45] Chloride-based secondary electrolytes are conventionally used in Zn/Br systems,[43,50,57,150] including bench-scale testing.[192] Zinc electrodeposition and behavior in solutions containing chlorides[90,155,159,193–195] has also been studied for industrial electroplating applications. However, it is possible that chlorides have a negative influence on electrodeposited zinc in the system due to the corrosive action of the former on the latter. This challenge has prompted work to identify suitable alternatives, such as the use of perchlorates.[157] The effects of sulfates[196–200] on zinc plating have also been studied and could potentially be adapted for use in Zn/Br

electrolytes. While the corrosion of zinc, whether accelerated by the presence of chloride ions or not, could be minimal when the battery is operating (i.e. cathodic protection), the electrodeposited zinc might be susceptible to corrosion during open-circuit conditions (i.e. no load applied). Consequently, it is of interest to optimize the type and properties of supporting electrolyte employed in the next generation of Zn/Br batteries in order to improve performance and thus the uptake of this system for utility-scale electrical energy storage.

This interest provides motivation for the present work which focusses on improving the electrochemical performance of the zinc half-cell, both in the bulk electrolyte and at the electrode–electrolyte interface. Four Na-based supporting electrolytes (Br^-, SO_4^{2-}, $H_2PO_4^-$ and NO_3^-) are assessed against a chloride-based solution to study the influence of these compounds on the Zn^{2+}/Zn couple. These electrolytes are selected as part of a targeted approach exploring ions present in conventional solutions (Br^-, Cl^-) as well as common anions which would not lead to the formation of alkaline Zn/Br electrolytes (SO_4^{2-}, $H_2PO_4^-$ and NO_3^-), i.e. supporting electrolytes which would maintain an acidic working environment. The implications of the findings of this work are potentially relevant to other RFBs containing this redox and similar systems involving metal electrodeposition.

4.3. Methodology

4.3.1. Electrolyte preparation

Testing solutions containing 2.25 M zinc bromide ($ZnBr_2$, Merck) primary electrolyte with 0.5 M of a sodium-based supporting electrolyte were prepared. The supporting electrolytes included the following compounds: sodium bromide (NaBr, Merck, 99%), sodium sulfate (Na_2SO_4, Mallinckrodt, 100%), sodium dihydrogen phosphate

dihydrate (NaH$_2$PO$_4$·2H$_2$O, VWR, 99.7%), sodium chloride (NaCl, Ajax, 99.9%) and

sodium nitrate (NaNO$_3$, Merck, 99%). 0.8 M N-ethyl-N-methyl-pyrrolidinium

bromide was used as the bromine sequestering agent based on the 0.8–1 M

concentration range conventionally used in modern Zn/Br systems.[45,81] Ionic

conductivity was measured using a labCHEM-CP (TPS Ltd., Brisbane, Australia) for

each testing solution prepared and listed in Table 4-1 together with a numerical

shorthand used to refer to each supporting electrolyte.

Table 4-1. Properties and numerical shorthand for supporting electrolytes studied in this work.

Supporting electrolyte	Numerical shorthand	Conductivity (mS cm^{-1})
Na$_2$SO$_4$	**1**	54.0 ± 0.2
NaBr	**2**	47.8 ± 0.2
NaCl	**3**	48.2 ± 0.6
NaH$_2$PO$_4$	**4**	43.2 ± 0.9
NaNO$_3$	**5**	49.7 ± 0.3

4.3.2. Zinc half-cell electrochemical tests

A three-terminal glass cell was used for electrochemical half-cell studies, with a

0.3 cm^2 graphite-coated conductive carbon plastic working electrode (RedFlow Ltd.,

Brisbane, Australia), vitreous carbon rod counter electrode and silver–silver chloride

(Ag/AgCl/3.4 M KCl) reference electrode. Solutions were bubbled with nitrogen gas

and maintained under an inert atmosphere to remove dissolved oxygen prior to half-

cell testing. A Bio-Logic SP-300 potentiostat was used for all electrochemical tests

and the EC-Lab (version 10.32) data acquisition software was used to extract, process

and fit the results obtained. Cyclic voltammetry (CV) was carried out between 0 V to

– 1 V *vs* Ag/AgCl at 30 mV s^{-1}, with all scans stabilizing by the sixth cycle. Tafel

analysis was carried out using linear sweep voltammetry (LSV) data obtained between

–0.95 V and –0.60 V *vs* Ag/AgCl at 2 mV s^{-1}. Values of current densities obtained

using this setup show good reproducibility within ±2% (standard deviation of ±0.04

mA cm⁻²) for CV and within ±1% (standard deviation of

±0.001 mA cm⁻²) for LSV. The equations used for Tafel fitting on the linear regions

of Tafel plots (logarithm of the magnitude of current density against the working

electrode potential *vs* Ag/AgCl) are (Eqs. 4-1–4-2):

$$log\ |i| \approx \frac{E - E_0}{\beta_a} + \log\ (i_0),\ \text{for}\ E >> E_0 \qquad \text{[Eq. 4-1]}$$

$$log\ |i| \approx \frac{E_0 - E}{\beta_c} + \log\ (i_0),\ \text{for}\ E << E_0 \qquad \text{[Eq. 4-2]}$$

where i is the current density of the Zn^{2+}/Zn reaction, i_0 the exchange current density,

E the working electrode potential *vs* Ag/AgCl, E_0 the potential *vs* Ag/AgCl at which i_0

occurs. The Tafel constants β_a and β_c are the anodic and cathodic reaction coefficients,

respectively. The polarization resistance (R_p) at E_0 is calculated as (Eq. 4-3):

$$R_p = \frac{\beta_a\ \beta_c}{i_0\ (\beta_a + \beta_c)\ ln10} \qquad \text{[Eq. 4-3]}$$

The fitted Tafel parameters presented in this work include i_0, E_0, R_p, β_a and β_c.

Potentiostatic electrochemical impedance spectroscopy (EIS) scans were carried out

by holding the working electrode at –1 V *vs* Ag/AgCl for 1 minute to generate zinc

electrodeposits on the surface, followed by EIS at the open-circuit potential (OCP)

with 10 mV perturbation from 200 kHz to 50 mHz. External interferences were

minimized by the use of a custom-built Faraday cage and all experiments were carried

out at laboratory conditions of 25±1°C. Differential capacitance tests were also carried

out as based on a method described in earlier literature[201] to study relative capacitive

behavior arising from ion assembly at the electroplated zinc surface during battery

charging (thus forming an interfacial electrical double-layer, EDL). The electroplated

zinc surface (after 1 minute of charging) was scanned between –0.2 V and +0.2 V *vs*

OCP at 0.1 V steps, beginning from the OCP in the positive direction, followed by the negative direction. EIS scans were carried out at 20 different frequencies between 200 kHz and 100 Hz to identify a suitable frequency for comparing the capacitive behavior of EDLs formed in each of the solutions studied. Differential capacitance was calculated using the following equation[201] (Eq. 4-4):

$$C = - (\omega Z_{im})^{-1} \qquad\qquad\qquad \text{[Eq. 4-4]}$$

where C is the differential capacitance calculated for a particular frequency, ω the angular frequency of the alternating current (ac) perturbation during the impedance scan, and Z_{im} the imaginary part of the impedance. Higher frequency leads to lower differential capacitance, hence it is necessary to select a suitable frequency which does not distort the impedance measurements and allows for clear comparison of trends in differential capacitance.[201] On this basis, 1 kHz was selected as a suitable frequency for such comparisons to be made.

4.3.3. Zinc electrodeposit preparation and characterization

Zinc was electrodeposited for 10 minutes from each electrolyte onto the graphite-coated working electrode using a Neware battery cycler operating at a current density of 20 mA cm^{-2}. The solution bath was magnetically stirred (300 rpm) to maintain homogeneity of the solution during this process. Electrodeposits were analyzed *via* scanning electron microscopy (SEM) and X-ray diffraction (XRD). SEM imaging was performed with a JCM-6000 NeoScope Benchtop SEM while XRD scans were carried-out between 30–80° at 5° min^{-1} and 0.02° step size using a Shimadzu S6000 with a Cu-Kα target operating at 40 kV and 30 mA. Analysis of XRD data was carried out using the PDF4+ software database.

4.4. Results and discussion

4.4.1. CV and Tafel analysis of the zinc redox

Voltammograms from zinc half-cell CV tests of solutions containing the various supporting electrolytes are presented in Figure 4-1. The following electrochemical parameters are calculated for the reduction (*red*) and oxidation (*ox*) scans, with relevant ratios of values during oxidation and reduction expressed as half-cell efficiencies (*eff*): highest-magnitude current (*j*), maximum power (*P**), charge (*Q*) and energy (*E**) densities, and nucleation overpotential (NOP) for zinc electrodeposition. The magnitude of potentials ($|j_{ox\text{-}E}|$) at which each electrolyte produced the stripping peak was also recorded. These values are listed in

Table 4-2. *P** and *E** are calculated with Ag/AgCl as a reference. While power and energy are typically listed for full cells, they are presented here for comprehensive comparison of electrolytes. NOP is calculated for zinc electrodeposition and stripping in that half-cell based on the difference in deposition (DP) and cross-over potentials (COP), as seen in the voltammetry profiles.
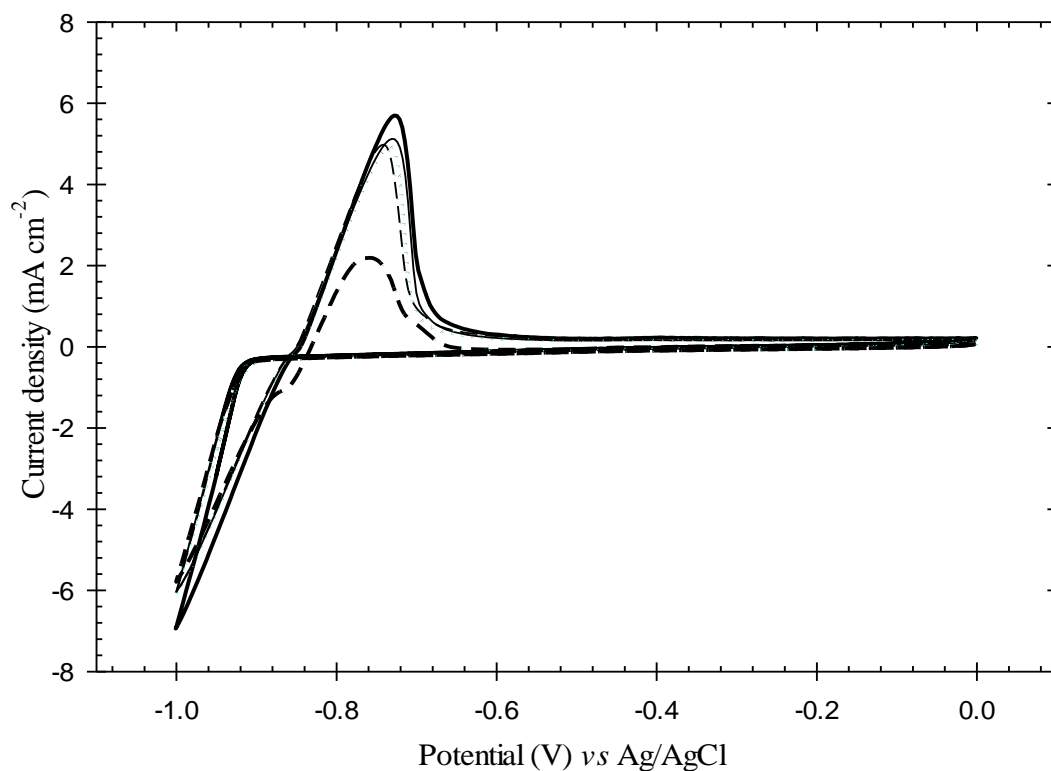
Figure 4-1. Zinc half-cell CV for solutions containing 0.5 M of the secondary electrolytes studied: **1** Na₂SO₄ (thin solid line), **2** NaBr (thick solid line), **3** NaCl (dotted line), **4** NaH₂PO₄ (thin dashed line) and **5** NaNO₃ (thick dashed line).

Table 4-2. Zinc half-cell CV comparing the electrochemical performance of supporting electrolytes.

	Na₂SO₄ (**1**)	NaBr (**2**)	NaCl (**3**)	NaH₂PO₄ (**4**)	NaNO₃ (**5**)
j_{red}, mA cm^{-2} [a]	-6.04	-6.94	-6.07	-6.07	-5.79
j_{ox}, mA cm^{-2} [b]	5.12	5.70	4.94	4.98	2.19
$j_{ox\text{-}E}$, mV	-731	-728	-734	-741	-758
Q_{red}, mC cm^{-2}	-25.4	-30.4	-26.7	-25.5	-27.4
Q_{ox}, mC cm^{-2}	20.0	23.4	18.9	20.0	6.5
Q_{eff}, %	79%	77%	71%	79%	24%
P^*_{red}, mW cm^{-2}	6.0	6.9	6.1	6.1	5.8
P^*_{ox}, mW cm^{-2}	3.7	4.2	3.6	3.7	1.7
P^*_{eff}, %	62%	60%	60%	61%	29%
E^*_{red}, mJ cm^{-2}	23.8	28.6	24.9	23.9	24.9
E^*_{ox}, mJ cm^{-2}	13.3	15.0	12.1	12.8	4.9
E^*_{eff}, %	56%	52%	49%	53%	20%
DP, mV	-926	-917	-919	-924	-916
COP, mV	-859	-855	-861	-861	-838
NOP, mV	67	62	58	63	78

[a]Standard deviation of ±0.03 mA cm^{-2} using this setup.
[b]Standard deviation of ±0.04 mA cm^{-2} using this setup.

The conventional chloride option (**3**) generally performed comparably to, or poorer than, alternative supporting electrolytes employing sulfate (**1**), bromide (**2**) or phosphate (**4**). Electrolytes containing **2** exhibited the best electrochemical performance during both the deposition and stripping scans with the highest magnitude values. The presence of **1** gave the highest energy efficiency while relatively similar current and power efficiencies were obtained for electrolytes utilizing **1**–**4**. The difference in voltammetry profiles in the presence of various anions suggest the influence of more than just zinc ions participating in the electrodeposition process. The generally comparable (P^*_{eff}) or lower (Q_{eff}, E^*_{eff}) efficiencies calculated for solutions with **3** suggest a possible interference with zinc ions in solution and/or electrodeposited zinc by chlorides compared to other supporting species. Higher bromide concentration led to improved zinc-side performance despite bromide anions being expected to behave as spectators in the zinc half-cell which do not participate in redox reactions there. This observation, combined with the mid-range conductivity of solutions with **2** compared to other electrolytes, suggests that increased bromide concentration could be more beneficial to the zinc electrodeposition process than chlorides, and require closer attention for such systems. It was noted that electrolytes which produced stripping peaks at comparatively lower $|j_{ox\text{-}E}|$ also gave better electrochemical performance than those which produced higher $|j_{ox\text{-}E}|$. Electrolytes utilizing nitrates (**5**) gave the worst performance during the oxidation scan despite producing similar values to the other electrolytes during charging. This is possibly due to a competing reaction which is observed as small peak in the reverse scan at about −860 mV *vs* Ag/AgCl. This side reaction is proposed to be hydrogen generation, based on electrochemical (CV, EIS, Tafel) and physical (SEM) results in subsequent sub-sections. Electrolytes

with **2**–**4** produced relatively similar NOP while a slightly higher value was recorded for **1** and the highest value for **5**.

Zinc half-cell Tafel plots for the different supporting electrolytes studied are presented in Figure 4-2. Corresponding Tafel fitting parameters including the exchange current density (i_0), the potential (E_0) at which i_0 occurs, polarization resistance (R_p), and the anodic (β_a) and cathodic (β_c) beta constants are listed in Table 4-3. With the exception of solutions containing **5**, the electrolytes studied generally maintained a similar trend in the relative magnitudes of Tafel parameters as their relative performance during CV tests. The presence of **1**, **2** and **4** produced higher i_0 than **3** due to lower R_p values. The presence of two inflexion points in the Tafel plot for **5** confirmed CV observations that a competing side-reaction is the cause of poor performance during the discharge phase of the zinc half-cell. Hydrogen evolution is common in conventional Zn/Br batteries and usually suppressed, and is consequently suggested as being the side-reaction on the zinc surface, combined with observations from SEM micrographs presented in section 4.4.3, below. While it is also possible that NO or HNO_2 might be forming in the cell due to the slightly less-positive reduction potentials of those reactions compared to that of the bromine/bromide redox, such formations would occur in the bromine half-cell.
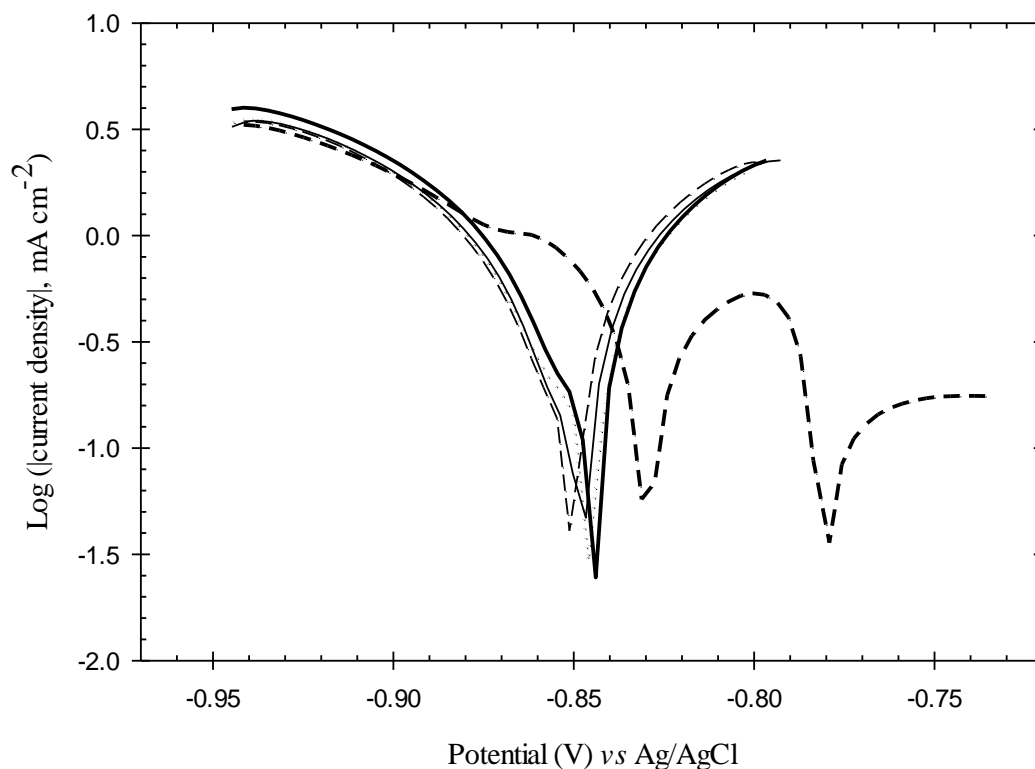
Figure 4-2. Zinc half-cell Tafel plots for solutions containing 0.5 M of the secondary electrolytes studied: **1** Na_2SO_4 (thin solid line), **2** NaBr (thick solid line), **3** NaCl (dotted line), **4** NaH_2PO_4 (thin dashed line) and **5** $NaNO_3$ (thick dashed line).

Table 4-3. Tafel fitting parameters calculated for each electrolyte studied in the zinc half-cell.

	Na_2SO_4 (**1**)	NaBr (**2**)	NaCl (**3**)	NaH_2PO_4 (**4**)	$NaNO_3$ (**5**)	
i_0, mA cm^{-2}	0.657	0.620	0.447	0.643	1.569	-0.187
E_0, mV	-848	-845	-845	-850	-829	-781
β_a, mV dec^{-1}	84	71	58	73	inf	inf
β_c, mV dec^{-1}	112	109	95	110	131	22
R_p, Ω	96	91	106	90	110	110

4.4.2. Impedance spectroscopy of the zinc half-cell

Nyquist plots from potentiostatic EIS of the various electrolytes show single time-constant behavior and are presented in Figure 4-3, together with an equivalent circuit model (see inset). This simple circuit contains the following elements: R_1 represents solution resistance between the reference and working electrodes, R_2 represents charge-transfer resistance of the Zn^{2+}/Zn redox reaction, C_2 represents capacitance of

the electrical double-layer at the electrode surface and W_2 represents Warburg diffusion limitations of the redox species. Values for each of the solutions are presented in Table 4-4. The Nyquist plot scale was chosen to show subtle differences in the depressed semicircular arcs of the EIS spectra obtained. While it is noted that replacing/adding more circuit elements might result in a better fit of the obtained spectra, the simplest equivalent circuit model with one time constant characteristic and capacitor was utilized as a first-pass fitting for directly attributing a physical/electrochemical process before other more sophisticated equivalent circuit models with other elements were used.
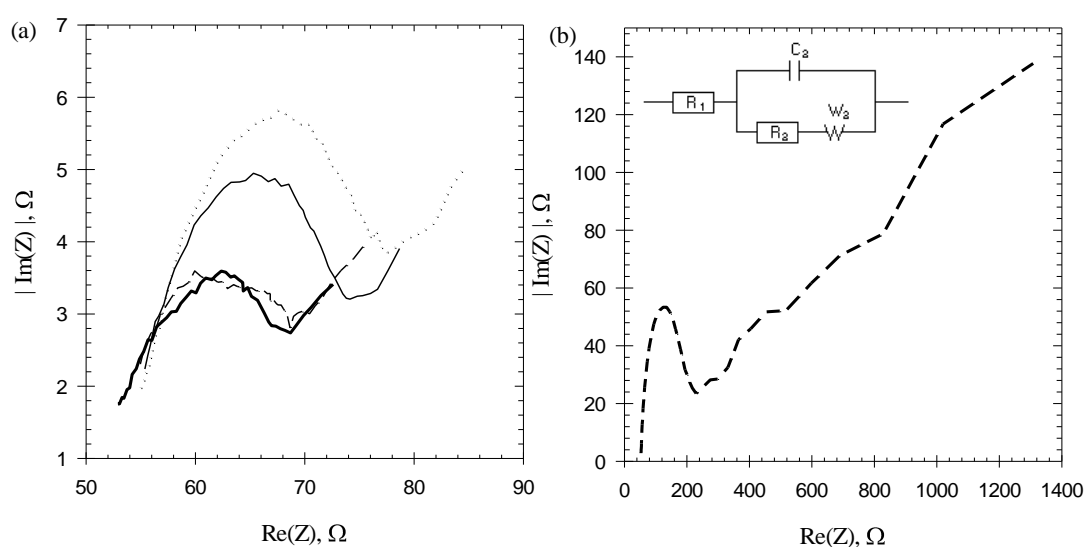
Figure 4-3. Zinc half-cell Nyquist curves for solutions containing 0.5 M of the secondary electrolytes studied: (a) **1** Na_2SO_4 (thin solid line), **2** NaBr (thick solid line), **3** NaCl (dotted line), **4** NaH_2PO_4 (thin dashed line) and (b) **5** $NaNO_3$ (thick dashed line). Inset of (b) shows the equivalent circuit model used to simulate each impedance curve.

Table 4-4. Equivalent circuit element values (with relative errors) for EIS modelling of the different supporting electrolytes studied.

	Na_2SO_4 (**1**)	NaBr (**2**)	NaCl (**3**)	NaH_2PO_4 (**4**)	$NaNO_3$ (**5**)
R_1, Ω	56.8 ± 0.3	54.6 ± 0.3	57.4 ± 0.3	56.0 ± 0.3	57.2 ± 0.3
C_2, μF	238 ± 35	366 ± 73	289 ± 37	186 ± 36	47 ± 68
R_2, Ω	12.8 ± 0.4	9.3 ± 0.4	14.7 ± 0.4	9.8 ± 0.4	122.5 ± 0.4
W_2, $\Omega.s^{-0.5}$	4.3 ± 0.2	3.9 ± 0.2	5.6 ± 0.2	4.3 ± 0.2	158 ± 0.3

Similar solution resistances (R_1) are observed for the electrolytes studied, with a maximum difference of 2 Ω. The lowest R_1 value was calculated for those using **2**, suggesting improved mobility of ions in the bulk electrolyte for this solution compared to others. It is possible that the small solution resistance of 2 Ω can be considered negligible in view of the cell configuration/electrode positions, with electrochemical performance differences attributed to the charge-transfer resistance and diffusion limitation. Solutions containing **1**, **2** and **4** gave better electrochemical performance during CV tests due to lower resistances associated with charge-transfer (R_2) and Warburg diffusion limitation (W_2), as determined *via* EIS. The difference in charge transfer resistances is potentially attributed to the influence of supporting species on the zinc redox energy barrier, with solutions containing **1**, **2** and **4** lowering that barrier compared to that of those with **3**.

A wide range of capacitance (C_2) values were calculated for the electrolytes, with the highest and lowest capacitance recorded for those with **2** and **5**, respectively. Given that the area of electrodes was consistent, any influence of the EDL or other electrochemical aspects can be potentially attributed to the supporting species used rather than cell geometry. Further evidence of supporting species influencing the zinc deposits is subsequently presented and discussed in section 4.4.3. Such a large range of values (each with a large relative error) indicate significant differences in the organization and behavior of ions forming the EDL, possibly with the densest packing of ions (and thus highest C_2) observed from the use of **2**. Conversely, a low C_2 in the presence of **5** suggests the formation of a comparatively less-compact EDL possibly due to larger ions forming it, notwithstanding any changes in zinc surface morphology. This provides an explanation towards the higher diffusion limitation in electrolytes

containing **5** although the reaction is occurring at a slower rate due to the high charge-transfer resistance. Further study is underway to understand this phenomenon. From comparison of the differential capacitances of the various electrolytes at 1 kHz, test results confirmed that solutions with **2** and **3** had higher differential capacitance than electrolytes with other supporting species while those utilizing **5** had the lowest differential capacitance. However, there was a slight discrepancy in the order of those using **1** and **4** which is attributed to the overlap of C_2 values within the margin of error and indicating that the ions present in these solutions potentially exhibit similar capacitive behavior.

4.4.3. SEM and XRD characterization of zinc electrodeposits

The zinc electrodeposits produced during the charging phase of the Zn/Br system under a current density of 20 mA cm^{-2} exhibit significantly different morphology depending on the supporting electrolyte used, and are presented in Figure 4-4. This observation confirms the significant influence of the anions studied herein on zinc electroplating behavior during battery operation, possibly *via* complexes formed with Zn^{2+} in solution. Electrolytes employing **2** and **4** produced bright electrodeposits with highly crystalline regions and crystal sizes generally between 5–10 µm, while solutions with **3** produced comparatively larger crystals in patches which were less bright. Conversely, solutions utilizing **1** and **5** produced highly mossy deposits with needle-like zinc clusters which were dull and had very little apparent ordering during visual observation. This observation suggests a link between high NOP seen during CV and the generation of mossy deposits due to the creation of multiple nucleation points instead of crystal growth. The mossy appearance of deposits in solutions with **1** was unexpected as such deposits are usually associated with poor electrochemical performance,[41,89] whereas the opposite was noted during CV tests in this study. Such

zinc electrodeposition behavior when utilizing a $ZnSO_4$ electrolyte has been previously reported[202] and it has been postulated the presence of an adsorbate (likely hydrogen) interferes with the normal epitaxial deposition, thereby promoting dendritic growth instead. This model offers a possible explanation of the reason behind the mossy deposits obtained from solutions containing **1**.
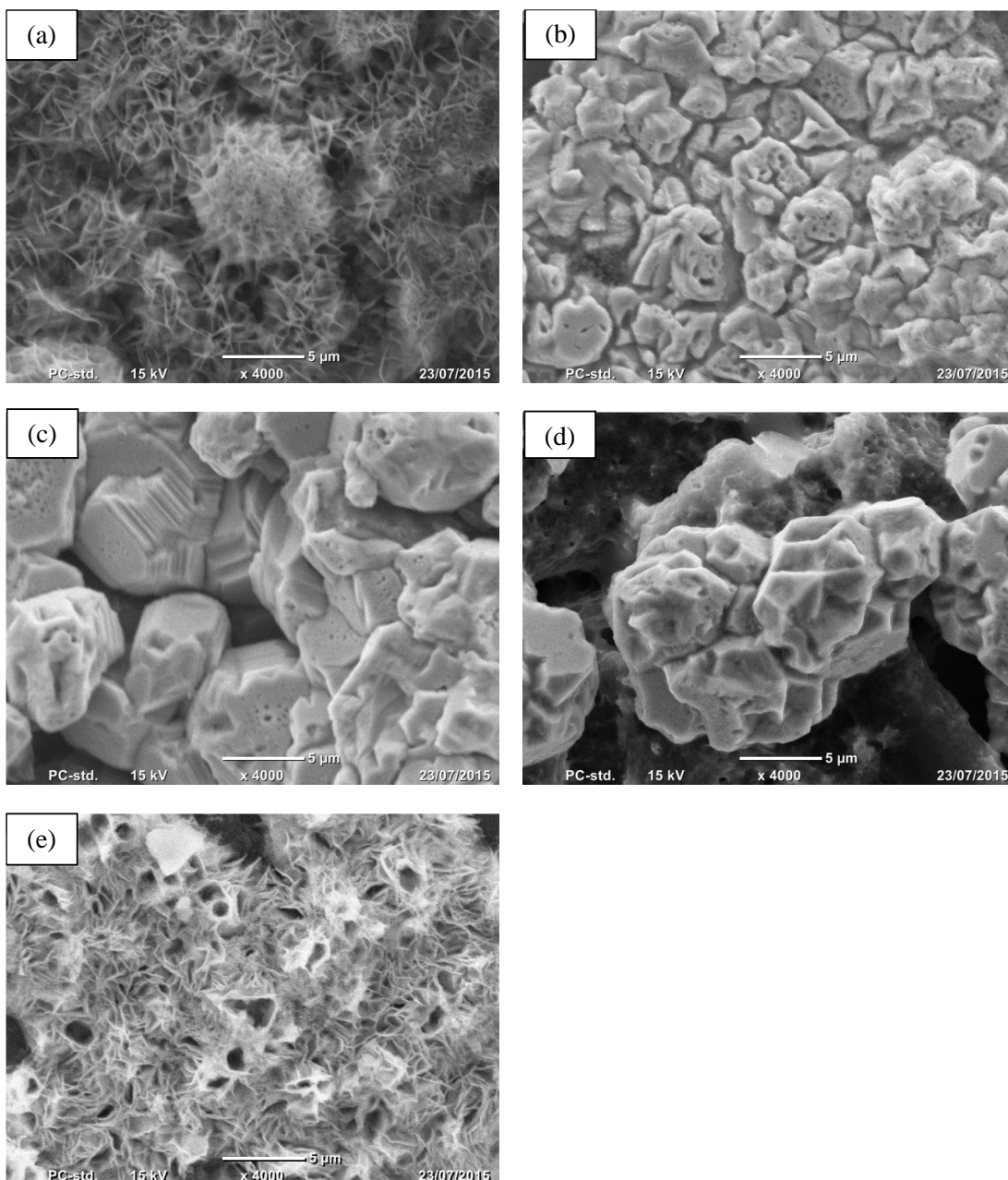
Figure 4-4. SEM micrographs of zinc electrodeposited on graphite after 10 minutes of charging at 20 mA cm^{-2} from solutions containing 0.5 M of the secondary electrolytes studied: (a) **1** Na_2SO_4, (b) **2** NaBr, (c) **3** NaCl, (d) **4** NaH_2PO_4 and (e) **5** $NaNO_3$.

Circular pores with diameters less than 5 µm were found within deposits obtained in the presence of **5**. These pores are possibly due to the evolution and escape of hydrogen bubbles on the electrode surface under the electrodeposited zinc. H_2 evolution caused by depassivation due to the presence of impurities has been discussed for the case of zinc electrodeposited from acidic sulfate solutions.[203] In the present work, it is proposed that depassivation at the zinc surface occurs in the presence of electrolytes containing nitrates (**5**), thereby promoting H_2 evolution on the electrode surface. The generation of H_2 could explain the significantly poorer electrochemical performance during the oxidation scan compared to the reduction scan observed during CV, as well as presence of double peaks on CV and Tafel plots, for that electrolyte. With the exception of solutions using **1**, those which produced non-mossy zinc deposits were observed to also give relatively good zinc half-cell CV values. A similar observation has been previously reported in the literature.[149] Experimental and molecular modelling work is being undertaken to better understand this phenomenon.

Diffractograms from XRD analysis of zinc electrodeposits obtained from the various electrolytes are presented Figure 4-5 and are consistent with SEM observations. The miller indices of zinc peaks were identified using PDF card #04-014-0230 in the PDF4+ database, and crystal orientations were compared upon standardized baseline correction using software. Solutions containing **2**, **3** and **4** yielded electrodeposits with a strong (101) preferred orientation and a secondary preference for the (102) configuration. A preference for the (101) orientation has been previously reported for the case of zinc deposited from solutions with 2.5 M $ZnBr_2$ and relatively high concentration of 3 M NaCl supporting electrolyte,[182] while some preference for the (102) and (103) configurations has also been reported from the use of $ZnCl_2$ solutions containing HCl.[90] The similarity in XRD peaks obtained for zinc electroplated from

these solutions is consistent with their generally similar morphology observed during SEM. The mossy deposits produced by electrolytes utilizing **1** and **5** exhibited a preference for the basal (004) orientation. XRD results in this and the previous chapter show that there can be significant variation in the preferred orientation of zinc electrodeposits. The difference in moving from the NaCl and $ZnCl_2$ solutions between this and that work is a likely cause of this difference, with the results suggesting the possibility that cations also have a role in influencing the preferred zinc deposit orientation.
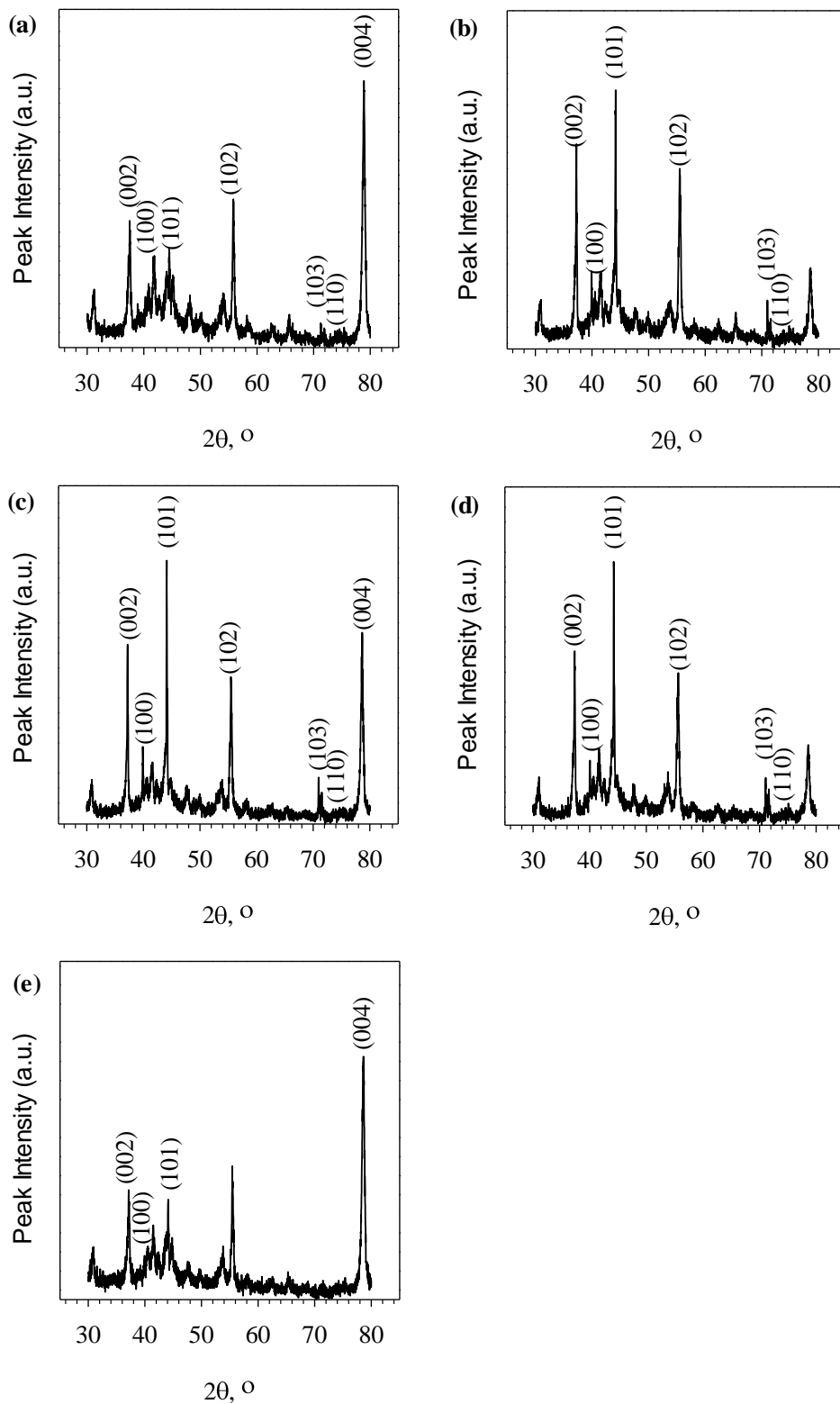
Figure 4-5. Raw diffractograms (with Miller indices of zinc peaks indicated after identification during post-processing) from XRD analysis of zinc electrodeposited on graphite (peaks not indicated) after 10 minutes of charging at 20 mA cm^{-2} from solutions containing 0.5 M of the secondary electrolytes studied: (a) **1** Na_2SO_4, (b) **2** NaBr, (c) **3** NaCl, (d) **4** NaH_2PO_4 and (e) **5** $NaNO_3$.

4.4.4. Selection of suitable alternative supporting electrolytes

Based on the findings from half-cell CV scans and Tafel analysis of the electrolytes studied, two alternatives to Cl-based supporting electrolytes are suggested. The first suggestion involves the use of higher bromide concentrations (by up to 0.5 M, based on this study). The second alternative is the further development of sulfates- and/or phosphate-based secondary electrolytes. The expected benefits of these two approaches are based on lower Zn^{2+}/Zn redox charge-transfer resistances and Zn^{2+} diffusion limitations, as indicated by impedance spectroscopy. Further investigations regarding the impact of these strategies on electrochemical performances of the bromine half-cell and subsequently a full Zn/Br cell are being undertaken.

It is proposed that the differences in electrochemical performance and behavior of ions in solution are attributable to the different types and degrees of zinc complexes formed in the presence of each supporting electrolyte. Specifically, the complexing of Zn^{2+} by weakly bound ligands of the various anions such as bromides and chlorides. It has been shown that increasing ion size increases the effective EDL thickness[190] and that ion size influences reaction rates at the electrode surface due to the extent of electrode-coverage.[151] Consequently, it is also possible that the formation of large cationic species in high concentrations does not allow for dense packing of ions at the EDL, thereby producing lower EIS capacitance values for some solutions studied in the present work. Consequently, the type and strength of ligands associated with zinc is an important factor to consider, with weaker association possibly giving rise to favorable zinc electrodeposition and thus zinc half-cell electrochemical performance. It is noted that differences between equilibrium potentials of different electrolytes are informative in terms of the electrolyte speciation (subsequently investigated in this

thesis), providing an indication of the 'unravelling' the zinc complex has to undergo before the reduction process can occur.

4.5. Chapter conclusions

Zinc half-cell electrochemical studies (CV, Tafel analysis, EIS) were performed to assess and identify possible alternative supporting electrolytes for Zn/Br flow batteries. Sodium-salts of the following anions were assessed for their viability by comparison against the conventional Cl-based option: Br^-, SO_4^{2-}, $H_2PO_4^-$ and NO_3^-. Electrolytes utilizing NaBr, Na_2SO_4 and NaH_2PO_4 generally exhibited comparable or better performance than those containing NaCl, primarily due to lowering of the charge-transfer resistance and diffusion limitation in the zinc half-cell. SEM imaging and XRD analysis confirmed the strong influence of supporting electrolyte type on the crystal size and morphology of zinc electrodeposits obtained during the charging phase of the battery. Electrolytes which produced smaller crystals also gave good electrochemical performance. Additionally and in contrast with conventional assumption, it was found that the generation of mossy deposits does not translate to poor zinc half-cell performance. The findings of this work are expected to prompt further investigations into, and identification of, beneficial alternative supporting electrolytes which improve Zn/Br performance.

The next chapter builds upon the findings and implications of this study by investigating the type and relative proportions of various complexes existing in conventional Zn/Br battery primary and secondary electrolytes, thereby providing an understanding of their influence on the behavior and performance of Zn/Br systems.

5. The Chemical Speciation of Zinc–Halogen Complexes in Zinc/Bromine Flow Battery Electrolytes

5.1. Chapter abstract

Zinc/bromine flow batteries are a promising solution for utility-scale electrical energy storage. The behavior of complex Zn–halogen species in the electrolyte during charge and discharge is currently not well-understood, and is an important aspect to be addressed in order to facilitate future electrolyte formulations. The speciation of the primary zinc bromide electrolyte with and without a secondary zinc chloride electrolyte is studied in the present work. Raman spectroscopy was carried out on aqueous solutions of zinc bromide at 5 concentrations (2–4 M) to account for the initial and later stages of charging, with 3 concentrations (1–2 M) of zinc chloride. Mixed solutions containing various combinations of each primary and secondary electrolyte concentrations were also studied. Semi-quantitative analysis of peaks after Gaussian and Lorentzian peak deconvolution showed that the proportion of four-ligand coordinated Zn–halides (i.e. $[ZnBr_4]^{2-}$ and $[ZnCl_4]^{2-}$) increases with higher salt concentration, as compared to complexes with lower halide coordination numbers. The presence of a previously unassigned peak was observed at the 220 cm^{-1} band in the Raman spectra of mixed electrolytes. *Ab-initio* molecular modeling suggests this peak is due to the presence of the hybrid-halide anionic complex $[ZnBr_2Cl(H_2O)]^-$. Increasing the Cl:Br ratio in electrolytes promote hybridization and subsequently decreasing the proportion of single-halide Zn–Br complexes. While this speciation study is focused on Zn/Br batteries, the findings are also potentially applicable to other energy storage and electrochemical systems containing zinc halide electrolytes.

5.2. Chapter introduction

The work presented in this chapter builds upon findings from studies on the influence of chlorides on electrodeposited zinc (Chapter 3) and the search for alternative supporting electrolytes (Chapter 4). The present chapter investigates the type and relative proportions of various complexes existing in conventional Zn/Br battery primary and secondary electrolytes, as part of efforts to understand the influence of speciation on Zn/Br system performance.

Evaluating alternative supporting electrolyte formulations[156] and ionic liquid bromine-sequestration agents[204] has shown such efforts to be crucial in improving half-cell performance, facilitating better power delivery, specific energy and eventual commercial viability. Such changes are due to the significant influence of electrolyte species on physical and electrochemical processes occurring within the bulk electrolyte and at the electrode–electrolyte interface during battery operation. However, a major challenge facing future development of this technology rests in obtaining a deeper and more comprehensive understanding of the various complexes, namely their proportion and behavior, existing within the electrolyte. This understanding is necessary as different zinc complexes can influence zinc electrodeposition and other processes which have direct bearing on battery behavior. Consequently, such knowledge is instrumental towards identifying and tailoring the design and development of more intelligent electrode and electrolyte materials as part of efforts to improve ZBB performance – a task which is undertaken in this study.

From surveying available literature pertaining to complex speciation in solutions containing similar salts to those found in modern Zn/Br electrolytes, there is general agreement regarding the type and physical configuration (e.g. tetrahedral) of zinc–halide species which exist. However, the calculated or empirically determined

concentrations of these complexes are largely inconsistent or not exhaustive in that they do not reflect the wider range of potential complexes which may exist in the electrolyte solution. Given the highly dynamic nature of RFB energy storage systems, it is of both research interest and commercial benefit to employ monitoring methods which are quicker and more efficient at providing snapshot analyses of electrolyte speciation within the battery environment. Consequently, Raman spectroscopy has been an approach used in the past as a means of semi-quantitatively estimating the presence and proportion of complexes present in solution.

Zinc–halogen complexes have long been studied,[205–207] and reported as having tetrahedral structures at salt concentrations below 10 M with structures similar to that of the crystal above that concentration.[208] They have also been investigated in other solvents including DMSO,[209] HMPA,[210] and alcohol solutions,[211] and generally found to coordinate with up to four ligands. While it is easier to detect weaker low-frequency Raman bands in the glassy state compared to the liquid phase,[212] this may not be directly applicable to the aqueous Zn/Br system.

Tetrahedral di-, tri- and tetra-bromo zinc complexes are common structures at standard conditions,[213,214] and become less stable as temperature increases.[215] It has also been shown that temperature has a greater influence than pressure on the proportion of zinc-halide species in aqueous solutions.[216] This difference in influence is to be expected as liquids are essentially incompressible fluids. Further to this, X-ray analyses[217,218] and Raman spectroscopy[219] have revealed that tetrahedral zinc-bromide structures are preferred at relatively high bromide concentrations. Neutron-diffraction studies have shown that the complex coordination number of the zinc cation is significantly influenced by the counter anion present in solution,[220] while cation size also influences the ion hydration configuration in solution.[221] A molecular dynamics study reports that

the type of dominating zinc-chloro complexes depend on chloride concentration whereas the $[Zn(H_2O)_6]^{2+}$ complex is always present in significant proportion.[222] Consequently, it can be expected that zinc complexes with a tetrahedral configuration are prevalent in conventional Zn/Br electrolytes. It is also to be noted that the composition of the complexes present also depends on the zinc to anion ratio.

It is noteworthy that relatively few studies report the investigation of solutions with the high salt concentrations similar to those used in conventional ZBB systems. To the best of our knowledge, the closest-related Raman studies of Zn/Br system electrolytes within the past two decades have been investigations on the separate phase which forms during charging when elemental bromine is sequestered using an ionic liquid additive,[223] and on aqueous primary electrolytes obtained at different states-of-charge.[224] However, conventional electrolyte formulations employed in current commercial ZBBs are yet to be studied in-depth, suggesting that the speciation and proportion of zinc-halide complexes (ZHCs) in the aqueous phase of the present Zn/Br battery electrochemical environment is still not fully understood.

These challenges can essentially be considered as a three-part sequential problem: (i) identifying the species present in solution, (ii) comparing their relative proportions, and (iii) determining their absolute concentrations within the electrolyte solution. The scope of the present work addresses gaps in knowledge of the former two aspects by employing a combination of Raman spectroscopy and first-principles density functional calculations to elucidate the identities and relative proportions of various ZHCs existing within aqueous ZBB electrolytes.

Molecular modeling has been a particularly good complement to such speciation studies, especially with recent computational advances, aiding in the proposal and confirmation of assignments for the various peaks present in the Raman spectra of

solutions containing ZHCs. Studies on hydration of the Zn^{2+} cation have reported the tetrahedral structure as being stable,[225] while coordination with monohydrates[226] and higher-order coordination[227,228] have also been studied. *Ab-initio* calculations have indicated that four- and six-ligand coordinated zinc complexes (including with water) are common in solutions containing bromides[229] as well as chlorides.[230] These configurations are generally consistent with earlier works in this area which reported that while hydrated zinc was stable when coordinated with six water molecules, the tetrahedral structure was most stable when chloride was a ligand.[231,232] Stability of the hexa-aquo species is due to that configuration being energetically favorable compared to others due to the particular arrangement and sizes of ligands as well as the equilibrium distances between them. Such findings are of interest in the present work as both bromides as well as chlorides can be present in conventional Zn/Br battery electrolytes.

Of interest and possibly highest relevance to the present work, the Raman vibrational modes and bands of zinc complexed with both bromide and chlorides in tetrahedral configurations have been computationally and experimentally investigated in a relatively recent study.[233] Halogens preferentially coordinating to zinc ions compared to water can be attributed to a higher zinc–halogen binding energy compared to that of zinc–water. It is to be noted that in that study, each ligand in the mixed complexes was a halogen (*viz.* no water molecules). Consequently, computational studies on tetrahedral zinc complexes containing both water and more than one type of halogen as ligands – such as this paper – are likely to be the first of their kind. This knowledge would be an important step in exploring and explaining speciation, electrochemical behavior and physical processes in Zn/Br RFBs, including the equilibria of electrolyte species in the presence of both the primary and supporting electrolytes.

Experimental evidence and identification of the various complexes present under different proportions of primary and supporting electrolytes in ZBBs is reported. This is followed by results from *ab-initio* calculations to propose possible assignments for peaks which were previously unreported in literature. This investigation provides insights into the existence of complexes which are possibly exclusive to Zn/Br systems due to their particular combination of primary and secondary electrolytes. These findings offer some explanation towards phenomena observed within the ZBB (particularly at the electrode–electrolyte interface). They are also an important linking step to exploring and comparing methods of calculating equilibrium constants and determining the proportions and concentrations of each of the various ZHCs previously identified as existing within the electrolyte solution.

This chapter is part of a larger study on electrolyte speciation, eventually linking physical characterization to electrochemical aspects in half- and full-cell systems. To the best of our knowledge, this work on determining the proportions and concentrations of each complex in Zn/Br RFB electrolytes, including species reported for the first time, gives the first detailed snapshot for the conventional system. It is expected that the findings presented in this study will influence alterations to Zn/Br electrolyte formulations and aid the design of complementary electrode materials to have beneficial impacts on system operation.

5.3. Methodology

5.3.1. Electrolyte preparation

Solutions of zinc bromide primary electrolyte and zinc chloride secondary electrolyte were prepared using commercially sourced $ZnBr_2$ (Merck, $\geq 98\%$) and $ZnCl_2$ (VWR, $\geq 98\%$) salts, respectively, in RO water. Single-electrolyte solutions of each salt were

prepared as follows: 2, 2.5, 3, 3.5 and 4 M zinc bromide with 1, 1.5 and 2 M zinc chloride to reflect concentrations typically used and studied in such systems.[41,45] 15 mixed electrolyte solutions were also prepared with different molar proportions of each zinc halide salt by combining the concentrations of the various single-electrolyte solutions tested, *viz.* five concentrations of zinc bromide solution each containing three different concentrations of zinc chloride. The pH and ionic conductivity of each solution studied in the present work was measured at 25ºC using CDC401 (for conductivity) and PHC101 (for pH) probes attached to an HQ440d laboratory meter (Hach, USA), with a minimum of five measurements for reproducibility.

5.3.2. Collection and analysis of Raman spectra

Raman spectra were collected using a Renishaw inVia Raman system with streamline CCD attached to a desktop computer running WiRE 4.2 software used for data collection and processing. A green laser (514 nm edge) with 10 s exposure time and 2400 mm^{-1} grating was used for all measurements in the 120–520 cm^{-1} region of interest, producing spectral resolution better than 2 cm^{-1}. Multiple-point baseline correction was applied to the obtained spectra, followed by deconvolution using a mixed Gaussian and Lorentzian function present in the GRAMS/AI software (version 9.2, Thermo Fisher Scientific, Inc.). The Raman vibrational band of each deconvoluted curve peak was used to identify the type of zinc complex present in solution, while the area under these curves was used to calculate and the ratios of areas used to determine the relative proportions of complexes present in each electrolyte solution, similar to approaches employed in earlier literature.[218,234]

5.3.3. *Ab-initio* vibrational calculations

Preliminary *ab-initio* calculations were carried out to confirm assignment of known vibrational bands and to identify any species producing Raman vibrations at previously

unreported bands for the zinc–halide solutions studied. The electronic energies were first obtained using periodic density functional theory (DFT) using the Vienna Ab-initio Simulation Program (VASP)[88] in the MedeA® software environment.[172] Projector-augmented wave (PAW) potentials[86,87] were used to describe the electron-ion interactions and the Kohn-Sham equations are solved *via* the generalized gradient-corrected Perdew-Burke-Ernzerhof method[173] using the GGA-rPBE functional. Isolated molecules were minimized in a vacuum cubic cell with length 10 Å using spin-polarized wavefunctions, 400 eV planewave cutoff and a Gaussian smearing of 0.001 eV at the Γ-point. A force constant approach was used for phonon calculations in the full Brillouin zone *via* the Phonon[235] software in MedeA®. Phonon calculations were carried out using similar VASP parameters to structural optimizations, with an interaction range of 10 Å and atom displacements of 0.06 Å for Raman tensor calculations.

5.4. Results and discussion

5.4.1. Analysis of primary and supporting electrolytes

The pH and conductivity of solutions containing zinc bromide or zinc chloride are summarized in Table 5-1, while their Raman spectra are shown in Figure 5-1, and the vibrational bands of assigned species are summarized in Table 5-2. The relative proportions of zinc complexes present in each solution, as determined from analysis of the Raman spectra, are presented in Table 5-3. A working assumption during peak analysis was that the Raman peak sensitivity is similar for the zinc complexes studied as they are relatively close in wavenumbers compared to the higher organics (e.g. ionic liquids) present in the electrolyte. The total area under all the peaks cannot be

completely associated to only zinc bromide due to the presence of other zinc species (in this case, zinc chloride) in solution for mixed solutions.

Table 5-1. Physical properties and numerical shorthand for various concentrations of separate primary and secondary electrolytes studied in this work.

Solution No.	ZnBr$_{2 \text{ (salt)}}$ (M)	ZnCl$_{2 \text{ (salt)}}$ (M)	pH	Conductivity (mS cm^{-1})
A1	2.00	–	3.60 ± 0.01	120.6 ± 0.2
A2	2.50	–	3.22 ± 0.01	122.6 ± 0.3
A3	3.00	–	2.91 ± 0.01	118.8 ± 0.5
A4	3.50	–	2.77 ± 0.04	115.8 ± 0.4
A5	4.00	–	2.36 ± 0.01	108.7 ± 0.5
B1	–	1.00	5.51 ± 0.01	83.9 ± 0.2
B2	–	1.50	5.34 ± 0.01	92.0 ± 0.1
B3	–	2.00	5.01 ± 0.01	99.6 ± 0.1
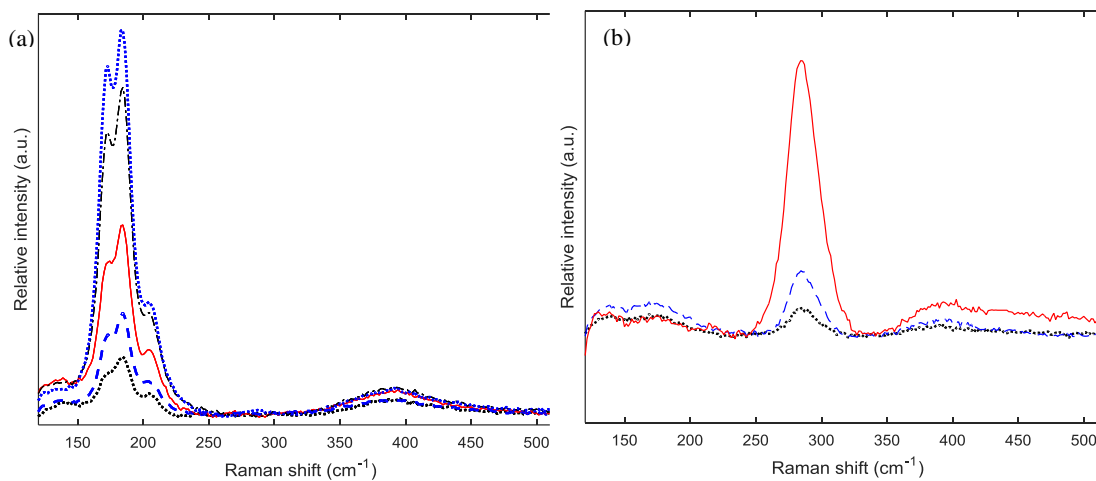
Figure 5-1. Raman spectra of (a) primary electrolytes containing 2 M (**A1**, dotted black line), 2.5 M (**A2**, dashed blue line), 3 M (**A3**, solid red line), 3.5 M (**A4**, dashed black line) and 4 M (**A5**, dotted blue line) zinc bromide, and (b) 1 M (**B1**, dotted black line), 1.5 M (**B2**, dashed blue line) and 2 M (**B3**, solid red line) zinc chloride.

Table 5-2. Experimental and calculated Raman vibrational band assignments of single-halide type zinc complexes present within the electrolytes studied in this work.

Complex species	Raman vibrational bands (cm^{-1})	
	Assignments in literature	Experimental and preliminary calculated assignments in this work
[ZnBr$_2$(H$_2$O)$_2$]$_{(aq)}$	206,[229] 204.0,[218] 207,[213,219]	Expt.: 205.9 ± 0.3 Calc.: 198
[ZnBr$_3$(H$_2$O)]$^-$	185,[229] 183.6,[218] 185,[213] 184[219]	Expt.: 184.7 ± 0.2 Calc.: 184
[ZnBr$_4$]$^{2-}$	174,[229] 170.6,[218] 171,[213] 172[219]	Expt.: 171.3 ± 0.3 Calc.: 163
[ZnCl$_2$(H$_2$O)$_2$]$_{(aq)}$	305[205]	Expt.: 297.6 ± 0.6 Calc.: 308
[ZnCl$_3$(H$_2$O)]$^-$	285,[205] 284[231]	Expt.: 284.2 ± 0.4
[ZnCl$_4$]$^{2-}$	275,[205] 275–280[206]	Expt.: 273.5 ± 0.7

Table 5-3. Relative proportions of zinc complexes present in solutions of 2–4 M zinc bromide primary and 1–2 M zinc chloride secondary electrolytes.

Solution No.	Relative proportion of complex species in electrolyte solution					
	$[ZnBr_4]^{2-}$	$[ZnBr_3(H_2O)]^-$	$[ZnBr_2(H_2O)_2]_{(aq)}$	$[ZnCl_4]^{2-}$	$[ZnCl_3(H_2O)]^-$	$[ZnCl_2(H_2O)_2]_{(aq)}$
A1 [a]	21%	60%	18%	–	–	–
A2 [a]	29%	53%	18%	–	–	–
A3 [a]	34%	50%	16%	–	–	–
A4 [a]	37%	48%	16%	–	–	–
A5 [a]	38%	48%	14%	–	–	–
B1 [b]	–	–	–	9%	66%	25%
B2 [b]	–	–	–	11%	57%	32%
B3 [b]	–	–	–	20%	49%	30%

[a] Standard deviation of ± 1% for zinc bromide solutions.

[b] Standard deviation of ± 2% for zinc chloride solutions.

Electrolyte pH decreases as the amount of zinc halide salt present is increased. While the conductivity of zinc chloride solutions increases with increasing salt addition, a peak observed at 2.5 M zinc bromide concentration suggests the presence of an optimally conductive concentration for that salt. It is observed that the amount of zinc bromide salt present has a larger impact on solution pH compared to changes in the amount of zinc chloride used, whereas the opposite is observed for the impact of salt concentration on electrolyte conductivity.

The Raman-active species observed are zinc coordinated with four ligands in a tetrahedral configuration. This observation is consistent with 4-coordinated zinc species reported in earlier literature discussed in section 5.2. Primary electrolyte solutions of zinc bromide salts produced Raman spectra with vibrational peaks corresponding to the following two-, three- and four-bromide coordinated zinc complexes: $[ZnBr_2(H_2O)_2]_{(aq)}$, $[ZnBr_3(H_2O)]^-$, and $[ZnBr_4]^{2-}$. $[ZnBr_3(H_2O)]^-$ and $[ZnBr_2(H_2O)_2]_{(aq)}$ exist in the highest and lowest proportions, respectively, for all solutions tested.

It is expected from Le Chatelier's principle that the relative concentration of each complex will vary with changing relative concentrations of chloride and bromide. As the amount of zinc bromide in the electrolyte increases, the proportion of $[ZnBr_3(H_2O)]^-$ complex decreases while that of $[ZnBr_4]^{2-}$ increases. Such behavior is to be expected, since the increase in amount of bromides in solution is likely to prompt ligand exchange in zinc-bromo complexes, substituting Br^- for H_2O. However, the proportion of $[ZnBr_2(H_2O)_2]_{(aq)}$ generally remains the same within the range tested. This consistency suggests that there exists some proportional saturation limit for the neutral species. With regards to the Zn/Br system, these results suggest that the longer the battery is charged and the higher the state-of-charge, there is increased substitution

of H_2O for Br^- in the existing zinc-bromo complexes, while maintaining a tetrahedral configuration in the resultant complexes.

Electrolytes containing only zinc chloride produced Raman spectra with vibrational peaks corresponding to the following three species: $[ZnCl_2(H_2O)_2]_{(aq)}$, $[ZnCl_3(H_2O)]^-$, and $[ZnCl_4]^{2-}$. The presence of two-, three-, and four-coordinated halogen species in these solutions is consistent with findings for electrolytes containing zinc bromide salts. Further to this, the $[ZnCl_3(H_2O)]^-$ exists in the highest proportion within the range of salt concentrations studied. With the exception of at the lowest concentration of 1 M zinc chloride, the proportion of $[ZnCl_4]^{2-}$ is higher than that of $[ZnCl_2(H_2O)_2]_{(aq)}$. Increasing the amount of zinc chloride salt present decreases the proportion of $[ZnCl_3(H_2O)]^-$ species whereas the proportion of $[ZnCl_4]^{2-}$ and $[ZnCl_2(H_2O)_2]_{(aq)}$ increases.

The increase in $[ZnCl_4]^{2-}$ proportion is to be expected as more chlorides are available in solution to substitute non-halide ligands in the zinc-chloro complexes (i.e. substituting H_2O for Cl^-) as was the case for zinc-bromo complexes in those solutions. However, the concurrent change in proportion of $[ZnCl_2(H_2O)_2]_{(aq)}$, unlike the unchanging proportion of $[ZnBr_2(H_2O)_2]_{(aq)}$ in zinc-bromo solutions, suggest that two- and four-coordinated zinc-chloro compounds are more stable than those with an odd number of halide ligands. There was no observable proportional saturation limit for the neutral species within the range of salt concentrations studied.

5.4.2. Analysis of mixed electrolytes

The pH and conductivity of solutions containing zinc bromide or zinc chloride are summarized in Table 5-4. The vibrational bands of assigned mixed-halide type zinc complexes are summarized in Table 5-5 (in addition to those already presented in

Table 5-2), while their Raman spectra are shown in Figure 5-2. The relative proportions of zinc complexes present in each solution are presented in Table 5-6.

Table 5-4. Physical properties and numerical shorthand for various concentrations of mixed primary and secondary electrolytes studied in this work.

Solution No.	ZnBr$_{2 \text{ (salt)}}$ (M)	ZnCl$_{2 \text{ (salt)}}$ (M)	pH	Conductivity (mS cm^{-1})
C1	2.00	1.00	4.07 ± 0.01	106.7 ± 0.3
C2	2.00	1.50	3.94 ± 0.09	101.3 ± 0.4
C3	2.00	2.00	3.77 ± 0.04	96.0 ± 0.1
C4	2.50	1.00	3.72 ± 0.04	93.1 ± 0.5
C5	2.50	1.50	3.30 ± 0.15	90.4 ± 0.1
C6	2.50	2.00	3.04 ± 0.04	90.4 ± 0.3
C7	3.00	1.00	3.38 ± 0.06	87.1 ± 0.2
C8	3.00	1.50	3.02 ± 0.04	85.4 ± 0.2
C9	3.00	2.00	2.78 ± 0.05	85.0 ± 0.1
C10	3.50	1.00	2.88 ± 0.02	76.5 ± 0.1
C11	3.50	1.50	2.59 ± 0.05	74.7 ± 0.1
C12	3.50	2.00	2.36 ± 0.01	74.0 ± 0.2
C13	4.00	1.00	2.53 ± 0.04	71.0 ± 0.3
C14	4.00	1.50	2.31 ± 0.08	69.0 ± 0.2
C15	4.00	2.00	2.15 ± 0.04	67.1 ± 0.6

Table 5-5. Experimental and calculated Raman vibrational band assignments of mixed-halide type zinc complexes present within the electrolytes studied in this work.

Complex species	Raman vibrational bands (cm^{-1})	
	Assignments in literature	Experimental and preliminary calculated assignments in this work
[ZnBr$_2$Cl(H$_2$O)]$^-$	Previously unreported	Expt.: 220.2 ± 0.8 Calc.: 224, 375
[ZnBrCl$_3$]$^{2-}$	200, 276[233]	Expt.: 196.6 ± 0.7, 277.8 ± 0.3 Calc.: 191
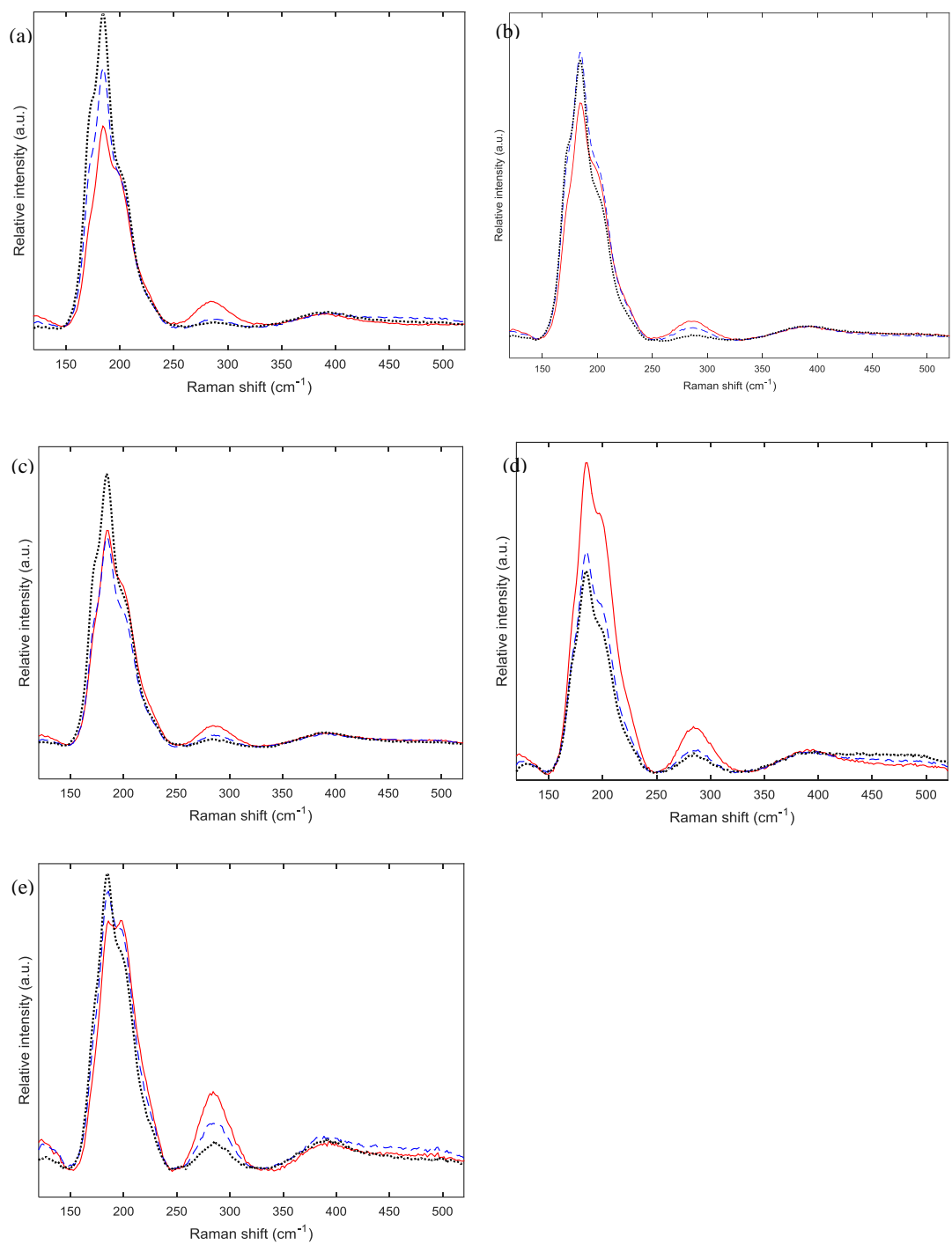
Figure 5-2. Raman spectra of (a) 2 M (**C1**–**C3**), (b) 2.5 M (**C4**–**C6**), (c) 3 M (**C7**–**C9**), (d) 3.5 M (**C10**–**C12**) and (e) 4 M (**C13**–**C15**) zinc bromide primary electrolyte containing 1 M (dotted black lines), 1.5 M (dashed blue lines) or 2 M (solid red lines) zinc chloride secondary electrolyte.

Table 5-6. Relative proportions (± 1% standard deviation) of zinc complexes present in mixed solutions of 2–4 M zinc bromide primary electrolyte with 1–2 M zinc chloride secondary electrolyte.

Solution	Proportion of complex species in electrolyte solution							
No.	$[ZnBr_4]^{2-}$	$[ZnBr_3(H_2O)]^-$	$[ZnBr_2(H_2O)_2]_{(aq)}$	$[ZnCl_4]^{2-}$	$[ZnCl_3(H_2O)]^-$	$[ZnCl_2(H_2O)_2]_{(aq)}$	$[ZnBrCl_3]^{2-}$	$[ZnBr_2Cl(H_2O)]^-$
C1	6%	10%	5%	16%	37%	16%	7%	3%
C2	4%	8%	4%	21%	30%	22%	7%	4%
C3	2%	5%	3%	25%	35%	20%	6%	4%
C4	6%	14%	7%	16%	38%	9%	7%	4%
C5	5%	11%	5%	21%	33%	15%	6%	4%
C6	3%	7%	4%	18%	40%	20%	6%	3%
C7	12%	16%	9%	12%	33%	6%	8%	4%
C8	8%	12%	4%	12%	41%	10%	9%	4%
C9	5%	8%	4%	26%	32%	15%	8%	3%
C10	14%	17%	7%	10%	36%	4%	9%	4%
C11	10%	17%	8%	16%	27%	10%	8%	4%
C12	7%	12%	8%	16%	35%	11%	7%	4%
C13	16%	23%	6%	8%	33%	1%	8%	5%
C14	10%	13%	6%	14%	37%	8%	8%	4%
C15	7%	10%	5%	16%	37%	11%	10%	4%

Both pH and conductivity decrease as the amount of salt added to the electrolyte increases. It is observed that the amount of $ZnBr_2$ salt present has a larger impact on solution conductivity and pH compared to changes in the amount of $ZnCl_2$ salt used.

A few trends are observed in the proportion of species existing as a function of changing the concentration of the electrolyte salts present in aqueous solution. Almost all the peaks present were identified from literature and single-salt solutions studied in this work. The type of species present in mixed solutions of primary and secondary electrolytes are generally consistent with those from single-salt solutions, namely: $[ZnBr_2(H_2O)_2]_{(aq)}$, $[ZnBr_3(H_2O)]^-$, $[ZnBr_4]^{2-}$, $[ZnCl_2(H_2O)_2]_{(aq)}$, $[ZnCl_3(H_2O)]^-$, and $[ZnCl_4]^{2-}$. Additionally, vibrational bands corresponding to the mixed-halogen complex $[ZnBrCl_3]^{2-}$ and an unknown species corresponding to vibrations at the 220 cm^{-1} band were observed.

An initial assignment of the $[ZnBr(H_2O)3]^+$ species to the new peak at 220 cm^{-1} was proposed as per an earlier study[219] which reported Raman vibration of this species at 240 cm^{-1}. However, this assignment was subsequently questioned due to the relatively large (20 cm^{-1}) discrepancy in peak locations which lay outside the good spectral resolution and consistency of other peak locations obtained in the present study. Consequently, preliminary *ab-initio* calculations carried out in the present work and comparing with possible species, both previously reported and unreported structures, suggest that the anionic complex $[ZnBr_2Cl(H_2O)]^-$ can be potentially assigned to Raman vibrations at the 220 cm^{-1} band. To the best of our knowledge, the present work is the first to investigate and report the vibrational band of this complex. The presence of mixed-halide complexes is to be expected as more than one kind of halide is present in the mixed electrolyte and competing with each other, as well as with H_2O molecules, for binding with zinc as ligands.

Overall, complexes of Zn and Cl are present in higher proportions than those of Zn and Br, possibly due to stronger ligand binding within the former pair. Interestingly, increasing Zn:Br ratios lead to a reduction in the proportion of Zn–Br species while the amount of Zn–Cl species increases. The opposite trend is observed upon increments to Zn:Cl and Br:Cl ratios. With regards to the Zn/Br system, these results suggest that as charging proceeds and the battery state-of-charge increases, the proportion of zinc bromide complexes decreases while that of zinc chloride species increases – a result which is to be expected. $[ZnCl_3(H_2O)]^-$ is the dominant species in all the solutions tested, while the newly assigned $[ZnBr_2Cl(H_2O)]^-$ ion is consistently present at the lowest concentration. This consistency suggests that the stability of dominant species is independent of pH and conductivity within the ranges of electrolyte salt amounts tested.

There is a strong link between the concentrations of $[ZnCl_2(H_2O)_2]_{(aq)}$ and $[ZnCl_4]^{2-}$, as well as between those for $[ZnBr_2(H_2O)_2]_{(aq)}$ and $[ZnBr_4]^{2-}$. Further to this, a notable inverse relationship in the concentrations of these pairs of species is observed, with higher concentrations of $[ZnCl_2(H_2O)_2]_{(aq)}$ and $[ZnCl_4]^{2-}$ leading to lower amounts of $[ZnBr_2(H_2O)_2]_{(aq)}$ and $[ZnBr_4]^{2-}$ present in solution. A strong linear relationship is observed between the concentration of each of the various species in solution as a function of Zn:Br molar ratio, though this correlation is limited to Zn salt concentrations below 4.5 M (*viz.* total halogen concentration below 9 M). Above these concentrations, no clear trend was observed in the proportion of electrolyte species.

5.4.3. Electrolyte speciation and Zn/Br battery behavior

The influence of various supporting electrolytes has previously been investigated[156] and presented in Chapter 4, where it was found that chlorides and bromides can exhibit

strong capacitive behavior at the zinc-side electrode in ZBBs. It is proposed that the presence of a higher proportion of zinc-chloro complexes compared to zinc-bromo species is linked to zinc half-cell electrochemical performance. Specifically, a higher proportion of zinc ions with chloride ligands results in additional energy required for dissociation, compared to zinc-bromide ligands, thereby producing the lower zinc half-cell current densities in solutions containing chlorides as observed.[156]

Further to this, electrochemical measurements carried out in that study led to the suggestion that the extent of complexation and cation sizes influence the structure and behavior of both the bulk electrolyte species and the electrical double-layer (EDL) at the electrode–electrolyte interface.[156]

In the present study, however, the only cationic zinc complexes formed are those due to zinc ion hydration, $[Zn(H_2O)_6]^{2+}$, associated with the peak at the ~390 cm^{-1} wavenumber region[223] of the Raman spectra obtained. This phenomenon suggests that the hydrated zinc cation and the anionic species identified in this study are the primary zinc-containing species forming EDLs at the zinc- and bromine-side electrodes in ZBBs, respectively. By extension, it is proposed that the presence and concentration of these anionic species (*viz.* $[ZnBr_4]^{2-}$, $[ZnCl_3(H_2O)]^-$, etc.) influences the diffuse or tightly-packed nature of the zinc-side EDL, leading to the variations in capacitive behavior.

Weak Raman signals in the 390 cm^{-1} region also pose a challenge in determining the relative proportion of zinc ions complexed with halides against those which exist "freely" (i.e. containing only H_2O ligands) in the aqueous solution. Consequently, it is necessary to carry out X-ray based investigations to determine the exact proportion, and hence concentration, of halide- and hydration-complexed zinc in each electrolyte mixture. It is expected that the results presented in this study provide an important and

useful foundation for subsequent speciation investigations into electrolytes containing ionic liquids for bromine-sequestration purposes (both with and without the presence of the separate sequestered phases) and other performance-improving additives at various sates-of-charge.

5.5. Chapter conclusions

Raman vibrational spectroscopy was carried out on solutions containing various salt concentrations of primary zinc bromide and/or secondary zinc chloride electrolytes, to improve understanding of the species present at various synthetic states-of-charge of Zn/Br batteries. The type and relative proportions of zinc-halide complexes present in solution were identified, with some similarities in the relative proportions of certain species observed, suggesting the presence of isosbestic points in the Raman data. Zinc ions were found to exist in tetrahedral complexes, and those in mixed electrolytes primarily exist with a single type of halide ligand.

Phonon calculations suggest that a previously unassigned band at 220 cm^{-1} found in this study could be assigned to the $[ZnBr_2Cl(H_2O)]^-$ complex. The higher proportion of zinc bound to chloride compared to bromide is linked to a decrease in zinc half-cell electrochemical performance in ZBBs as ligand dissociation is required prior to zinc electrodeposition during battery charging, and the binding of Zn–Cl is stronger than that of Zn–Br in zinc-halide complexes.

The findings of this work are expected to facilitate in-depth investigations into zinc complexation in the presence of other electrolyte additives, and optimization of electrolyte formulation to increase the proportion of species beneficial to Zn/Br electrochemical performance. It is also suggested that a titration approach might be helpful in further ascertaining the relative amounts of chloride and bromide.

The next chapter builds upon the findings and implications of this study by investigating potential alternatives to the conventional ionic liquid additives used in Zn/Br electrolytes by understanding their influences on the behavior and performance of zinc half-cells.

6. The Influence of Ionic Liquid Additives on Zinc Half-Cell Electrochemical Performance

6.1. Chapter abstract

Six ionic liquids were assessed for their fitness-for-utilization as alternative bromine-sequestering agents (BSAs) in zinc/bromine redox flow batteries (Zn/Br RFBs) *via* comparison against the conventional BSA, 1-ethyl-1-methylpyrrolidinium bromide ([C$_2$MPyrr]Br). These alternative BSAs included the bromide salts of the following cations: 1-ethyl-1-methylpiperidinium ([C$_2$MPip]$^+$), 1-ethyl-1-methylimidazolium ([C$_2$MIm]$^+$), 1-(2-hydroxyethyl)-3-methylimidazolium ([C$_2$OHMIm]$^+$), 1-ethylpyridinium ([C$_2$Py]$^+$) and 1-(2-hydroxyethyl)pyridinium ([C$_2$OHPy]$^+$). Cyclic and linear sweep voltammetry, as well as electrochemical impedance spectroscopy, were performed to understand the influence of electrolytes containing these ionic liquids on zinc half-cell electrochemical performance. Solutions with [C$_2$Py]Br, [C$_2$MIm]Br and [C$_2$OHPy]Br improved zinc half-cell performance (highest-magnitude current, charge, maximum power and energy) when compared to those utilizing [C$_2$MPyrr]Br. Electrolytes employing these BSAs also reduced the nucleation overpotential of zinc electrodeposition and stripping compared to those using [C$_2$MPyrr]Br. Zinc electrodeposits obtained during charging from electrolytes containing the different BSAs were analyzed *via* scanning electron microscopy and X-ray diffraction. Scanning electron micrographs showed a strong relationship between the chemical structure of the BSA employed and the crystallinity of zinc electrodeposits, with solutions containing [C$_2$OHMIm]Br, [C$_2$Py]Br and [C$_2$OHPy]Br producing more compact zinc deposits than those with other BSAs. These findings warrant further investigation of BSAs with delocalized cationic charge. While these

compounds have been proposed for application in Zn/Br systems, they are also potentially adaptable to other types of RFBs, which employ the Br_2/Br^- redox couple and use electrolytes containing BSAs.

6.2. Chapter introduction

The work presented in this chapter builds upon findings from the search for alternative supporting electrolytes presented in Chapter 4 by investigating the behavior and influence of ionic liquid additives as part of efforts to improve Zn/Br system performance. The evaluation of various organic bromide salts as potential BSAs has been a focus of earlier literature.[69,81,236,237] A recent study has also looked at the influence of the BSA on the bromide-side electrode as a result of the changing electrochemical environment within the Zn/Br system at different states-of-charge.[238] However, there appears to be little work reported to date investigating the possible effects of these organic agents on the zinc-side electrode of Zn/Br RFBs during electrodeposition (charging phase) and de-plating (discharge phase). The quality of electroplated zinc depends on many factors, including electrolyte composition.[191] For instance, the presence of surfactants in zinc plating baths facilitates smooth electroplating, resulting in a uniform and shiny deposit.[239] The surfactants used were anionic sodium dodecylsulfate, cationic dodecyltrimethylammonium bromide, and nonionic octylphenolpoly(ethyleneglycolether)10. They work by changing the Zn electrodeposition via inhibiting or allowing for instantaneous nucleation and three-dimensional growth controlled by diffusion. Consequently, the particular BSA employed could be considered an electrolyte additive which influences this electrodeposition process - a phenomenon which has been reported and reviewed in the literature.[158,240–242] Such a consideration is of high importance as the use and effects of organic additives in zinc electroplating has long been an established practice in

industry.[243,244] This has also been investigated for the Zn/Br system.[245] With relevance to the present work, it has been reported that increasing BSA concentrations in the electrolyte had the effect of reducing formation of zinc dendrites during charging.[45] It was found that deposits from QBr-containing (i.e. BSAs) electrolytes produced smoother deposits than those from solutions containing only zinc bromide. It is possible that the BSAs influence Zn electrodeposition by controlling the nucleation type and diffusion-related growth.

The present work is motivated by the need to develop alternative BSAs, which improve the electrochemical performance of both half-cells of the Zn/Br system. The focus here is on the zinc half-cell and significantly expands upon previous work presented in this area and accepted for publication in conference proceedings.[246] Five novel BSAs are tested and compared against the conventionally used BSA, [C$_2$MPyrr]Br, in a zinc half-cell to study the influence of the chemical structure of a BSA against the Zn/Zn(II) redox couple in this system. The methods, findings and implications of the present work are relevant to other RFBs, which employ the Br$_2$/Br$^-$ redox couple and make use of organic BSAs to sequester the bromine evolved. The mechanism, kinetics and extent of bromine complexation by these BSAs are also likely to significantly influence system behavior in the bromine half-cell as well as overall full-cell charge/discharge cycling performance. These investigations are left to a separate study. Aspects of this work are also adaptable for hybrid systems that rely on metal deposition from solution.

6.3. Methodology

6.3.1. BSA and electrolyte preparation

Zinc bromide (as ZnBr$_2$, Aldrich, >98%), zinc chloride (ZnCl$_2$, Ajax, >95%) and potassium chloride (KCl, Ajax, 99.8%) were sourced commercially. The sequestration

agents 1-ethyl-1-methylpyrrolidinium bromide ([C$_2$MPyrr]Br), 1-ethyl-1-methylpiperidinium bromide ([C$_2$MPip]Br), 1-ethyl-1-methylimidazolium bromide ([C$_2$MIm]Br), 1-(2-hydroxyethyl)-3-methylimidazolium bromide ([C$_2$OHMIm]Br), 1-ethylpyridinium bromide ([C$_2$Py]Br) and 1-(2-hydroxyethyl)-pyridinium bromide ([C$_2$OHPy]Br) were prepared by quaternisation of the required tertiary amine (Aldrich) by bromoethane (BDH), and purified by standard literature methods.[247] Typical BSA concentrations used in Zn/Br electrolytes are approximately 0.8–1 M[45,81] (based on the expected bromine content which is in turn influenced by the amount of zinc bromide and hence zinc ions present in solution), thus this concentration range was selected for testing. Stock solutions for each BSA tested in this study (50 mL of 2.5 M ZnBr$_2$ primary electrolyte) were prepared and supplied by colleague Max Easton (School of Chemistry, The University of Sydney).

6.3.2. Half-cell electrochemical measurements

A glass three-terminal electrochemical cell was used for half-cell studies. Graphite-coated conductive carbon plastic sheets made from high-density polyethylene (HDPE) blended with carbon nanotubes (RedFlow Ltd., Brisbane, Australia) with known exposed surface area of 0.3 cm^2 were used as working electrodes. Silver-silver chloride (Ag/AgCl/3.4 M KCl) was used as the reference electrode while the counter electrode was a polished vitreous carbon rod of 5 mm diameter. N$_2$ gas was bubbled through each testing solution for at least 20 minutes under magnetic stirring to remove dissolved oxygen prior to half-cell testing. N$_2$ was also introduced above the surface of the de-oxygenated solution to create and maintain an inert atmosphere to minimize oxygen re-dissolution into the electrolyte solution. The testing setup was placed in a custom-built Faraday shielding cage for the duration of all tests to minimize electrochemical interference during impedance measurements (the results of which are

sensitive to such effects). The range of testing temperatures was based on ambient laboratory conditions of $25 \pm 1°C$.

Electrochemical measurements were made using a Bio-Logic SP-300 potentiostat attached to a desktop computer running EC-Lab (version 10.32) data acquisition software, which controls the instrument and was also used to process and fit the results obtained. Cyclic voltammetry (CV) was run at 30 mV s^{-1} with a step size of 2 mV between 0 V and -1 V *vs* Ag/AgCl, with all scans stabilizing by the sixth cycle. Linear sweep voltammetry (LSV) was carried out at a slow scan rate of 2 mV s^{-1} from -0.95 V to -0.7 V *vs* Ag/AgCl. Good reproducibility of current densities is obtained using this setup, with values within ±2% (standard deviation of ±0.04 mA cm^{-2}) for CV measurements and ±1% (standard deviation of ±0.001 mA cm^{-2}) for LSV. The equations used for Tafel fitting on the linear regions of Tafel plots and determining the polarization resistance at the potential at which the exchange current density occurs are similar to those in Chapter 4 (Eqs. 4-1–4-2 and Eq. 4-3, respectively), with terms carrying the same meaning.

Electrochemical impedance spectroscopy (EIS) measurements began with polarizing the working electrode for 1 minute at -1 V *vs* Ag/AgCl to promote zinc deposition, followed by measurement of the open-circuit potential (OCP). Potentiostatic EIS scans were then carried out within a frequency range of 4 MHz to 50 mHz (10 points per decade) at OCP with a 10 mV ac perturbation. The differential capacitance arising from ion assembly at the electroplated zinc surface (forming an interfacial electrical double-layer, EDL) due to the negatively polarized working electrode was studied using impedance methods described in the literature.[201] Scanning was carried out at 20 frequencies between 0.1-200 kHz and potentials between -0.2 V and +0.2 V *vs* OCP (0.1 V steps) to identify a suitable frequency for comparing EDL capacitive behavior

of each solution studied. 1 kHz was selected as a suitable frequency as it allowed for clear comparison of trends in differential capacitance to be made (higher frequencies led to lower differential capacitance and distorted impedance measurements). Under the assumption that the working electrode is ideally polarizable, the differential capacitance was calculated using a similar equation[201] to Eq. 4-4 in Chapter 4, with terms carrying the same meaning.

6.3.3. Zinc deposit preparation and characterization

A Neware battery cycler was used to generate zinc deposits on graphite-coated electrodes (similar to those used in half-cell electrochemical tests) at a current density of 20 mA cm^{-2} for 4 minutes. The electrolyte solution was under constant magnetic stirring at 300 rpm to promote electrolyte homogeneity. The deposits were then stored under vacuum in a desiccator prior to analysis *via* scanning electron microscopy (SEM) and X-ray diffraction (XRD). Samples were quickly transferred to the SEM in air. SEM imaging was performed by colleague Max Easton with a Zeiss ULTRA+ operating at 5.0 kV. XRD scans were carried out in air using a Shimadzu S6000 employing a Cu-Kα target under conditions of 40 kV and 30 mA, between a range of 30-80°, at a scan speed of 5° min^{-1} and step size of 0.02°. The diffractograms obtained were analyzed using the PDF4+ software database to identify the preferred crystal orientations of zinc electrodeposited from each solution.

6.4. Results and discussion

6.4.1. Physical properties of electrolytes containing varying BSA compounds

The cation structures of the various bromide salts prepared for this work are shown in Figure 6-1, with mnemonic and numerical shorthand defined for ease of reference. The

cations were selected using the conventional BSA, [C$_2$MPyrr]Br (**1**), as a structural basis. Table 6-1 summarizes the physical properties measured (by colleague Max Easton) for the electrolyte solutions containing all components of the electrolyte.

1	**2**	**3**	**4**	**5**	**6**
[C$_2$MPyrr]$^+$	[C$_2$MPip]$^+$	[C$_2$MIm]$^+$	[C$_2$OHMIm]$^+$	[C$_2$Py]$^+$	[C$_2$OHPy]$^+$
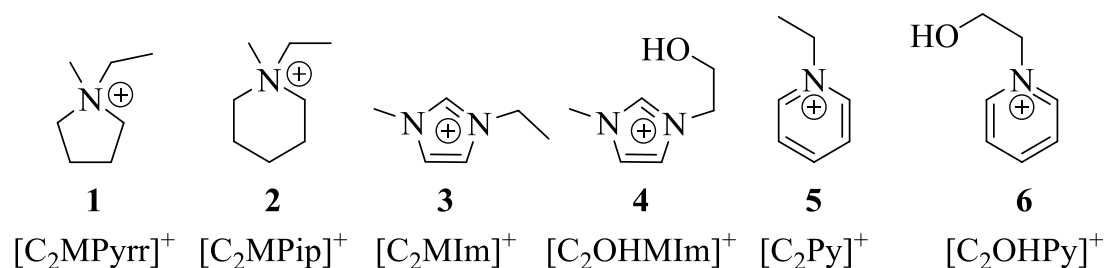
Figure 6-1. Cation structures of the BSAs studied in the present work.

Table 6-1. Physical properties for aqueous electrolytes containing 1 M BSAs at 21±2°C.

BSA	pH	Conductivity (mS cm^{-1})
[C$_2$MPyrr]Br (**1**)	3.72	92.3
[C$_2$MPip]Br (**2**)	3.64	84.1
[C$_2$MIm]Br (**3**)	3.75	97.4
[C$_2$OHMIm]Br (**4**)	3.30	96.0
[C$_2$Py]Br (**5**)	3.65	98.8
[C$_2$OHPy]Br (**6**)	3.41	96.7

Conductivities were comparable for solutions containing **3-6**, with values ranging from 96.0-98.8 mS cm^{-1}. Conductivity of the electrolyte employing **1** was slightly lower (92.3 mS cm^{-1}) while the value for solutions containing **2** was significantly less at 84.1 mS cm^{-1}. The presence of additional ionic species influences conductivity, seen when electrolyte conductivity was enhanced when BSA cations with a delocalized positive charge were employed, a property which has a possible influence over electrochemical performance, *vide infra*. Similar pH values (3.64-3.75) were measured for solutions utilizing **1**, **2**, **3** and **5**. However, a lower pH was obtained in the presence of BSAs with a hydroxyethyl group (**4** and **6**). This lower pH is attributed to the labile

and thus acidic hydrogen atom of the OH group. It is possible that a zwitterionic species forms when the hydroxylated species are used as the BSA.

The influence of these physical properties and other chemical influences induced by the structurally disparate BSA cations on the zinc half-cell electrochemical performance are investigated below.

6.4.2. Cyclic voltammetry and Tafel analysis for the zinc redox couple in solutions of ionic liquid bromide salts

Voltammograms from CV of the Zn/Zn^{2+} redox couple in solutions containing the various BSAs are presented in Figure 6-2.

Figure 6-2. Zinc-side cyclic voltammograms for electrolytes containing the six BSAs tested in the present study: **1** [C$_2$MPyrr]Br (thin solid red line), **2** [C$_2$MPip]Br (large dotted red line), **3** [C$_2$MIm]Br (thin dashed green line), **4** [C$_2$OHMIm]Br (small dotted green line), **5** [C$_2$Py]Br (thick solid blue line) and **6** [C$_2$OHPy]Br (thick dashed blue line).

The following electrochemical performance indicators and their efficiencies (*eff*) are calculated during forward (*i.e.* reduction, *red*) and reverse (*i.e.* oxidation, *ox*) scans and are presented in Table 6-2: highest-magnitude current (*j*), charge (*Q*), maximum power (*P**) and energy (*E**) density, and nucleation overpotential (NOP). Values for highest-magnitude current and maximum power are obtained directly from voltammograms while energy and charge densities are calculated by integrating the area under plots of current and power against time, respectively. The electrode potential ($j_{ox\text{-}E}$) at which the stripping peak was produced from each electrolyte was also recorded. Ag/AgCl is used as a reference for calculating *P** and *E**. NOP for zinc electrodeposition is calculated as the difference between the deposition (DP) and cross-over potentials (COP) observed in CV plots.

Table 6-2. CV of the zinc redox couple in the presence of six ionic liquid bromide salts.

BSA	1	2	3	4	5	6
j_{red}, mA cm^{-2}	-10.3	-8.8	-10.8	-10.2	-13.3	-10.9
j_{ox}, mA cm^{-2}	9.3	7.7	9.5	9.0	12.5	9.9
$j_{ox\text{-}E}$, mV	-618	-645	-615	-640	-524	-640
Q_{red}, mC cm^{-2}	-58.6	-47.5	-63.5	-56.9	-99.6	-62.1
Q_{ox}, mC cm^{-2}	53.8	43.3	57.7	52.4	89.5	55.2
Q_{eff}, %	91.9%	91.3%	90.9%	92.1%	89.9%	88.9%
P^*_{red}, mW cm^{-2}	10.3	8.8	10.8	10.2	13.3	10.9
P^*_{ox}, mW cm^{-2}	5.7	5.0	5.9	5.8	6.6	6.4
P^*_{eff}, %	56.0%	56.3%	54.5%	56.5%	49.3%	58.2%
E^*_{red}, mJ cm^{-2}	55.2	44.9	59.7	53.7	92.3	58.6
E^*_{ox}, mJ cm^{-2}	30.3	24.0	31.2	28.8	43.0	30.7
E^*_{eff}, %	54.9%	53.5%	52.3%	53.7%	46.5%	52.4%
DP, mV	-848	-865	-841	-856	-792	-851
COP, mV	-809	-815	-804	-815	-762	-815
NOP, mV	39	50	37	41	30	36

There is some significant variability in the onset potential for reduction in these cases with the BSA present, which can be due to different speciation with the BSA in solution. The highest magnitude of current densities obtained during zinc

electrodeposition and stripping were for solutions of BSA **5**, while those utilizing **2** gave the lowest values. This trend was generally observed for forward and reverse scan Q, P^* and E^* values. All the electrolytes tested gave relatively close Q_{eff} (maximum difference of 3%), while a broader range of values was obtained for P_{eff}^* and E_{eff}^* (7-9% maximum difference). P_{red} during the forward CV scan of each solution was calculated using the highest-magnitude current at a lower scan limit of -1 V *vs* Ag/AgCl reference, hence, each electrolyte produced P^*_{red} values of magnitude similar to their j_{red}. However, this behavior was not maintained during the reverse scan since the stripping j_{ox} occurred at j_{ox-E} other than -1 V. Half-cell results suggest a possible inverse relationship between the magnitude of E values obtained in the zinc half-cell and the E^*_{eff} of zinc-related processes. A clear relationship is observed between better zinc half-cell electrochemical performances and narrowing of the NOP. The best-performing electrolyte containing BSA **5** also produced the lowest NOP while the highest NOP was recorded for the worst-performing solution utilizing BSA **2**. On the basis of metrics including current densities and NOP, it is notable that better zinc half-cell CV performance was observed in almost every instance for solutions which employed BSAs possessing delocalized cationic charge (i.e. **3**, **5** and **6**), relative to the salts with localized charge (i.e. **1** and **2**).

The cell configuration used is expected to result in variations of zinc ion concentration in the electrolyte solution during CV measurements, *viz.* decreasing and increasing during the forward and reverse scans, respectively. This variation is in turn expected to have influence over the various impedances within the system determining half-cell performance, such as those associated with diffusion limitations at the electrode–electrolyte interface. This aspect is of interest in the present work, and consequently studied *via* EIS with the results presented and discussed in subsequent sections of this

work. The shifting of the formal potential for the case of the $[C_2Py]Br$ ionic liquid is indicative of a different mechanism involved compared to the other ionic liquid additives, suggesting that the possibility of different mechanisms at play explain why $[C_2Py]$ Br showed improved voltammetry performance.

Tafel plots for the zinc half-cell in the presence of each BSA are presented in Figure 6-3. Tafel analysis was performed for each electrolyte and a full set of Tafel fitting parameters including the exchange current density (i_0), polarization resistance (R_p), anodic (β_a) and cathodic (β_c) beta constants as well as the potential (E_0) at which i_0 occurs, is presented in Table 6-3. Tafel plots show that lower E_0 generally leads to higher i_0, although there appears to be some trade-off for the case of solutions with BSA **3** where i_0 decreased instead. Solutions producing lower R_p were generally also those which produced higher magnitude currents, charge, maximum power and energy densities observed during CV tests.
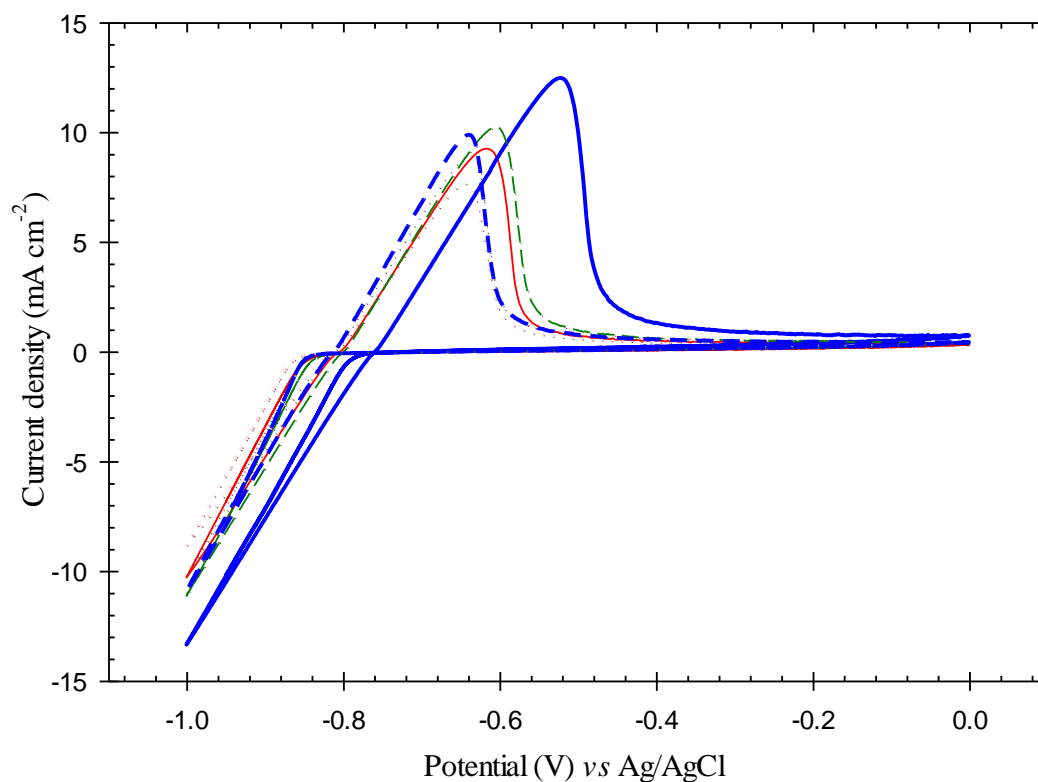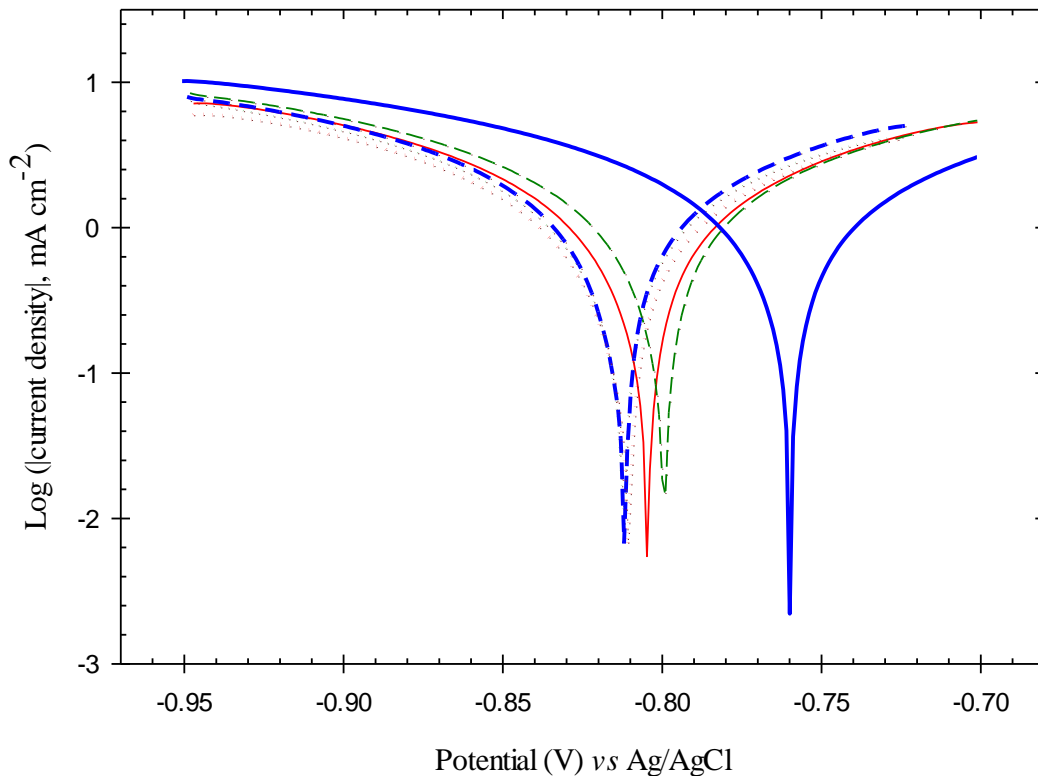
Figure 6-3. Zinc half-cell Tafel plots for electrolytes containing the six BSAs tested in the present study: **1** [C$_2$MPyrr]Br (thin solid red line), **2** [C$_2$MPip]Br (large dotted red line), **3** [C$_2$MIm]Br (thin dashed green line), **4** [C$_2$OHMIm]Br (small dotted green line), **5** [C$_2$Py]Br (thick solid blue line) and **6** [C$_2$OHPy]Br (thick dashed blue line).

Table 6-3. Tafel fitting parameters calculated for the zinc half-cell.

BSA	1	2	3	4	5	6
i_0, mA cm^{-2}	1.15	0.70	1.67	1.02	1.03	0.97
E_0, mV	-805	-811	-801	-812	-760	-812
β_a, mV dec^{-1}	132	97	173	114	108	100
β_c, mV dec^{-1}	138	107	179	120	112	111
R_p, Ω	79	101	73	74	71	68

6.4.3. Impedance spectroscopy

A Nyquist plot obtained by EIS for each electrolyte is presented in Figure 6-4. An equivalent circuit model (see inset of Figure 6-4) representing the various contributors to electrochemical impedance within the system was proposed and fitted using the Simplex method for each EIS result obtained. The proposed circuit is deemed appropriate due to the single-time-constant behavior observed in the impedance

spectra obtained. While the Nyquist plots show depressed semi-circles, the simplest equivalent circuit model with one time constant characteristic was utilized as a first-pass fitting before other more sophisticated equivalent circuit models were used even though adding more circuit elements would have allowed for a better fit but not directly attributable to a physical/electrochemical process.

The resistor circuit element R_1 represents solution resistance existing between the reference and working electrodes. R_2 represents charge-transfer resistance of the redox reaction while C_2 represents the capacitive contribution of the electrical double-layer arising due to ions at the electrode-electrolyte interface. Finally, the W_2 element represents Warburg diffusion limitations of ions. The values of each circuit element are presented in Table 6-4 for each of the electrolytes studied.
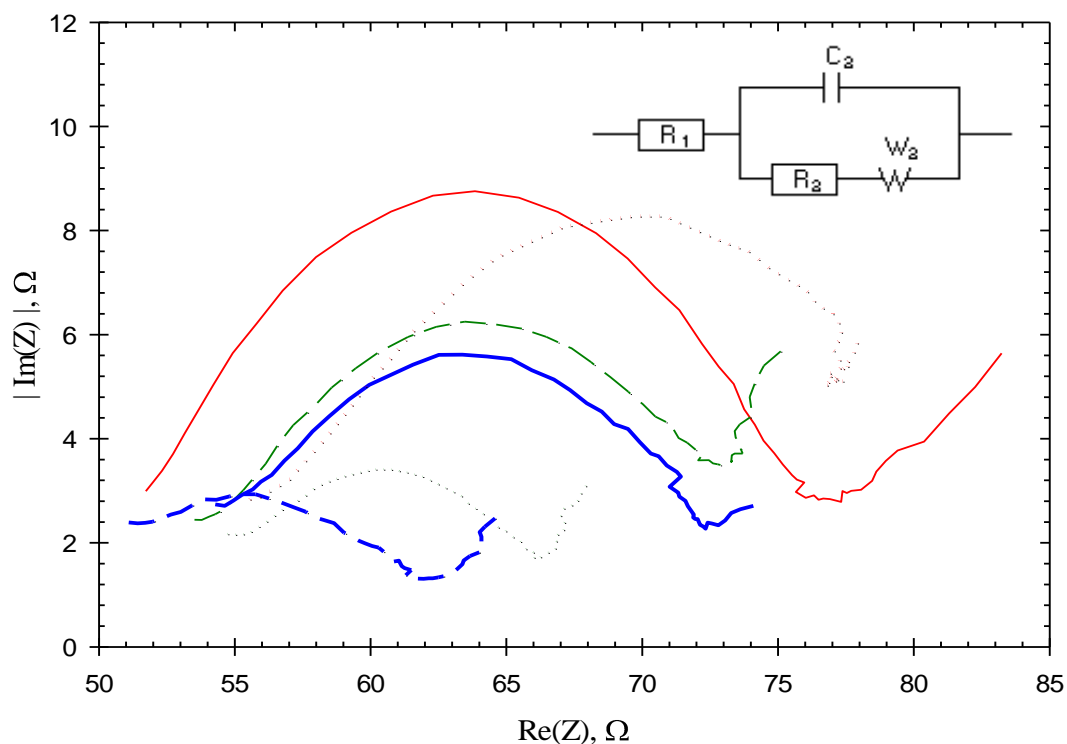
Figure 6-4. Zinc half-cell Nyquist curves for electrolytes containing the six BSAs tested in the present study: **1** [C$_2$MPyrr]Br (thin solid line), **2** [C$_2$MPip]Br (large dotted line), **3** [C$_2$MIm]Br (thin dashed line), **4** [C$_2$OHMIm]Br (small dotted line), **5** [C$_2$Py]Br (thick solid line) and **6** [C$_2$OHPy]Br (thick dashed line). Inset shows the equivalent circuit model used to simulate each curve.

Table 6-4. Equivalent circuit element values from simulation of impedance curves.

BSA	1	2	3	4	5	6
R_1, Ω	53.2 ± 0.3	57.6 ± 0.3	55.3 ± 0.3	56.3 ± 0.3	56.2 ± 0.3	52.9 ± 0.2
C_2, μF	36 ± 3	82 ± 9	92 ± 11	109 ± 24	83 ± 11	96 ± 23
R_2, Ω	21.1 ± 0.3	17.5 ± 0.4	15.1 ± 0.4	8.6 ± 0.3	13.9 ± 0.4	7.7 ± 0.2
W_2, $\Omega.s^{-0.5}$	4.5 ± 0.1	3.8 ± 0.2	3.9 ± 0.2	2.3 ± 0.1	2.6 ± 0.2	2.4 ± 0.1

Some links are observed between zinc half-cell electrochemical impedance behavior and the physical properties of electrolytes. Electrolyte solution resistances (R_1) are close (between 53-58 Ω), with those employing BSA **2** having the highest R_1. A higher R_1 suggests a lower mobility of ions within the electrolyte under the polarization conditions studied, which in turn could potentially be attributed to physical properties of the electrolyte such as a lower ionic conductivity. This suggestion is generally supported by the 9% lower ionic conductivity measured for electrolyte containing BSA **2** compared to electrolyte using **1** (see Table 6-1). The better-performing solutions containing BSAs **3**, **5** and **6** showed conductivities 5-7% higher than those with **1**, even though they also produced slightly higher R_1.

Significantly higher capacitance (C_2) values were obtained for electrolytes containing non-conventional BSAs (i.e. **2**-**6**). This increase in capacitance is attributed to denser packing of ions forming the EDL in those solutions. EIS results suggest that the BSA (which is usually considered a spectator in zinc half-cell electrochemistry) is actually interacting with the primary and/or supporting ions present in the electrolyte. It is also possible for the BSAs to be directly interacting with the surface of the negatively polarized zinc-side electrode (and later with the electrodeposited zinc as the charging phase progresses), thereby giving rise to an electrode-blocking phenomenon at some regions which causes additional zinc to deposit elsewhere.

Both EIS and differential capacitance tests confirm the existence of some adsorption on the surface of the zinc-covered working electrode, and the differential capacitances varied according to electrode potential *vs* OCP. Solutions containing **3** consistently produced the lowest differential capacitance at all scanning potentials, while those using **1** and **4** generally produced higher differential capacitance and electrolytes utilizing **2**, **5** and **6** gave mid-range values. Cation type significantly influences EDL behavior, with denser EDL leading to higher capacitance.[201] The size of ions (both cations and anions) has also been shown to influence differential capacitance, with larger ions leading to lower capacitance.[248] The variations in differential capacitance seen in this work are attributed to the potential-dependent adsorption of BSA cations on the electroplated zinc surface. The BSA orientation and degree of this adsorption influences the packing density of ions forming the EDL, consequently changing the capacitance. Molecular modelling studies are underway to study this behavior.

A trend is observed between charge-transfer resistances (R_2) and the structures of BSA present in solution. Electrolytes containing the two BSAs possessing hydroxyl functional groups (i.e. **4** and **6**) produced the lowest R_2 values of the BSAs studied. The use of non-hydroxyl versions of these BSAs resulted in a slight increase to these values (i.e. solutions with BSAs **3** and **5**), while electrolytes containing **1** and **2** produced the highest R_2. These observations suggest the strong dependence of zinc-side charge-transfer resistance on more than one factor, in this case pH, conductivity and other factors related to the chemical structure of the BSA that were unable to be measured directly. The relationship between the low pH and R_2 of electrolytes with BSAs **4** and **6** is less than obvious. Two possible explanations are proposed for these observations: (a) the presence of the OH group increases the dipole behavior of the BSA, which in turn limits interactions with the zinc surface (e.g. adsorption) due to

certain unfavorable molecular orientations (as described during EDL discussion, above) and thereby assists zinc electrodeposition by lowering the impedance to charge-transfer; (b) the labile hydrogen in the OH group results in more H^+ ions being available to preferentially form the EDL at the negatively polarized working electrode (compared to other cations in solution), and these H^+ ions are in turn displaced with relative ease when zinc ions undergo charge transfer and get electrodeposited.

EIS results also showed that the use of the non-conventional BSAs decreases resistance attributed to Warburg diffusion limitation (W_2) in the zinc half-cell. This observation further suggests that BSAs are interacting with ions in solution and strongly influencing ion behavior (including mobility).

6.4.4. SEM and XRD characterization of zinc electrodeposits

The morphology of zinc electrodeposits obtained by galvanostatic deposition at 20 mA cm^{-2} after 4 minutes of charging varies significantly, depending on the BSA present in the electrolyte. This is unsurprising as the presence of various organic electrolyte additives has been shown previously to significantly alter the preferential crystal orientation of deposited zinc.[249] SEM images of zinc deposits obtained from electrolytes containing the different BSAs are presented in Figure 6-5.
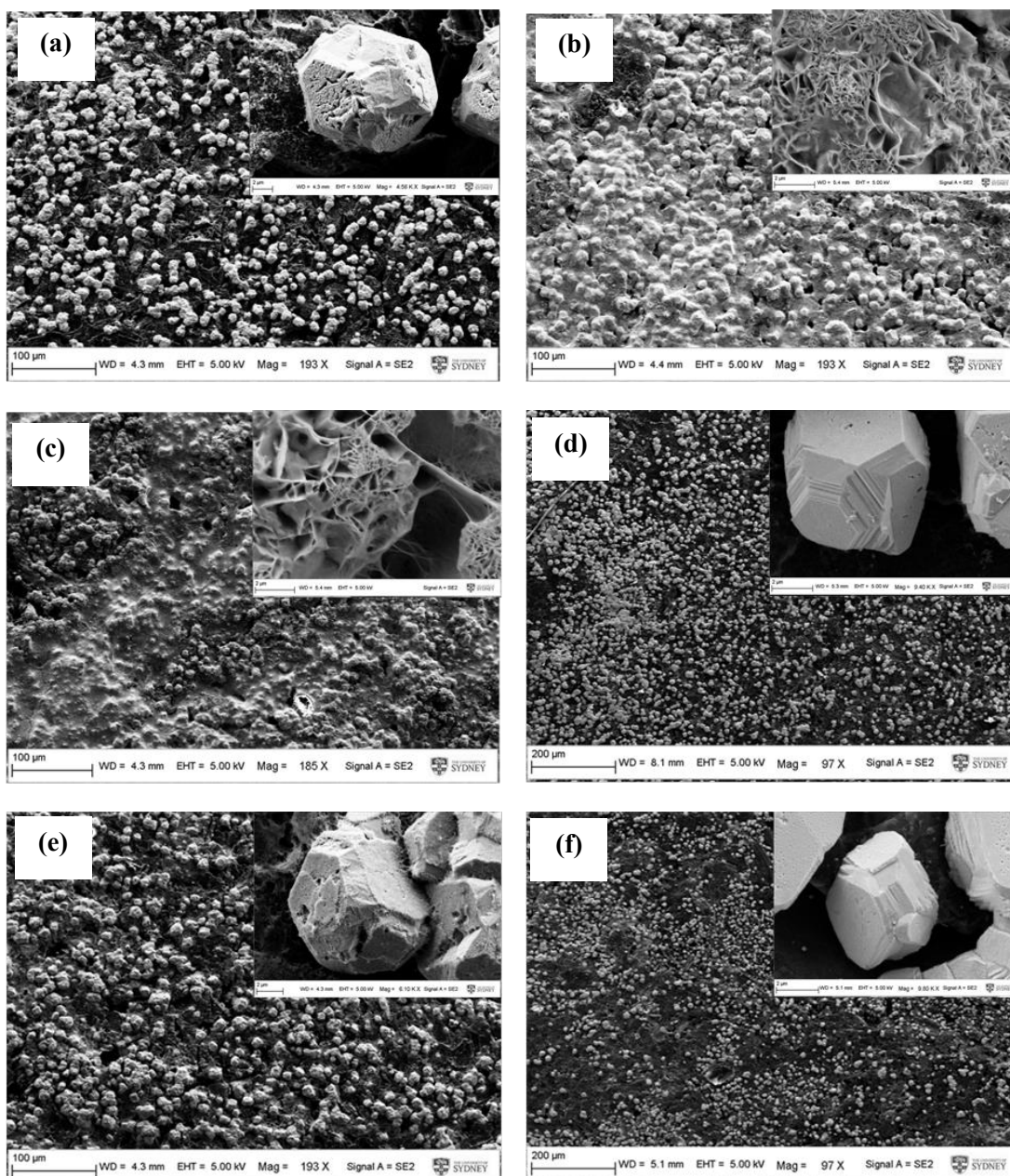
Figure 6-5. SEM images (100 (a, b, c, e) or 200 (d, f) µm scale for large images, 2 µm scale for insets) of zinc deposits obtained after 4 minutes of charging at 20 mA cm^{-2} current density from electrolytes containing the six BSAs tested: (a) **1** [C$_2$MPyrr]Br, (b) **2** [C$_2$MPip]Br, (c) **3** [C$_2$MIm]Br, (d) **4** [C$_2$OHMIm]Br, (e) **5** [C$_2$Py]Br and (f) **6** [C$_2$OHPy]Br.

Zinc electrodeposits obtained from electrolytes containing BSAs **4-6** exhibited highly crystalline regions with crystal sizes generally less than or equal to 10 µm. This production of highly crystalline zinc plating is a result of the relatively low diffusion limitations and charge-transfer resistances observed for solutions containing these BSAs. Conversely, solutions with the conventional BSA **1** produced slightly less

ordered, but still relatively small crystalline deposits that were slightly larger than 10 µm. Zinc deposits with micrographs exhibiting highly mossy morphologies and little apparent ordering are produced from solutions containing BSAs **2** and **3**. Compactness of zinc deposits has been linked to improved battery performance[149] and is supported by the findings in this work, wherein solutions giving highly-crystalline deposits were generally found to give good electrochemical performance during CV tests. The disparate structural features of the BSA cations studied potentially influence the formation and maintenance of complexed species with zinc in solution, leading to differences in orientations of crystals obtained, *vide infra*. Further experimental and molecular simulation work is currently in progress to understand this behavior.

The preferred crystal orientations of zinc electrodeposits was analyzed *via* XRD and found to vary depending on the BSA present in the electrolyte solution. Reflections, found by examination of blank samples to be associated with the clean/bare graphite electrode substrate and conductive silver-based glue from the preparation stage, were removed prior to identifying the preferred orientations of zinc crystal obtained using PDF card #04-014-0230 in the PDF4+ database and confirming with results of previous studies involving zinc electroplated from $ZnBr_2$ solutions.[90,182] Raw diffractograms for each zinc deposit obtained from electrolytes containing the different BSAs are presented in Figure 6-6, with Miller indices of zinc peaks indicated after identification during processing. Electrolyte with BSA **1** yielded an electrodeposit with a (101) preferred orientation and to a lesser extent the (102) orientation. Zinc electrodeposited from solutions containing BSAs **2**-**6** generally shows a strong preference for basal orientations. Most alternative electrolytes produced zinc preferring the (004) configuration, with the exception of samples derived from solutions with **6** that produced crystals preferring the (002) orientation.
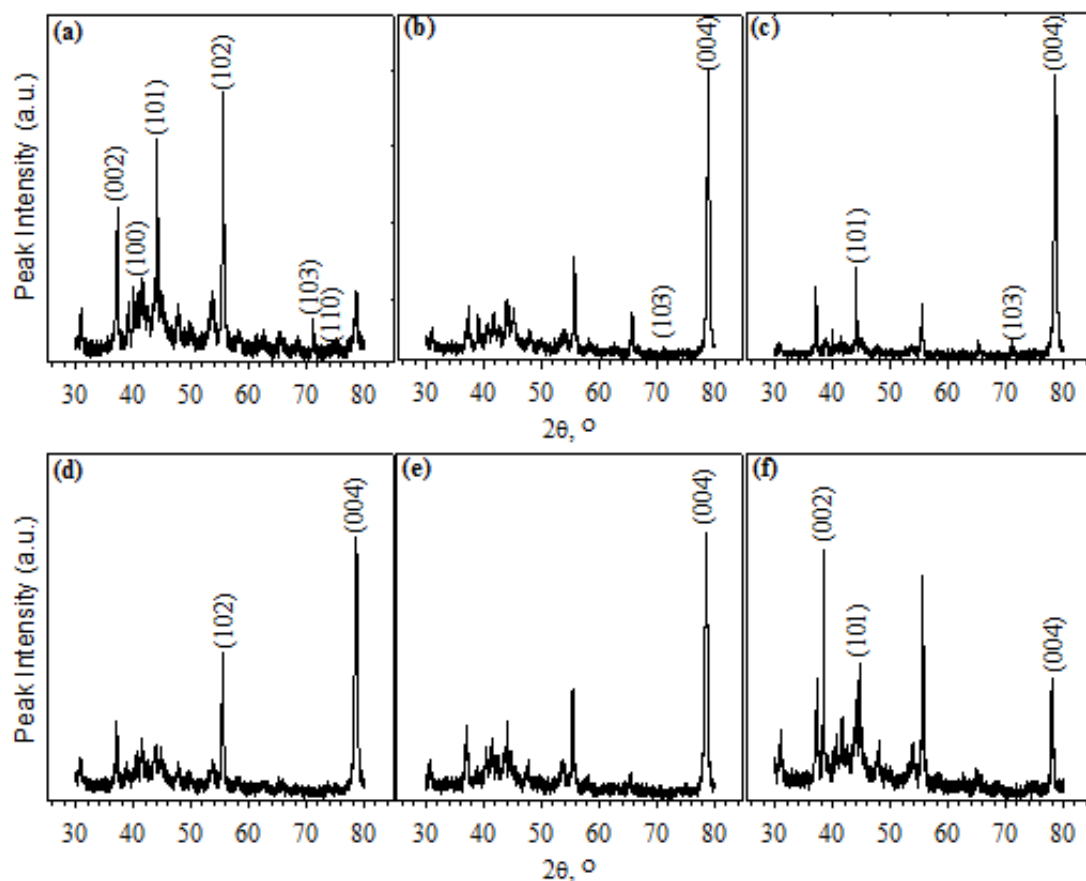
Figure 6-6. Diffractograms (with Miller indices of zinc peaks indicated) from XRD analysis of zinc deposits obtained after 4 minutes of charging at 20 mA cm^{-2} current density from electrolytes containing the six BSAs tested: (a) **1** [C$_2$MPyrr]Br, (b) **2** [C$_2$MPip]Br, (c) **3** [C$_2$MIm]Br, (d) **4** [C$_2$OHMIm]Br, (e) **5** [C$_2$Py]Br and (f) **6** [C$_2$OHPy]Br.

Electrochemical performance from half-cell tests of electrodepositing media can be linked to crystal orientation, with higher current densities obtained from electrolytes which produced zinc deposits with strong preferences for basal orientations at initial stages of charging (in this case 4 minutes into the charging process). Furthermore, an increasing preference for non-basal orientations directly relates to a decrease in zinc half-cell performance. This relationship is confirmed by the best-performing electrolytes containing **3**, **5** and **6**, all of which produce zinc deposits with preferences for (002) or (004) orientations. The presence of additional (103) or (102) planes in zinc electrodeposits from solutions containing **2** and **4** correlates with unfavorable electrochemical performance. It is possible that the presence of the (101) orientation

120

in zinc electrodeposits could be linked to electrolytes which give better electrochemical performance. It has been shown that differential capacitance (as a function of electrode potential) is influenced by electrode surface structure.[250] Given that the type of BSA used changes the morphology of zinc deposits obtained in the present work, variation in surface topography is the likely cause of different EDL structures and packing densities (and thus capacitive behavior) observed during EIS and differential capacitance tests for the different BSAs studied.

6.4.5. The influence of BSAs on zinc electrodeposition and stripping processes

On the basis of half-cell CV and Tafel analyses, electrolytes containing [C$_2$MIm]Br and [C$_2$OHPy]Br showed better electrochemical performance compared to those using the conventional BSA, [C$_2$MPyrr]Br, while solutions utilizing [C$_2$Py]Br gave the best performance.

The alteration of the chemical structure of the BSA employed in the zinc half-cell has demonstrated a clear influence over both voltammetry performance and the quality of zinc electrodeposits obtained during the charging phase. This may be due to a number of factors. As expected, the conductivity of the solution is a strong driver of the electrochemical performance (see in particular EIS analysis), however this does not account for all observed behavior. It is proposed that zinc ions in solution are complexed to various extents (and by varying modes of interaction) by alteration of the BSA's chemical character, however this too is not straightforward. Zinc ions in aqueous solutions will be complexed by weakly associated ligands of water molecules (i.e., Zn(H$_2$O)$_y^{2+}$), or bromide ions from the zinc bromide salt and/or BSA (i.e., Zn(Br)$_x^{(x-2)-}$). The existence of such bromo-zincates are well-known in the literature.[209,219,251] In this example, favorable zinc electrodeposition is likely to occur

for zinc coordinating water ligands preferentially due to the cationic complex arriving at the negatively polarized electrode, rather than the slight repulsion for the negatively charged bromide ligands. Thus, an important factor to consider is the strength of interaction between the BSA cation and its bromide counter-ion, whereby a weakly associated ion pair is more likely to provide a higher concentration of bromide ligands to complex zinc ions in solution.

In the case of the reduction currents experienced during electrodeposition, the negatively polarized electrode will assemble cationic species at its surface in the EDL. As the chemical structure of the BSA cation is varied substantially, the assembly of the EDL will vary in turn between each BSA electrolyte (as seen during EIS and differential capacitance tests). Consequently, the selection of BSA has significant influence over the behavior of zinc being electrodeposited on the electrode surface during the charging phase. In addition to the factors identified in the present study, other parameters likely also influence zinc half-cell performance. It is illuminating that those BSAs possessing delocalized cationic charges result in improved zinc half-cell performance by almost all the performance metrics applied in this study. Although further investigations are required to understand in more detail the chemistry underlying these observations, it is proposed that the electrolytes containing, for example, $[C_2Py]Br$, assemble more weakly at the EDL and complex their bromide anions more strongly than do BSAs such as $[C_2MPip]Br$. Weaker interactions amongst BSAs as well as with other electrolyte species would in turn influence ion mobility and thus the solution conductivities which appear to be linked to charge-transfer resistances.

6.5. Chapter conclusions

Electrochemical studies were carried out on the zinc half-cell of a Zn/Br flow battery to study the performance of electrolytes containing six different BSAs: [C$_2$MIm]Br, [C$_2$OHMIm]Br, [C$_2$Py]Br, [C$_2$OHPy]Br, [C$_2$MPip]Br and the conventionally-employed [C$_2$MPyrr]Br. Solutions with [C$_2$MIm]Br, [C$_2$Py]Br and [C$_2$OHPy]Br showed relatively good performance during CV tests and are recommended for further investigation as potential alternatives for future Zn/Br development. The best-performing electrolyte containing [C$_2$Py]Br had lower polarization resistance and produced higher exchange currents than solutions with other BSAs due to a lower diffusion limitation and less charge-transfer resistance (as seen during EIS). SEM imaging and XRD analysis of zinc electrodeposits obtained from each electrolyte clearly showed the significant influence of BSAs on zinc deposition morphologies during the initial stages of charging. The type of BSA employed influences the size and preferred orientation of zinc crystals obtained, with smaller crystals and basal orientations linked to better electrochemical performance. The findings of this work demonstrate the strong influence of BSA choice on zinc half-cell performance and behavior, contrary to the conventional simplifying assumption that BSAs are only spectators in this chemistry. It is expected that these findings will lead to rationally improved electrolyte formulations that also address the zinc electrodeposition process in Zn/Br flow batteries.

The next chapter builds upon the findings and implications of ionic liquids studied in this chapter by investigating the influences of utilizing binary BSA mixtures on half-cell performance and behavior.

7. Half-Cell Electrochemical Performance of Hybridized Ionic Liquid Additives

7.1. Chapter abstract

The effects of employing hybrid ionic liquid (IL) mixtures as bromine sequestration agents in zinc/bromine (Zn/Br) flow batteries are investigated. The ILs 1-ethyl-3-methylimidazolium bromide ([C2MIm]Br) and 1-ethyl-1-methylpyrrolidinium bromide ([C2MPyrr]Br) are studied within Zn/Br electrolytes in different mixing proportions at glassy carbon electrodes. Cyclic voltammetry showed beneficial performance in the Zn and Br half-cells when utilizing pure [C2MIm]Br and [C2MPyrr]Br, respectively. Consequently, it is recommended that electrolytes containing single IL types are better suited for Zn/Br systems compared to those utilizing hybrid mixtures. Electrochemical impedance spectroscopy showed that low diffusion limitations and charge-transfer resistance in both half-cells, as well as low Zn-side polarization resistance, contribute towards beneficial voltammetry performance. Scanning electron microscopy, X-ray diffraction and Williamson–Hall analysis of zinc electrodeposited during battery charging showed that the type and proportion of IL present influences crystal morphology and size. These findings warrant further investigation into full-cell testing, as well fundamental studies on the behavior and influence of other hybrid IL formulations for Zn/Br system applications. The methods and findings presented in this work are also applicable to electrodeposition and redox flow batteries which utilize pure or hybrid ILs for bromine sequestration purposes.

7.2. Chapter introduction

The search for alternative BSAs in Chapter 6 exploring IL cations with similar and differing structures to the conventional option has resulted in the identification of some promising compounds. That chapter presented results from tests utilizing graphite electrodes and a single BSA type per electrolyte studied. The effects of mixing the complexing agents N-ethyl-N-methyl-pyrrolidinium bromide and N-ethyl-N-methyl-morpholinium bromide have recently been studied in V/Br systems and found to improve cell performance.[111] However, to our knowledge, there has been little work investigating BSAs mixtures for Zn/Br electrolyte applications. It is possible that there exists some benefit from utilizing hybrid mixtures since different compounds benefit each half-cell to different extents. These possibilities motivate the fundamental half-cell electrochemical studies and physical characterization presented in this work. They provide a platform for optimizing the performance of each half-cell in the Zn/Br system, both at the electrode–electrolyte interface as well as within the bulk electrolyte, as well as support full-cell studies which are potentially more time-consuming (e.g. deep-cycling) and expensive.

Pure and hybridized BSA mixtures of the following ionic liquids are studied in the ZnBr$_2$ electrolyte to understand the influence of such solutions on the primary charge-transfer redox couples: 1-ethyl-1-methylimidazolium bromide and the conventionally employed 1-ethyl-1-methylpyrrolidinium bromide. The former IL has shown to produce modest improvements to zinc half-cell charge and current densities and efficiencies due to lower charge-transfer resistance at that electrode as compared to the conventional latter IL. Consequently, it is of interest to identify and study any synergistic effects which exist between these ILs and could potentially lead to improved system performance compared to electrolytes which employ a single IL type.

The mixing of these ILs in different proportions would also allow for a graduated assessment of how the various contributors of electrochemical performance (charge-transfer resistances, etc.) are influenced by the presence of different proportions of structurally disparate ILs existing within a single electrolyte.

Further to this, the present study investigates the electrochemical kinetics and performance, as well as physical characteristics, of zinc-side half-cell behavior in the presence of glassy carbon electrodes, whereas previous investigations were carried out using graphite electrodes. This difference provides an additional platform for comparing half-cell electrochemical kinetics and performance dependent on electrode substrate. In addition, electrochemical performance of the bromine half-cell is investigated in this study, in order to understand the influence of single-type and mixed BSAs in that half-cell. While the methods and findings of the present work are focused on Zn/Br RFB applications, they are also potentially applicable to other systems utilizing similar redox couples and electrodeposition reactions.

7.3. Methodology

7.3.1. Preparation of electrolyte solutions

Zinc bromide salt ($ZnBr_2$, Merck, >98%) was dried in a vacuum oven at 50°C prior to preparation of electrolytes. 2.5 M $ZnBr_2$ primary electrolyte solutions were prepared in RO water, and 0.8 M of BSA added according to the 0.8–1 M range typically used in such systems.[45,81] The ILs 1-ethyl-1-methylpyrrolidinium bromide ([C_2MPyrr]Br, >99%) and 1-ethyl-1-methylimidazolium bromide ([C_2MIm]Br, >99%) were sourced commercially from IoLiTec (Ionic Liquids Technologies GmbH, Germany). These ILs were mixed in different molar proportions (1:0, 3:1, 1:1, 1:3 and 0:1, respectively) to form the 5 electrolyte solutions studied in the present work.

7.3.2. Electrochemical tests

Electrochemical half-cell studies were carried out in a 3-terminal glass cell using a commercial glassy carbon working electrode (BASi MF-2012, 3 mm diameter), silver–silver chloride (Ag/AgCl/3.4 M KCl) as a reference and a glassy carbon rod as the counter electrode. Dissolved oxygen was removed from, and an inert atmosphere maintained over, all electrolyte solutions by bubbling N_2 through them before carrying out electrochemical tests. Cyclic voltammetry (CV), linear sweep voltammetry (LSV, for Tafel analysis and determining polarization resistance), potentiostatic electrochemical impedance spectroscopy (EIS) and differential capacitance[201,248] (DC) tests were carried out using a Bio-Logic SP-300 potentiostat according to methods, and using parameters, described in Chapters 4 and 6. Similar equations and techniques (including scanning parameters and bounds) to that study were used to carry out Tafel fitting on the linear regions of Tafel plots and calculations of DC in the present work. The EC-Lab (version 10.32) software was used for data acquisition, as well as extracting, processing and fitting the obtained results.

CV was carried out between 0 and –1 V vs Ag/AgCl at a scanning rate of 30 mV s^{-1} and step size of 2 mV to study the Zn half-cell, while the Br half-cell was studied between 0 and +1 V vs Ag/AgCl at a similar scan rate. LSV was carried out at 2 mV s^{-1} between –0.82 and –0.94 V vs Ag/AgCl. iR compensation was applied to minimize the effects of solution resistance. All scans had stabilized by the sixth cycle. Tests carried out in triplicate confirmed good reproducibility of half-cell current densities via this setup, within ±0.2 and ±0.4 mA cm^{-2} standard deviation for forward and reverse Zn-side CV scans, respectively, and ±0.1 mA cm^{-2} for LSV. Br half-cell CV values had standard deviation of ±0.1 and ±0.01 mA cm^{-2} during the oxidation and reduction scans, respectively. EIS scans of the Zn and Br half-cells at open-circuit

potential (OCP) also produced values with good reproducibility (within 5% and 0.1%, respectively). Impedance measurements at various frequencies between 0.1–5 kHz showed that higher frequencies led to lower DC due to distorted impedance measurements and/or did not allow for clear comparison of values and any trends. Consequently, 1 kHz was selected as a suitable frequency to calculate and compare the DCs of each solution which occurs due to ions assembling at the working electrode surface (electroplated zinc for Zn and glassy carbon for Br half-cells, respectively). The interfacial electrical double-layer (EDL) which forms during the charging phase of the battery was studied this way. The calculated DCs had maximum error of 8% for the Zn half-cell (for the –0.2 to +0.1 V *vs* OCP range studied) while the Br side produced values within ±1% (for the –0.2 to +0.2 V *vs* OCP range studied).

7.3.3. Preparation and characterization of zinc electrodeposits

Zinc electrodeposits were galvanostatically prepared (4 minutes charging at 20 mA cm^{-2} current density) from each of the electrolytes studied using a two-electrode cell configuration with glassy carbon electrodes according to procedures and conditions described in previous work.[156] The prepared deposits were rinsed, vacuum-dried and kept under vacuum before characterization *via* SEM and XRD analysis under similar conditions to that study, in order to prevent oxidation of samples. The XRD data obtained was subsequently analyzed using the PDF4+ software database for identification of zinc peaks. XRD peak data was also analyzed *via* the Williamson–Hall method[170,171] in order to semi-quantitatively compare the relative sizes of zinc crystals generated from each solution during the initial stages of the charging process. This was carried out to investigate the influence of IL type and mixing proportion on zinc electrodeposition crystallinity. Sample peak results were referenced against a LaB$_6$ standard (NIST SRM 660a) which was selected for its well-defined peaks. The

diffraction angle θ was used to calculate the full width at half maximum (FWHM, β) using an equation similar to Eq. 3-2 in Chapter 3, with terms carrying similar meaning.

7.4. Results and discussion

7.4.1. Physical properties of electrolytes containing pure and mixed BSAs

The pH and ionic conductivity of each freshly prepared testing solution containing 2.5 M ZnBr$_2$ primary electrolyte and the 0.8 M BSA mixture were measured using a labCHEM-CP instrument (TPS Ltd., Brisbane, Australia). These physical properties are presented in Table 7-1, including a numerical convention for ease of reference.

Table 7-1 Physical properties of aqueous electrolytes containing five different BSA formulations at $25\pm1°C$.

Proportion of 0.8 M BSA Mixture in 2.5 M ZnBr$_2$ Primary Electrolyte Solution (with Numerical Shorthand for Reference)	pH	Conductivity (mS cm^{-1})
100% [C$_2$MPyrr]Br (**1**)	2.56 ± 0.04	51.8 ± 0.4
75% [C$_2$MPyrr]Br + 25% [C$_2$MIm]Br (**2**)	2.34 ± 0.02	54.1 ± 0.6
50% [C$_2$MPyrr]Br + 50% [C$_2$MIm]Br (**3**)	2.29 ± 0.01	52.5 ± 0.5
25% [C$_2$MPyrr]Br + 75% [C$_2$MIm]Br (**4**)	2.21 ± 0.01	54.1 ± 0.2
100% [C$_2$MIm]Br (**5**)	2.19 ± 0.02	55.1 ± 0.3

Electrolytes with a higher proportion of [C$_2$MIm]Br gave lower pH values, with solutions containing **4** and **5** giving comparable values. From these results, it is clear that [C$_2$MIm]$^+$ has a stronger acidity than [C$_2$MPyrr]$^+$, hence giving rise to greater system acidity. This behavior is attributed to the delocalized cationic structure of the dissociated [C$_2$MIm]$^+$ ion, whereby dissociation of water is promoted *via* a relatively stronger binding between [C$_2$MIm]$^+$ (compared to [C$_2$MPyrr]$^+$) and OH$^-$ (from water). This phenomenon results in a higher proportion of labile H$^+$ (also from water) present in those solutions, which in turn leads to the lower pH observed. Conductivities were

comparable between solutions employing **1** and **3**, as well as between those with **2** and **4**, while electrolytes utilizing **5** produced the highest conductivity. Generally, an increasing proportion of $[C_2MIm]^+$ served to improve conductivity, potentially due to the presence of its delocalized positive charge. The potential influences of these physical properties on half-cell electrochemical performances and zinc electrodeposition behavior are presented and discussed in subsequent sections.

7.4.2. Half-cell electrochemical performance and behavior

Zn half-cell CV, Tafel, EIS and DC

Zn half-cell cyclic voltammograms of electrolytes containing the different hybrid IL mixtures are presented in Figure 7-1. The electrochemical performance of each solution is determined using the reduction (*red*) and oxidation (*ox*) scans through the following metrics, as described in a previous report:[156] highest-magnitude current (*j*), charge (*Q*), maximum power (*P**) and energy (*E**) densities, where the latter two values are calculated with reference to Ag/AgCl. The nucleation overpotential (NOP) is also calculated for zinc electrodeposition and stripping in that half-cell based on the difference in deposition (DP) and cross-over potentials (COP). These values, including their efficiencies (*eff*) based on comparison of the forward and reverse scans, are presented in Table 7-2. *P**, *j*, DP, COP and the electrode potential (j_{ox-E}) of reverse scan peaks are obtained directly from CV measurements while *Q* and *E** are calculated from *P** and *j*, respectively, for the duration of each scan.

Figure 7-1. Zn half-cell CV for electrolytes containing the five BSA formulations studied in the present work (molar proportions): **1** 100% [C₂MPyrr]Br (solid red line), **2** 75% [C₂MPyrr]Br + 25% [C₂MIm]Br (dashed green line), **3** 50% [C₂MPyrr]Br + 50% [C₂MIm]Br (solid blue line), **4** 25% [C₂MPyrr]Br + 75% [C₂MIm]Br (dashed blue line), and **5** 100% [C₂MIm]Br (dotted red line).

Table 7-2. Zn half-cell CV of electrolytes containing five different BSA formulations.

BSA	1	2	3	4	5
$j_{red} \pm 0.2$, mA cm^{-2}	-25.0	-25.2	-21.9	-28.2	-29.4
$j_{ox} \pm 0.4$, mA cm^{-2}	14.3	14.2	11.8	13.2	17.2
$j_{ox\text{-}E} \pm 1$, mV	-772	-769	-769	-779	-764
$Q_{red} \pm 1.2$, mC cm^{-2}	93.3	97.1	84.0	109.7	113.3
$Q_{ox} \pm 4.1$, mC cm^{-2}	55.6	68.4	61.2	79.7	82.4
$Q_{eff} \pm 3.6$, %	59.6	70.5	72.9	72.6	72.7
$P^*_{red} \pm 0.2$, mW cm^{-2}	25.0	25.2	21.9	28.2	29.4
$P^*_{ox} \pm 0.3$, mW cm^{-2}	11.0	10.9	9.1	10.3	13.2
$P^*_{eff} \pm 0.6$, %	44.0	43.4	41.6	36.4	44.8
$E^*_{red} \pm 1.2$, mJ cm^{-2}	89.7	93.3	80.7	105.3	108.9
$E^*_{ox} \pm 1.4$, mJ cm^{-2}	36.1	42.4	36.6	43.9	51.9
$E^*_{eff} \pm 1.5$, %	40.3	45.5	45.4	41.7	47.6
DP ± 1, mV	-935	-923	-922	-914	-915
COP ± 1, mV	-857	-854	-855	-854	-855
NOP ± 1, mV	79	68	68	59	61

Generally, a higher proportion of [C₂MIm]Br improved Zn half-cell performance. Solutions containing **5** produced the overall best electrochemical performance in the

131

Zn half-cell on the basis of all testing metrics applied, while those utilizing **4** gave slightly lower values and the remaining solutions performed even poorer. The magnitude of the potential at which the stripping peak was recorded was similar for solutions with **1**-**3**, while those of the best-performing **4** and **5** had the highest and lowest magnitude values, respectively. On the basis of j and P^*, electrolytes using **3** gave the poorest electrochemical performance while those with 1 performed the worse with regards to Q and E^*. Small amounts of [C$_2$MPyr]Br decrease P_{eff}^* while the presence of even a small proportion of [C$_2$MIm]Br improves Q_{eff}. These results suggest that Zn half-cell performance potentially benefits from employing ILs with a delocalized cationic charge (i.e. [C$_2$MIm]Br), which is consistent with previous investigations on such BSAs.[246,252]

CV and Tafel measurements indicate that the type and amount of BSA present influences half-cell performance. It is proposed that for this half-cell: (a) the use of non-equimolar BSA mixtures is detrimental to performance; and (b) while the addition of small amounts of either BSA are potentially beneficial (depending on the metric used), pure ILs are likely to be overall most effective. Furthermore, it was observed that COP for all solutions was similar whereas the magnitude of DP decreased as [C$_2$MIm]Br concentration was increased. It was also observed that lower NOP values were linked to solutions which also gave better half-cell performance. The following Tafel fitting parameters from analysis of zinc half-cell Tafel plots for each solution (Figure 7-2) are presented in Table 7-3: exchange current density (i_0) and the corresponding potential (E_0), anodic (β_a) and cathodic (β_c) beta constants, and polarization resistance (R_p). Parametric values obtained were generally similar for all solutions except those containing **4**, which gave the highest magnitude values.

Additionally, a higher proportion of [C$_2$MIm]Br appears to lower R_p, which in turn is linked to better CV performance in this half-cell.
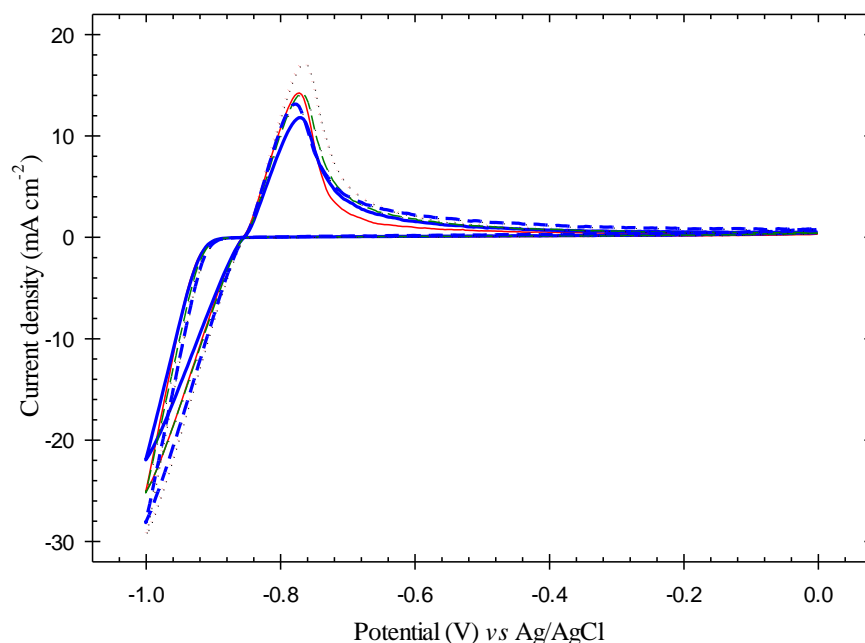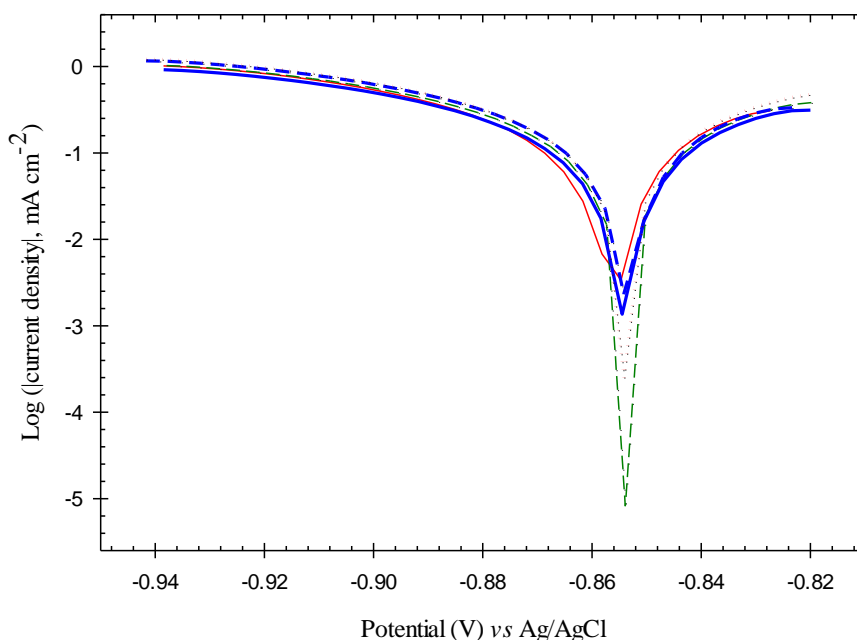

Figure 7-2. Zn half-cell Tafel plots for electrolytes containing the five BSA formulations studied in the present work (molar proportions): **1** 100% [C$_2$MPyrr]Br (solid red line), **2** 75% [C$_2$MPyrr]Br + 25% [C$_2$MIm]Br (dashed green line), **3** 50% [C$_2$MPyrr]Br + 50% [C$_2$MIm]Br (solid blue line), **4** 25% [C$_2$MPyrr]Br + 75% [C$_2$MIm]Br (dashed blue line), and **5** 100% [C$_2$MIm]Br (dotted red line).

Table 7-3. Tafel fitting parameters for the Zn half-cell.

BSA	1	2	3	4	5
$i_0 \pm 1.18$, mA cm^{-2}	0.85	1.78	1.68	4.94	2.32
$E_0 \pm 1$, mV	-856	-854	-854	-854	-854
$\beta_a \pm 15$, mV dec^{-1}	41	69	73	305	68
$\beta_c \pm 16$, mV dec^{-1}	59	81	83	131	86
$R_p \pm 6$, Ω	99	94	106	88	79

EIS results offer some explanation of trends observed during CV, namely the behavior and influence of each BSA formulation in the half-cell. Zinc half-cell Nyquist plots for each solution are presented in Figure 7-3. Values of elements from a proposed

simple equivalent circuit model (inset of Figure 7-3) fitted using the Simplex method are tabulated in Table 7-4. As with the case in previous chapters, while the Nyquist profiles show depressed semi-circles and possibly more than one time constant characteristic, the simplest equivalent circuit model was utilized as a first-pass fitting even though adding more circuit elements would have allowed for a better fit but not directly attributable to a physical/electrochemical process.

Figure 7-3. Zn half-cell Nyquist plots for electrolytes containing the five BSA formulations studied in the present work (molar proportions): **1** 100% [C$_2$MPyrr]Br (solid red line), **2** 75% [C$_2$MPyrr]Br + 25% [C$_2$MIm]Br (dashed green line), **3** 50% [C$_2$MPyrr]Br + 50% [C$_2$MIm]Br (solid blue line), **4** 25% [C$_2$MPyrr]Br + 75% [C$_2$MIm]Br (dashed blue line), and **5** 100% [C$_2$MIm]Br (dotted red line). Raw data points (thin crosses or triangles) indicated for the fitted lines they overlay, for clarity. Inset shows the equivalent circuit model used to simulate each curve.

Table 7-4. Zn half-cell equivalent circuit element values from modelling of impedance curves.

BSA	1	2	3	4	5
R_1, Ω	56.6 ± 2.8	56.3 ± 2.8	62.7 ± 3.1	54.3 ± 2.7	51.7 ± 2.6
C_2, µF	44.9 ± 2.2	58.3 ± 2.9	53.4 ± 2.7	47.4 ± 2.4	43.8 ± 2.2
R_2, Ω	24.1 ± 1.2	16.0 ± 0.8	16.7 ± 0.8	14.7 ± 0.7	12.9 ± 0.6
W_2, $\Omega.s^{-0.5}$	5.53 ± 0.28	5.02 ± 0.25	4.92 ± 0.25	3.90 ± 0.19	4.15 ± 0.21

Although there is a suppressed arc consistently present in all the impedance spectra obtained from EIS scans (when viewed isotropically), the proposed simple circuit is deemed appropriate for preliminary analysis due to the single-time-constant behavior observed. The following sources of electrochemical impedance are included in this model: solution resistance (R_1), charge-transfer resistance (R_2), EDL capacitance (C_2) and Warburg diffusion limitation (W_2). Solutions having lower R_1 and W_2 values gave better electrochemical performance than other electrolytes during CV tests, suggesting that these parameters have a large degree of influence over zinc half-cell behavior. The higher mobility of ions in solution (as indicated by low R_1) and lower diffusion limitations (low W_2) are consistent with, and supported by, the observation of lower pH values which were in turn attributed to a higher proportion of anions in solution. A lower R_2 is observed for electrolytes containing a higher proportion of [C_2MIm]Br, which is consistent with observations from previous studies involving such ILs.[246,252] It is also noted that zinc-side EIS scans from those studies also produced similar suppressed-arc Nyquist plots, suggesting that the electrochemical measurements at this electrode are influenced by factors and processes in addition to the zinc reaction.

Generally higher C_2 was produced by electrolytes containing binary IL mixtures compared to those utilizing a single IL type, and is attributed to relatively denser packing of EDL ions at the electrode-electrolyte interface within the former solutions. DC tests confirmed adsorptive behavior of electrolyte species on the surface of the working electrode, with potentials further from OCP producing increasingly higher DC values than those at OCP. Electrolytes containing **1** and **5** generally gave the lowest and highest values, respectively, while other solutions produced mid-range values. It is known that the type, size and shape of IL cation can influence EDL structure,

capacitance and behavior, whereby larger ions lead to looser packing and hence lower capacitance.[201,248] This dependence provides some explanation for the differing capacitive behavior observed in the solutions studied. The interaction of each BSA with other ions and the electrode surface, as well as between the BSAs themselves (in hybrid mixtures), influences both the EDL structure and bulk electrolyte behavior, consequently varying the capacitances observed.

Given that the difference between each electrolyte is the mixing proportion of BSAs, and from observations of impedance behavior, it is proposed that the structures and interactions of these BSAs influence zinc half-cell performance. Specifically: (a) the delocalized cationic structure of $[C_2MIm]^+$ promotes the formation of relatively densely-packed EDL structures which in turn positively facilitate zinc reduction by lowering diffusion limitations and charge-transfer resistances compared to solutions containing higher proportions of $[C_2MPyrr]^+$ with its localized cationic structure; and (b) BSAs in solution strongly interact with other primary electrolyte ions and affect their behavior (e.g. influencing properties such as mobility within the solution), which consequently determines electrochemical performance of the half-cell.

Br half-cell CV, EIS and DC

Br half-cell cyclic voltammograms of the electrolytes studied are presented in Figure 7-4. Key electrochemical parameters measured during CV (as described earlier for the Zn-side) in the Br half-cell are tabulated in Table 7-5.
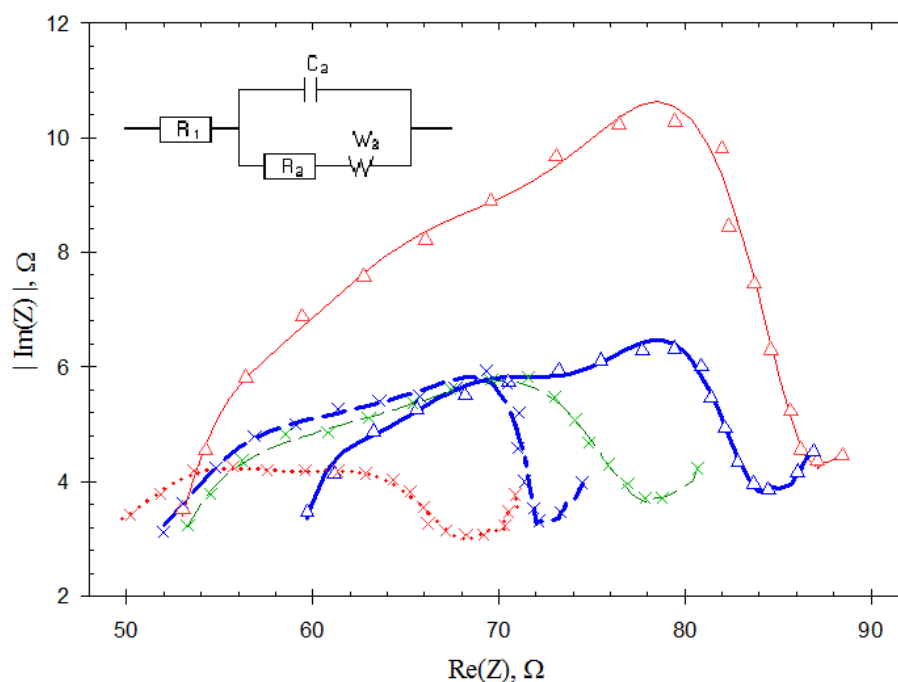
Figure 7-4. Br half-cell CV for electrolytes containing the five BSA formulations studied in the present work (molar proportions): **1** 100% [C$_2$MPyrr]Br (solid red line), **2** 75% [C$_2$MPyrr]Br + 25% [C$_2$MIm]Br (dashed green line), **3** 50% [C$_2$MPyrr]Br + 50% [C$_2$MIm]Br (solid blue line), **4** 25% [C$_2$MPyrr]Br + 75% [C$_2$MIm]Br (dashed blue line), and **5** 100% [C$_2$MIm]Br (dotted red line).

Table 7-5. Br half-cell CV of electrolytes containing five different BSA formulations.

BSA	1	2	3	4	5
$j_{red} \pm 0.012$, mA cm^{-2}	-0.695	-0.557	-0.532	-0.529	-0.534
$j_{ox} \pm 0.12$, mA cm^{-2}	3.90	3.26	3.01	2.91	2.94
$j_{ox-E} \pm 9$, mV	717	727	727	730	734
$Q_{red} \pm 0.14$, mC cm^{-2}	8.86	6.42	6.42	6.32	6.36
$Q_{ox} \pm 0.38$, mC cm^{-2}	10.97	9.01	8.23	7.95	8.05
$Q_{eff} \pm 3.7$, %	80.8	71.2	78.0	79.4	79.0
$P*_{red} \pm 0.009$, mW cm^{-2}	0.501	0.406	0.389	0.388	0.394
$P*_{ox} \pm 0.12$, mW cm^{-2}	3.90	3.26	3.01	2.91	2.94
$P*_{eff} \pm 0.1$, %	12.9	12.5	12.9	13.4	13.4
$E*_{red} \pm 0.09$, mJ cm^{-2}	4.50	3.52	3.40	3.36	3.39
$E*_{ox} \pm 0.35$, mJ cm^{-2}	10.58	8.69	7.94	7.68	7.77
$E*_{eff} \pm 1.1$, %	42.5	40.5	42.8	43.8	43.6

The difference of Br-side values being about one or two orders of magnitude lower than that of the Zn-side was expected due to the presence of an additional (*viz.* sequestration) step in the Br half-cell which may be an operational limitation,[253] and recently reviewed.[95,254] This challenge is conventionally compensated-for by employing electrodes with higher exposed surface area compared to the zinc-side electrode, as discussed in a recent review.[95] Since similar smooth glassy carbon working electrodes with consistent surface area are used to study both half-cells in the present study, Br-side performance is lower than that of the Zn-side.

The overall best electrochemical performance in the Br half-cell, on the basis of j and Q, was obtained for solutions of **1**, while those containing **2** gave slightly lower values. The other electrolytes gave comparable measurements which were even lower than the former two. The reduction peak during the reverse scan was obtained at similar potentials for all solutions tested. The trend of electrolytes containing a higher proportion of [C$_2$MIm]Br decreasing Br half-cell performance was generally maintained. Those employing **2** gave the lowest Q_{eff}, $P_{eff}*$ and $E_{eff}*$, whereas **1** produced the highest Q_{eff}, and the increased presence of [C$_2$MIm]Br gave the highest $P_{eff}*$ and $E_{eff}*$ compared to other electrolytes. The results suggest that generally better CV performance can be obtained in the Br half-cell from solutions containing BSAs possessing a localized cationic charge (i.e. [C$_2$MPyrr]Br) compared to those having a delocalized charge (i.e. [C$_2$MIm]Br). However, the findings also indicate that a higher proportion of the latter BSA type may benefit $P_{eff}*$ and $E_{eff}*$ in that half-cell.

Br-side Nyquist plots for each electrolyte are presented in Figure 7-5. The EIS data obtained were fitted with a simple equivalent circuit (see inset of Figure 7-5) due to the single-time-constant behavior of impedance spectra in this half-cell as well, and the results presented in Table 7-6.
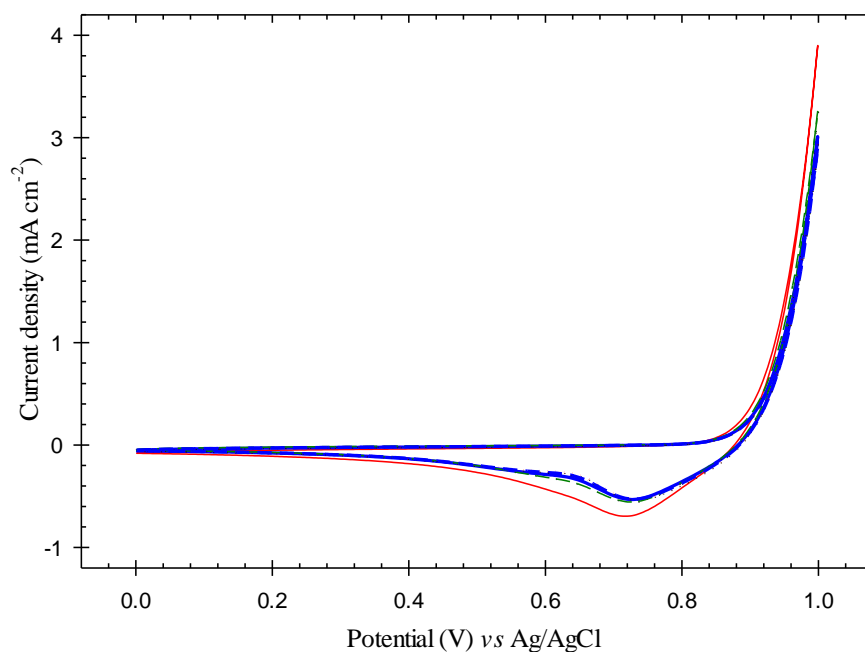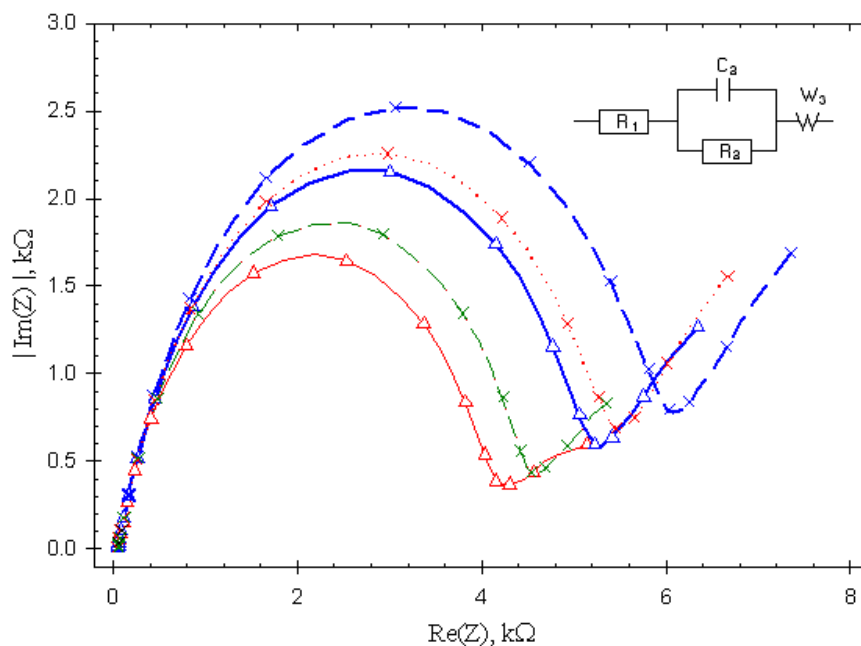
Figure 7-5. Br half-cell Nyquist plots for electrolytes containing the five BSA formulations studied in the present work (molar proportions): **1** 100% [C$_2$MPyrr]Br (solid red line), **2** 75% [C$_2$MPyrr]Br + 25% [C$_2$MIm]Br (dashed green line), **3** 50% [C$_2$MPyrr]Br + 50% [C$_2$MIm]Br (solid blue line), **4** 25% [C$_2$MPyrr]Br + 75% [C$_2$MIm]Br (dashed blue line), and **5** 100% [C$_2$MIm]Br (dotted red line). Raw data points (thin crosses or triangles) indicated for the fitted lines they overlay, for clarity. Inset shows the equivalent circuit model used to simulate each curve.

Table 7-6. Br half-cell equivalent circuit element values from modelling of impedance curves.

BSA	1	2	3	4	5
R_1, Ω	56.0 ± 0.6	56.3 ± 0.6	51.5 ± 0.5	51.2 ± 0.5	51.4 ± 0.5
C_2, μF	2.93 ± 0.03	3.12 ± 0.03	3.37 ± 0.03	3.58 ± 0.04	3.53 ± 0.04
R_2, kΩ	3.30 ± 0.03	3.55 ± 0.04	3.96 ± 0.04	4.49 ± 0.04	4.07 ± 0.04
W_2, kΩ.$s^{-0.5}$	1.01 ± 0.01	1.12 ± 0.01	1.51 ± 0.02	1.86 ± 0.02	1.67 ± 0.02

The elements of this circuit refer to similar phenomena as those used to model the Zn-side Nyquist curves. R_1 is higher for solutions containing larger amounts of [C$_2$MPyrr]Br (i.e. **1** and **2**), whereas the converse is observed for values of R_2 and W_2. This suggests that the resistances due to charge-transfer and diffusion limitations have a larger influence on Br half-cell performance observed during CV, compared to the

mobility of ions within the bulk electrolyte itself. These influences, together with physical properties such as pH, are attributed to the localized/delocalized charge of the BSA structures and their interactions with each other, as well as other ions, in solution.

The following possible explanations are proposed for the electrochemical phenomena observed: (a) [C$_2$MPyrr]Br sequesters elemental bromine stronger than [C$_2$MIm]Br does due to the localized cationic charge of the former IL, consequently reducing resistances to diffusion and of charge-transfer; (b) the existence of two types of BSAs with differing degrees of charge distribution (due to different cationic structures), especially in equimolar proportions, generates competition during bromine sequestration due to strong interactions between the ILs and the electrode interface, thereby decreasing Br half-cell performance than if a single IL was used.

C$_2$ also generally increases with higher proportions of [C$_2$MIm]Br. Results from DC tests are consistent with the presence of adsorbed species on the working electrode, with higher electrode potentials leading to higher DC values. Generally higher DCs were observed for solutions containing higher proportions of [C$_2$MIm]Br at potentials equal to and lower than the OCP, while the converse was observed at higher potentials. This observation is attributed to changes in the packing density of ions forming the EDL, possibly due to the interactions of the BSAs with the electrode surface and/or the presence of more bromide anions (from the BSA) present in the EDL due to weaker interactions between the cation and counter-ion of [C$_2$MIm]Br (*viz.* [C$_2$MIm]$^+$ and Br$^-$, respectively).

7.4.3. Characterization of zinc electrodeposits: SEM, XRD and WH analysis

Zinc electrodeposits produced during the initial stages of charging of the Zn/Br cell at 20 mA cm^{-2} current density were analyzed *via* SEM. Micrographs of deposits from electrolytes employing the various mixed BSAs are presented in Figure 7-6. The proportion and type of BSA present is observed to influence zinc deposit morphology, which is to be expected as organic additives in electrolytes are known to influence the preferential orientation zinc electrodeposits.[249] While the presence of a single IL type (**1** and **5**) promotes the formation of mossy deposits with needle-like structures, generally more crystalline deposits are obtained from the use of the mixed BSAs **2**–**4**. Compared to equimolar BSA mixtures (**3**), increasing the molar proportion of either IL (towards **1** or **5**) appears to increase the size of zinc clusters and crystal sizes observed while reducing the smoothness and uniformity of deposits. These observations of BSAs influencing zinc electrodeposition are consistent with behavior seen during electrochemical tests. The presence of dendrites in solutions of **1** and **5** is potentially attributed to fast deposition kinetics in those cases, while the suppression of dendritic zinc growth from solutions containing **2**–**4** is attributed to sluggish kinetics due to inter-IL interactions which lead to zinc ions being more evenly distributed onto the electrode surface and hence able to form more uniform electrodeposits.
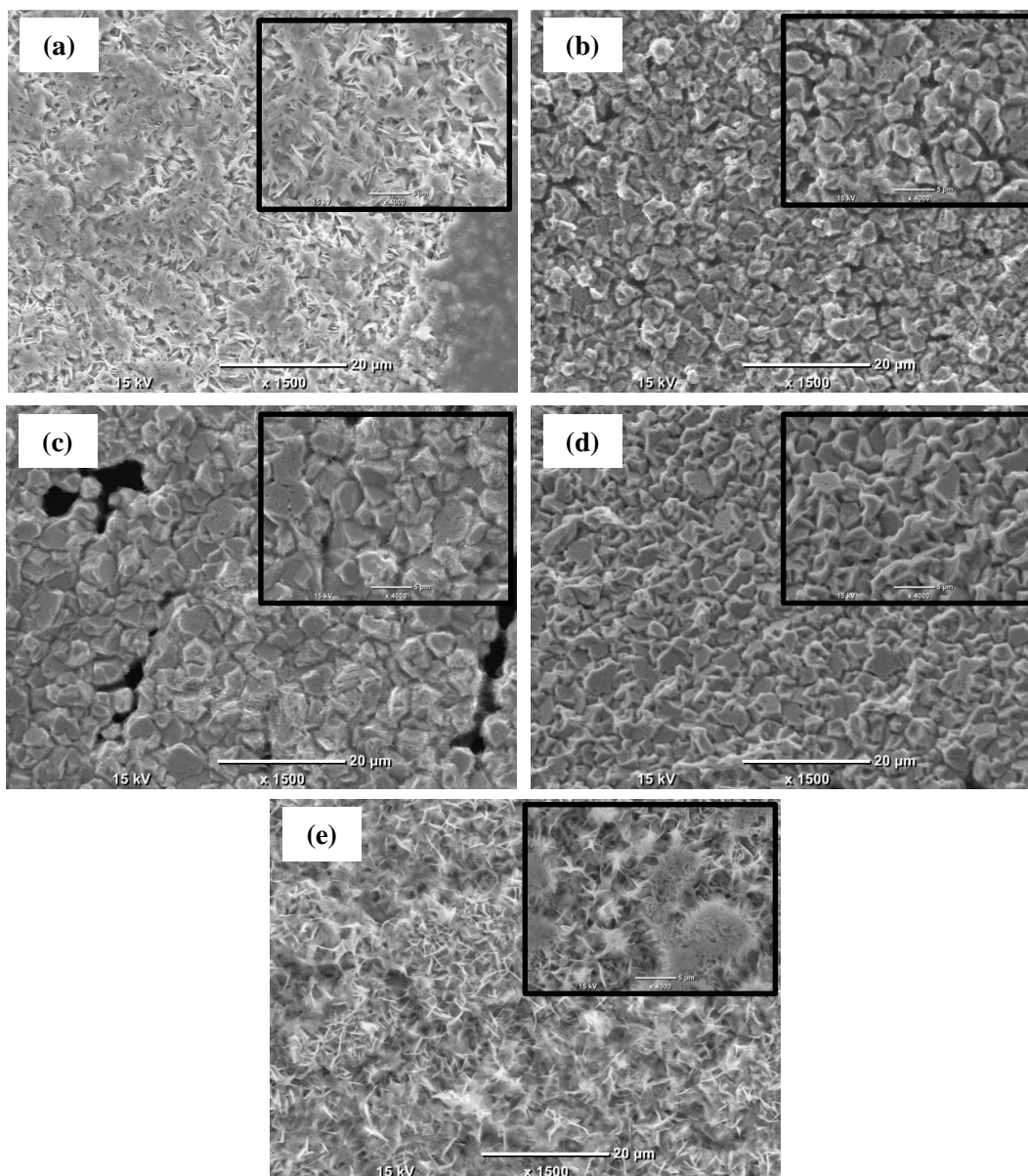
Figure 7-6. SEM images (20 µm scale for large images, 5 µm scale for insets) of zinc deposits obtained after 4 minutes of charging at 20 mA cm^{-2} current density from electrolytes containing the five BSA formulations studied in the present work (molar proportions): (a) **1** 100% [C$_2$MPyrr]Br, (b) **2** 75% [C$_2$MPyrr]Br + 25% [C$_2$MIm]Br, (c) **3** 50% [C$_2$MPyrr]Br + 50% [C$_2$MIm]Br, (d) **4** 25% [C$_2$MPyrr]Br + 75% [C$_2$MIm]Br, and (e) **5** 100% [C$_2$MIm]Br.

Raw diffractograms from XRD characterization of the zinc deposits are presented in Figure 7-7. The crystal orientations of each deposit were identified *via* the PDF4+ database (PDF card #04-014-0230) and further compared against previous reports on zinc electroplating out of ZnBr$_2$ solutions[90,182] for confirmation. These Miller indices are indicated above the relevant peaks on the corresponding diffractograms.
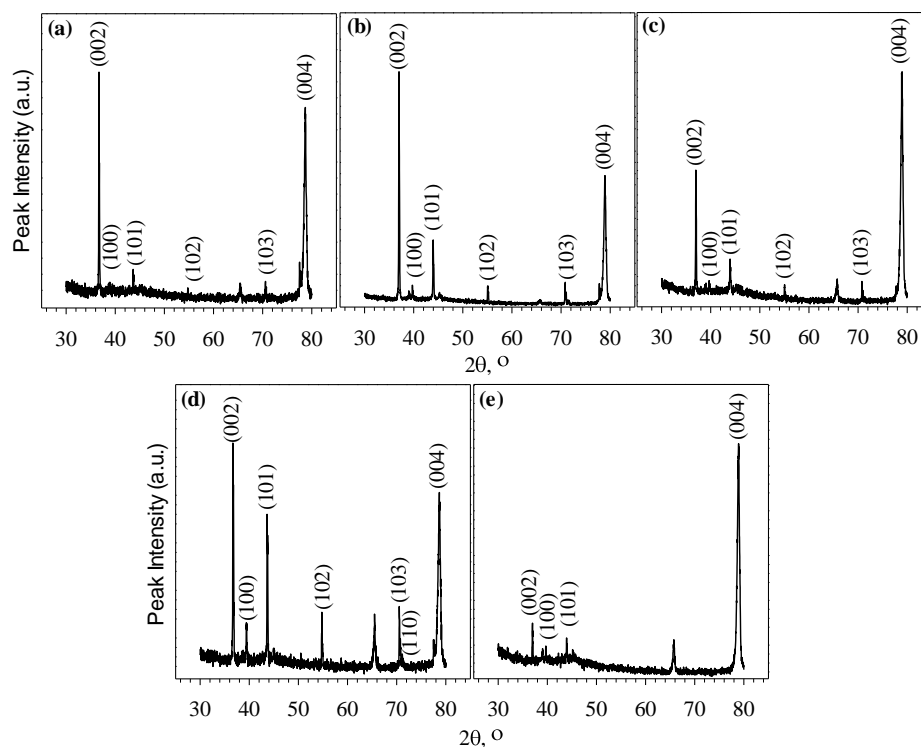
Figure 7-7. Diffractograms (with Miller indices of zinc peaks indicated after identification during post-processing) from XRD analysis of zinc deposits obtained after 4 minutes of charging at 20 mA cm^{-2} current density from electrolytes containing the five BSA formulations studied in the present work (molar proportions): (a) **1** 100% [C$_2$MPyrr]Br, (b) **2** 75% [C$_2$MPyrr]Br + 25% [C$_2$MIm]Br, (c) **3** 50% [C$_2$MPyrr]Br + 50% [C$_2$MIm]Br, (d) **4** 25% [C$_2$MPyrr]Br + 75% [C$_2$MIm]Br, and (e) **5** 100% [C$_2$MIm]Br.

A strong preference for zinc structures with basal orientations was identified across all samples. It was also observed that electrolytes containing mixed BSAs (**2**–**4**) yielded deposits with a secondary preference for (101) configurations. Diffraction peaks attributed to the (100), (102) and (103) orientations were generally present at relatively lower intensities for almost all samples analyzed. The latter two configurations are only present in mixtures containing [C$_2$MPyrr]Br, suggesting that those Miller indices are associated with this IL for such systems. The mixture of preferred basal configurations with some non-basal reflections is consistent with morphologies observed under SEM. These findings have implications for future zinc-side electrolyte formulations, given that crystal configurations are related to electrochemical

performance in that half-cell[90,149] and better control of the former may benefit the latter.

XRD peak data was further analyzed *via* the WH method to study the influence of each BSA formulation on zinc crystals generated. Compared to crystals obtained from equimolar IL mixtures (**3**), those from solutions with a higher proportion of [C$_2$MPyrr]Br (**1**-**2**) were up to 1.5 times larger, whereas the increased presence of [C$_2$MIm]Br (**4**-**5**) gave crystals more than 3 times larger than the equimolar base case. Interestingly, crystal strain decreases with increased proportions of [C$_2$MPyrr]Br (compared to equimolar mixtures, **3**), whereas the converse is observed for electrolytes utilizing greater amounts of [C$_2$MIm]Br. A possible link is identified between decreasing NOP values and increasing crystal strain, where such phenomena are indicative of improved Zn half-cell performance. While compact deposits are conventionally linked to better battery performance,[149] observations from CV tests within the present work indicate otherwise. The differences in crystal morphology and other characteristics during charging are attributed to interactions between BSA ions and zinc: either (a) directly with zinc electrodeposits, or (b) zinc complexes in solution, or possibly a combination of (a) and (b). Molecular modeling studies are underway to investigate these possibilities.

The different surfaces of zinc electrodeposits obtained from each electrolyte, combined with earlier findings that the surface morphology of an electrode can influence the DC of that system,[250] also provide some explanation towards the different capacitances (associated with packing density and structure of the EDL) observed during electrochemical impedance tests.

7.4.4. The influence of hybrid IL mixtures on Zn/Br half-cells

Observations of half-cell CV performance, electrochemical analysis, and zinc electrodeposition behavior indicate that the BSAs studied have influence over system operation. Specifically, the structure of the ILs used influence how they interact with each other (in hybrid solutions) as well as other electrolyte species. There is possibly some competition between the BSAs for bromine sequestration, and a similar interaction with zinc ions. It appears that different physical properties (e.g. low *vs* high pH) might benefit each half-cell differently, by way of influencing the major contributors to electrochemical impedance within the cell environment. Further to this, while a BSA concentration of 0.8–1 M is typically used in Zn/Br electrolyte formulations, this range may not necessarily apply for the case of the hybrid ILs studied in the present work.

A number of interesting comparisons can be made between results from the present study and those of single-type BSAs previously reported in Chapter 6. It is to be noted that electrolytes used in the earlier study contained potassium chloride and zinc chloride as supporting electrolytes, consequently producing solutions with higher ionic conductivity than those used in the present work. Furthermore, graphite-coated working electrodes with a relatively higher exposed surface area were used in that study, compared to the commercial glassy carbon electrodes in this one. Despite these differences, higher current, charge, power and energy densities are obtained in the zinc half-cell using glassy carbon electrodes (i.e. this work). However, better zinc half-cell efficiencies were obtained using the graphite-electrode setup. Besides the higher solution conductivity of electrolytes in the earlier study, this phenomenon can also be attributed to the relatively lower NOP and faster kinetics of zinc electrodeposition and stripping on graphite. Comparatively, the de-plating of zinc from glassy carbon

surfaces within the electrolyte formulations of the present work is sluggish and potentially incomplete, with zinc deposits still remaining on the electrode surface at the end of the reverse scan cycle.

It is also interesting to note that a similarity between these studies is the link between solutions generating zinc electrodeposits with basal configurations also producing better electrochemical performance in that half-cell, while the increasing presence of non-basal reflections is generally linked to a decrease in performance. This consistency suggests that careful control of flow patterns within the full-cell setup to achieve desirable zinc deposit configurations could potentially improve system performance.

Results from separate on-going studies involving a wider range of ILs (including those studied in the present work) have led to the in-depth discussion and proposal of bromo-zincate[209,219,251] complexes being a possible reason for changing the electrochemical behavior in both half-cells as a direct consequence of altering the BSA formulation employed therein. In essence, the presence of additional bromides in solution from dissociation of the BSA into its cation and bromide counter-ion would shift the equilibrium towards formation of additional zinc complexes, which in turn influences half-cell performance due to the resultant factors discussed in earlier sections. The availability of additional bromides would depend on the strength of the ion pair association between the BSA cation and its bromide counter-ion. It is also proposed that these complexes are further interacting with the cation of the BSA as well, such as *via* dipole interactions with water-coordinated zinc and/or anionic zinc-bromide complexes.

It is necessary to study these IL mixtures in full-cell configurations to further understand and characterize their behavior in practical systems. It is also important to understand the physical and (electro)chemical stability and nature (miscibility with the

aqueous electrolyte solution, etc.) of the bromine-sequestered complexes formed at various states of charge during cell operation. Similarly, the equilibrium bromine vapor pressure of the electrolytes containing single-type and mixed-BSAs need to be studied within the intended operating range of temperatures – these studies are on-going.

Overall, the results of this study suggest that pure BSAs perform better in each half-cell than hybrid solutions. Consequently, it is likely that improvements to system performance can be achieved by making changes to conventional Zn/Br RFB architecture which would in turn allow for different electrolyte formulations and therefore different BSAs (or additives, in the case of the Zn half-cell) to be used in the circulatory loops servicing each half-cell. However, such an arrangement would need to consider the possible migration of ILs across the membrane separator which would in turn eventually produce a mixed-BSA electrolyte after extended cell operation, and lead to degraded cell performance as indicated by half-cell studies presented in this work. Such migration could be minimized by the use of ion-selective membranes at considerably higher cost.

7.5. Chapter conclusions

Electrochemical tests were carried out in both half-cells of a Zn/Br flow battery to study the effect of utilizing pure and hybrid BSAs in the electrolyte. The two BSAs studied, [C_2MIm]Br and the typically-used [C_2MPyrr]Br, were studied at 5 different molar proportions amounting to 0.8 M in solution: 1:0, 3:1, 1:1, 1:3 and 0:1, respectively. On the basis of half-cell electrochemical performance of the solutions studied in this work, electrolytes containing a single IL type are better suited for Zn/Br systems compared to those utilizing hybrid mixtures. [C_2MIm]Br is most beneficial for Zn-side operation, while the conventional BSA [C_2MPyrr]Br remains the best

option for the Br-side under the testing conditions employed. Electrolytes producing lower charge-transfer resistance and diffusion limitation during EIS were linked to good CV performance in both half-cells, in addition to lower polarization resistance on the Zn-side. SEM and XRD characterization of the zinc deposits produced during charging of the Zn/Br system showed that the type and proportion of IL influences zinc electrodeposit morphology. The electrochemical behavior observed, combined with findings from analysis of zinc deposits, strongly suggest that the BSAs are interacting at the electrode–electrolyte interface with each other (in hybrid mixtures) as well as other ions in the electrolyte, consequently affecting performance in both the Zn and Br half-cells.

Although the particular combination of [C$_2$MPyrr]Br and [C$_2$MIm]Br was selected for this work based on previous success utilizing solutions of the latter BSA, the initial results of the present study suggest this particular combination is unsuitable for use in Zn/Br systems. However, it is possible that further investigations of other hybrid BSA solutions in full-cell systems, as well as fundamental and full system studies involving other hybrids combinations, could still lead to improved electrochemical performance. It is expected that findings from this study has the potential to prompt work in re-designing Zn/Br flow battery electrolyte formulations and architectures to improve system performance.

The next chapter presents overall conclusions and recommendations based on the findings of work detailed in this and earlier chapters (3–5). Studies to understand and improve Zn/Br RFB systems, as well as future outlook for the technology, are also discussed.

8. Overall Conclusions and Strategies Forward for Zn/Br RFB Development

8.1. Overall conclusions and recommendations

This thesis presented a technical overview of some short- and long-term challenges to ZBB development, with some corresponding potential solutions. Although the suggestions in this chapter have been developed and listed for ZBBs, it is possible that some can be easily adjusted and adapted for use in other types of RFBs with similar characteristics.

Based on the literature reviewed and original work presented in this thesis, it can be concluded that significant improvements to Zn/Br system performance can be made by the strategic use of materials to overcome internal resistances and losses. It is recommended that beneficial alternatives to conventional chloride-based supporting electrolytes are used, and that ionic liquids possessing a delocalized cationic charge be further investigated for both bromine-sequestration and zinc-side additive purposes. While the binary ionic liquid mixture studied as part of this thesis was not particularly effective at improving half-cell operation, it is possible that further testing of alternative combinations might prove beneficial.

Overall, it is concluded that results from the combination of molecular simulations, electrochemical investigations and physical characterization work undertaken has been successful in answering the central question of this thesis stated in the introductory chapter:

"What are some beneficial compounds for Zn/Br battery performance, and what are their roles and influences in achieving this effect?"

8.2. Future work and strategies forward

From the technological challenges described in previous chapters, some promising strategies have been formulated for increasing knowledge about and improving the electrochemical and physical processes of Zn/Br systems, particularly at the electrode–electrolyte interface. These focused strategies have been condensed and collated in a separate work,[255] aimed at improving Zn/Br flow battery technology. New-found understanding from fundamental studies would allow clear identification of promising investigative pathways and reduce the time and effort involved in developing tailor-made solutions to reduce or circumvent internal sources of losses (e.g. due to undesirable side reactions), consequently reducing costs while improving operating efficiencies and practical specific energy.

For maximum gain, it is proposed that short-term research is carried out on two fronts, namely computer modeling and electrochemical studies. That combination would allow rapid discovery and implementation of solutions, both for developing novel materials and for characterizing the Zn/Br system's behavior under various combinations of physicochemical conditions.

Simulations using sophisticated modeling techniques with adjustments based on accurate empirical parameters and correlations would significantly minimize the time and cost of the experimental investigations required to develop suitable materials for use in Zn/Br batteries. These simulations include periodic density functional calculations and multi-physics models of the system. On the experimental front, impedance spectroscopy is a sensitive and highly informative technique that can be used to both study and track even minor changes to Zn/Br system behavior contingent upon variations of chemical composition, physical arrangements and operating conditions.

Recommendations for future work based on findings from the work carried out and presented in preceding chapters of this thesis are categorized and discussed below:

8.2.1. Determining nature and proportion of electrolyte complexes

The work presented in Chapter 5 used the Raman spectroscopy technique to identify the type and relative proportion of the various zinc-halide complexes expected to be present in modern Zn/Br battery electrolytes at various simulated states of charge. However, a primary limitation of this technique was the inability to determine the exact concentrations of each species, including that of the hydrated zinc complex $[Zn(H_2O)_6]^{2+}$.

Additional techniques such as X-ray adsorption spectroscopy could be useful in determining these exact proportions of each of the various complexes existing within the electrolyte at different states of charge during battery operation. Further to this, it is beneficial to understand how these proportions and the type of complexes present are influenced by the presence of different types and concentrations of BSAs.

8.2.2. Improving supporting electrolyte formulation

The electrochemical and physical influence of supporting electrolytes has been studied at the zinc-side electrode in Chapter 4. As was subsequently shown and discussed in Chapter 7 for the case of ionic liquid additives, it is possible that supporting electrolytes which improved performance in the zinc half-cell could be detrimental to performance in the bromine half-cell and even the full-cell system. Consequently, it is necessary to continue development efforts involving those anions while concurrently assessing which anion-cation pairs offer the maximum benefit to system performance. By extension, it would be of great interest and potentially beneficial to pursue

investigations into the influence of organic additives commonly used during industrial zinc electroplating.

In addition to the electrolyte itself, the surface of the zinc-side electrode also plays a significant role in the tendency for zinc dendrites to form and propagate at the initial stages of charging. Consequently, it is important to identify and optimize electrolyte–electrode combinations which offer the highest benefit to both zinc and bromine half-cells and thus achieve optimal battery performance.

8.2.3. Optimizing the roles of bromine-sequestration agents

Some suitable alternative ionic liquid additives for improving zinc-side performance were identified in Chapter 5, while it was shown in Chapter 7 that similar benefits in the bromine half-cell are not guaranteed despite promising performance in the other side. Consequently, there is a balance to be struck in the use of ionic liquids which significantly improve system performance in one half-cell while having little or no negative influences in the other.

Following from that point, there also exist a number of hybrid BSA combinations remaining to be tested in both half-cells as well as the full-cell system. Additionally, while a 0.8–1 M BSA concentration is typically used in Zn/Br electrolyte formulations, this range may not necessarily apply for the case of either single-type or hybrid BSAs in future formulations. As discussed in Chapter 7, such investigations should be accompanied by investigations to understand the stability (both physical and electrochemical) and behavior (e.g. extent of miscibility with the aqueous electrolyte) of the bromine-sequestered complexes formed as cell charging progresses across a range of intended operating temperatures.

It is also necessary to develop a more sophisticated and comprehensive electrochemical model to describe processes in the zinc half-cell as EIS spectra suggest that electrochemical measurements at this electrode are influenced by additional factors and processes besides the zinc electrodeposition/stripping reaction.

8.2.4. Understanding interactions between electrolyte species

Molecular modelling, e.g. *via* DFT methods, has a very strong role to play in understanding the interactions between the various complexes and other electrolyte additives present in the Zn/Br environment. Such work could begin with further investigations into understanding the mechanics and subsequent reactions from the point of zinc removal from electrodeposited zinc on the zinc-side electrode surface due to the action of chlorides. These investigations could be expanded to study the effects of other supporting electrolytes, including those identified in Chapter 4 as potentially being beneficial, to understand how those ions interact with zinc and influence the surface, providing insights into the physical and electrochemical reactions at that electrode. Following from that point, DFT and molecular dynamics studies of how ionic liquid additives with different cationic structure and functional groups interact with zinc-covered and bare-carbon electrodes would be useful in improving understanding of how and why certain ionic liquids favorably influence reactions in the zinc half-cell.

8.3. Outlook for Zn/Br RFB Technology

In essence, future work in ZBB research should be focused on increasing detailed knowledge about the fundamental electrochemical and physical processes occurring within the system at each point of the charge/discharge cycle. With such knowledge it would be possible to design and implement tailor-made solutions to reduce or

circumvent some of the internal sources of electrochemical impedance that currently contribute towards inefficiency in the battery. These solutions include resolving the issue of non-uniformity of charge transfer across the surface of electrodes during both charging and discharging. By developing such tailor-made solutions, it may be possible to maximize the practical specific energy of the electrolyte through increased utilization of the ions in solution, thereby adding to the cost-effectiveness of the next generation of Zn/Br systems.

The use of sophisticated electrochemical techniques to identify the types and nature of dominant processes at a given point in time and three-dimensional space, both in the bulk electrolyte solution and especially at the EEI, is instrumental in designing alternative physical configurations and deciding the nature and degree of functionality required of future electrode materials. Focusing on the research and development of novel materials with superior functionality in the areas of electrolyte formulation, additives and "smarter" electrode surfaces, would lead to achieving a higher degree of control over processes at the EEI.

Ongoing research by the Energy Storage Group at the University of Sydney[256] includes investigations of alternative cell architectures and studies involving identification of beneficial electrolyte additives, as well as development and characterization of novel advanced electrode materials suitable for use in next-generation Zn/Br batteries. For widespread implementation of improved ZBBs to become a reality, it is necessary to give due consideration to trade-offs between battery performance and the costs and complexity of manufacturing. The next generation of enhanced-performance ZBBs is close to being developed, with renewed interest regarding commercialization and with reasonable potential for success in providing sustainable utility-scale electrical energy storage capability.

References

1. Yekini Suberu, M., Wazir Mustafa, M. & Bashir, N. Energy storage systems for renewable energy power sector integration and mitigation of intermittency. *Renew. Sustain. Energy Rev.* **35,** 499–514 (2014).

2. Goodson, A. How energy storage provides solutions to renewable integration challenges. in *Proceedings of the 2013 Electrical Energy Storage Applications & Technologies (EESAT) Biennial International Conference* (2013).

3. Boicea, V. A. Energy storage technologies: the past and the present. *Proc. IEEE* **102,** 1777–1794 (2014).

4. Luo, X., Wang, J., Dooner, M. & Clarke, J. Overview of current development in electrical energy storage technologies and the application potential in power system operation. *Appl. Energy* **137,** 511–536 (2014).

5. Zakeri, B. & Syri, S. Electrical energy storage systems: A comparative life cycle cost analysis. *Renew. Sustain. Energy Rev.* **42,** 569–596 (2015).

6. Spanos, C., Turney, D. E. & Fthenakis, V. Life-cycle analysis of flow-assisted nickel zinc-, manganese dioxide-, and valve-regulated lead-acid batteries designed for demand-charge reduction. *Renew. Sustain. Energy Rev.* **43,** 478–494 (2015).

7. Larcher, D. & Tarascon, J.-M. Towards greener and more sustainable batteries for electrical energy storage. *Nat. Chem.* **7,** 19–29 (2014).

8. Akinyele, D. O. & Rayudu, R. K. Review of energy storage technologies for sustainable power networks. *Sustain. Energy Technol. Assessments* **8,** 74–91 (2014).

9. Barnhart, C. J. The energetic implications of curtailing or storing wind and solar generated electricity. in *Proceedings of the 2013 Electrical Energy Storage Applications & Technologies (EESAT) Biennial International Conference* (2013).

10. Electricity Advisory Committee. *Bottling electricity: Storage as a strategic tool for managing variability and capacity concerns in the modern grid*. (2008).

11. Elsevier B.V. Journal of Power Sources. (2014). Available at: http://www.journals.elsevier.com/journal-of-power-sources.

12. Beaudin, M., Zareipour, H., Schellenberglabe, A. & Rosehart, W. Energy storage for mitigating the variability of renewable electricity sources: An

updated review. *Energy Sustain. Dev.* **14,** 302–314 (2010).

13.   Rose, D. M. & Ferreira, S. R. Performance Testing of Zinc-Bromine Flow Batteries for Remote Telecom Sites. in *The Battcon^{TM} 2013 Stationary Battery Conference and Trade Show* 1–11 (2013).

14.   Smith, S. C., Sen, P. K., Kroposki, B. & Malmedal, K. Renewable energy and energy storage systems in rural electrical power systems: Issues, challenges and application guidelines. in *2010 IEEE Rural Electric Power Conference (REPC)* B4-B4-7 (IEEE, 2010). doi:10.1109/REPCON.2010.5476206

15.   Dunn, B., Kamath, H. & Tarascon, J.-M. Electrical Energy Storage for the Grid: A Battery of Choices. *Science* **334,** 928–935 (2011).

16.   Parasuraman, A., Lim, T. M., Menictas, C. & Skyllas-Kazacos, M. Review of material research and development for vanadium redox flow battery applications. *Electrochim. Acta* **101,** 27–40 (2013).

17.   Cunha, Á., Martins, J., Rodrigues, N. & Brito, F. P. Vanadium redox flow batteries: a technology review. *Int. J. Energy Res.* n/a-n/a (2014). doi:10.1002/er.3260

18.   Braff, W. A., Bazant, M. Z. & Buie, C. R. Membrane-less hydrogen bromine flow battery. *Nat. Commun.* **4,** 1–6 (2013).

19.   Weber, A. Z. *et al.* Hydrogen/Bromine Flow Batteries. in *Proceedings of the 2013 Electrical Energy Storage Applications & Technologies (EESAT) Biennial International Conference* (2013).

20.   Bae, C., Roberts, E. P. L., Chakrabarti, M. H. & Saleem, M. All-Chromium Redox Flow Battery for Renewable Energy Storage. *Int. J. Green Energy* **8,** 248–264 (2011).

21.   Xing, X., Zhang, D. & Li, Y. A non-aqueous all-cobalt redox flow battery using 1,10-phenanthrolinecobalt(II) hexafluorophosphate as active species. *J. Power Sources* **279,** 205–209 (2015).

22.   Walsh, F. C. *et al.* The Development of Zn-Ce Hybrid Redox Flow Batteries for Energy Storage and Their Continuing Challenges. *Chempluschem* n/a-n/a (2014). doi:10.1002/cplu.201402103

23.   Leung, P. Development of a zinc-cerium redox flow battery. (University of Southampton, 2011).

24.   Leung, P. K., Ponce-de-León, C., Low, C. T. J., Shah, A. A. & Walsh, F. C. Characterization of a zinc–cerium flow battery. *J. Power Sources* **196,** 5174–

5185 (2011).

25. Xie, Z., Liu, Q., Chang, Z. & Zhang, X. The developments and challenges of cerium half-cell in zinc–cerium redox flow battery for energy storage. *Electrochim. Acta* **90,** 695–704 (2013).

26. Bhavaraju, S. Development of Sodium-Iodine Battery for Large-Scale Energy Storage. in *Proceedings of the 2013 Electrical Energy Storage Applications & Technologies (EESAT) Biennial International Conference* (2013).

27. Sanz, L. *et al.* Study and characterization of positive electrolytes for application in the aqueous all-copper redox flow battery. *J. Power Sources* **278,** 175–182 (2015).

28. Sanz, L., Lloyd, D., Magdalena, E., Palma, J. & Kontturi, K. Description and performance of a novel aqueous all-copper redox flow battery. *J. Power Sources* **268,** 121–128 (2014).

29. Lloyd, D., Magdalena, E., Sanz, L., Murtomäki, L. & Kontturi, K. Preparation of a cost-effective, scalable and energy efficient all-copper redox flow battery. *J. Power Sources* **292,** 87–94 (2015).

30. McKerracher, R. D., Ponce de Leon, C., Wills, R. G. a., Shah, a. a. & Walsh, F. C. A Review of the Iron-Air Secondary Battery for Energy Storage. *Chempluschem* n/a-n/a (2014). doi:10.1002/cplu.201402238

31. Li, B. *et al.* Ambipolar zinc-polyiodide electrolyte for a high-energy density aqueous redox flow battery. *Nat. Commun.* **6,** 6303 (2015).

32. Wu, M. *et al.* A novel high-energy-density positive electrolyte with multiple redox couples for redox flow batteries. *Appl. Energy* **136,** 576–581 (2014).

33. Oh, S. H. *et al.* A metal-free and all-organic redox flow battery with polythiophene as the electroactive species. *J. Mater. Chem. A* **2,** 19994–19998 (2014).

34. Chang, Z. *et al.* Rechargeable Li//Br battery: a promising platform for post lithium ion batteries. *J. Mater. Chem. A* **2,** 19444–19450 (2014).

35. Wang, W. *et al.* A new hybrid redox flow battery with multiple redox couples. *J. Power Sources* **216,** 99–103 (2012).

36. Huskinson, B. *et al.* A metal-free organic-inorganic aqueous flow battery. *Nature* **505,** 195–8 (2014).

37. Soloveichik, G. L. Electrochemistry: Metal-free energy storage. *Nature* **505,** 163–165 (2014).

38. Huskinson, B., Marshak, M. P., Gerhardt, M. R. & Aziz, M. J. Cycling of a Quinone-Bromide Flow Battery for Large-Scale Electrochemical Energy Storage. *ECS Trans.* **61,** 27–30 (2014).

39. Er, S., Suh, C., Marshak, M. P. & Aspuru-Guzik, A. Computational design of molecules for an all-quinone redox flow battery. *Chem. Sci.* (2014). doi:10.1039/C4SC03030C

40. Denholm, P. *et al.* Valuation of energy storage - quantification and ongoing policy challenges. in *Proceedings of the 2013 Electrical Energy Storage Applications & Technologies (EESAT) Biennial International Conference* (2013).

41. Putt, R. A. *Assessment of technical and economic feasibility of zinc/bromine batteries for utility load leveling. Final Report Gould, Inc., Rolling Meadows, IL.* (1979).

42. Exxon Research and Engineering Company. *Development of a Circulating Zinc-Bromine Battery, Phase I. Final Report*. (1983).

43. Exxon Research and Engineering Company. *Development of a Circulating Zinc-Bromine Battery, Phase II. Final Report*. (1983).

44. Exxon Research and Engineering Company. Zinc/Bromide Battery Development — Phase III. *J. Power Sources* **11,** 324–326 (1984).

45. Cathro, K. J. *Zinc-bromine batteries for energy storage applications: volume 541 of end of grant report*. (Department of Resources and Energy, 1986).

46. Bolstad, J. J. & Miles, R. C. Development of the zinc/bromine battery at Johnson Controls Inc. in *Proceedings of the 24th Intersociety Energy Conversion Engineering Conference* **3,** 1311–1318 (IEEE, 1989).

47. Lex, P. J. & Matthews, J. F. Recent developments in zinc/bromine battery technology at Johnson Controls. in *IEEE 35th International Power Sources Symposium* 88–92 (IEEE, 1992). doi:10.1109/IPSS.1992.282047

48. Bartolozzi, M. Development of redox flow batteries. A historical bibliography. *J. Power Sources* **27,** 219–234 (1989).

49. Butler, P., Eidler, P. & Grimes, P. in *Handbook of Batteries* (eds. Linden, D. & Reddy, T. B.) 37.1-37.16 (McGraw-Hill, 2001).

50. Linden, D. & Reddy, T. B. *Handbook of Batteries*. (McGraw-Hill Professional, 2001).

51. Weber, A. Z. *et al.* Redox flow batteries: A review. *Journal of Applied*

Electrochemistry **41,** 1137–1164 (2011).

52.   RedFlow Ltd. RedFlow Limited - Energy Storage Solutions. (2013). Available at: http://www.redflow.com.

53.   Premium Power Corp. Premium Power - Zinc-Flow(R) Technology. *Zinc-Flow(R) Technology* (2011). Available at: http://www.premiumpower.com.

54.   Primus Power. Primus Power. (2012). Available at: http://www.primuspower.com.

55.   Hall, J. High performance flowing electrolyte battery for grid scale energy storage. in *Proceedings of the 2013 Electrical Energy Storage Applications & Technologies (EESAT) Biennial International Conference* (2013).

56.   ZBB Energy Corp. ZBB Energy ∷ Zn-Br Flow Battery Technology. (2014). Available at: http://www.zbbenergy.com.

57.   Ponce de Leon, C. & Walsh, F. C. in *Encyclopedia of Electrochemical Power Sources* (eds. Dyer, C. et al.) 487–496 (Elsevier, 2009). doi:10.1016/B978-044452745-5.00856-X

58.   Beck, F. & Rüetschi, P. Rechargeable batteries with aqueous electrolytes. *Electrochimica Acta* **45,** 2467–2482 (2000).

59.   U.S. Geological Survey. *Mineral Commodity Summaries 2011*. (2011).

60.   The London Metal Exchange. Settlement prices. (2014). Available at: http://www.lme.com/.

61.   Bureau of Labor Statistics (U.S. Department of Labor). Inflation Calculator: Bureau of Labor Statistics. *CPI Inflation Calculator* (2014). Available at: http://www.bls.gov/data/inflation_calculator.htm.

62.   Bradbury, K., Pratson, L. & Patiño-Echeverri, D. Economic viability of energy storage systems based on price arbitrage potential in real-time U.S. electricity markets. *Appl. Energy* **114,** 512–519 (2014).

63.   Aburub, H., Jewell, W. T. & Price, J. E. Assessment of the use of CAISO wholesale grid state indicator to schedule storage. in *2013 North American Power Symposium (NAPS)* 1–6 (IEEE, 2013). doi:10.1109/NAPS.2013.6666897

64.   Nykvist, B. & Nilsson, M. Rapidly falling costs of battery packs for electric vehicles. *Nat. Clim. Chang.* **5,** 329–332 (2015).

65.   Parry, R. From Concept to Commercialization - China as a Design and Engineering Base for Low Cost Flow Battery Products. in *Proceedings of the*

2013 Electrical Energy Storage Applications & Technologies (EESAT) Biennial International Conference (2013).

66. Montoya, T. L. *et al. Flow Battery System Design for Manufacturability*. (2014).

67. Mastragostino, M. & Valcher, S. Polymeric salt as bromine complexing agent in a Zn-Br2 model battery. *Electrochim. Acta* **28,** 501–505 (1983).

68. Poon, G., Parasuraman, A., Lim, T. M. & Skyllas-Kazacos, M. Evaluation of N-ethyl-N-methyl-morpholinium bromide and N-ethyl-N-methyl-pyrrolidinium bromide as bromine complexing agents in vanadium bromide redox flow batteries. *Electrochim. Acta* **107,** 388–396 (2013).

69. Cathro, K. J., Cedzynska, K. & Constable, D. C. Some properties of zinc/bromine battery electrolytes. *J. Power Sources* **16,** 53–63 (1985).

70. Chalamala, B. R. *et al.* Redox Flow Batteries: An Engineering Perspective. *Proc. IEEE* **102,** 976–999 (2014).

71. Moro, L. M. S. Trends in redox flow battery technology and project REDOX2015. in *2013 International Conference on New Concepts in Smart Cities: Fostering Public and Private Alliances (SmartMILE)* 1–4 (IEEE, 2013). doi:10.1109/SmartMILE.2013.6708218

72. Wang, W. *et al.* Recent Progress in Redox Flow Battery Research and Development. *Adv. Funct. Mater.* **23,** 970–986 (2013).

73. Ponce de León, C., Frías-Ferrer, A., González-García, J., Szánto, D. A. & Walsh, F. C. Redox flow cells for energy conversion. *J. Power Sources* **160,** 716–732 (2006).

74. Skyllas-Kazacos, M., Chakrabarti, M. H., Hajimolana, S. A., Mjalli, F. S. & Saleem, M. Progress in Flow Battery Research and Development. *Journal of The Electrochemical Society* **158,** R55 (2011).

75. Palacín, M. R. Recent advances in rechargeable battery materials: a chemist's perspective. *Chem. Soc. Rev.* **38,** 2565–75 (2009).

76. Kear, G., Shah, A. A. & Walsh, F. C. Development of the all-vanadium redox flow battery for energy storage: a review of technological, financial and policy aspects. *Int. J. Energy Res.* **36,** 1105–1120 (2012).

77. Skyllas-Kazacos, M., Kazacos, G., Poon, G. & Verseema, H. Recent advances with UNSW vanadium-based redox flow batteries. *Int. J. Energy Res.* **34,** 182–189 (2010).

78. Huang, K.-L., Li, X., Liu, S., Tan, N. & Chen, L. Research progress of vanadium redox flow battery for energy storage in China. *Renew. Energy* **33,** 186–192 (2008).

79. Rajarathnam, G. P. & Vassallo, A. M. *The Zinc/Bromine Flow Battery: Materials Challenges and Practical Solutions for Technology Advancement.* (Springer Singapore, 2016). doi:10.1007/978-981-287-646-1

80. Cedzynska, K. Properties of modified electrolyte for zinc-bromine cells. *Electrochim. Acta* **40,** 971–976 (1995).

81. Cathro, K. J., Cedzynska, K., Constable, D. C. & Hoobin, P. M. Selection of quaternary ammonium bromides for use in zinc/bromine cells. *J. Power Sources* **18,** 349–370 (1986).

82. Cathro, K. J. Performance of zinc/bromine cells having a propionitrile electrolyte. *J. Power Sources* **23,** 365–383 (1988).

83. Singh, P. Application of non-aqueous solvents to batteries. *J. Power Sources* **11,** 135–142 (1984).

84. Singh, P., White, K. & Parker, A. J. Application of non-aqueous solvents to batteries part I. Physicochemical properties of propionitrile/water two-phase solvent relevant to zinc—bromine. *J. Power Sources* **10,** 309–318 (1983).

85. Lancry, E., Magnes, B.-Z., Ben-David, I. & Freiberg, M. New Bromine Complexing Agents for Bromide Based Batteries. *ECS Trans.* **53,** 107–115 (2013).

86. Blöchl, P. E. Projector augmented-wave method. *Phys. Rev. B* **50,** 17953–17979 (1994).

87. Kresse, G. From ultrasoft pseudopotentials to the projector augmented-wave method. *Phys. Rev. B* **59,** 1758–1775 (1999).

88. Kresse, G. & Furthmüller, J. Efficient iterative schemes for ab initio total-energy calculations using a plane-wave basis set. *Phys. Rev. B. Condens. Matter* **54,** 11169–11186 (1996).

89. Clark, N., Eidler, P. & Lex, P. *Development of Zinc/Bromine Batteries for Load-Leveling Applications: Phase 2 Final Report (Sandia Report SAND99-2691).* (1999).

90. Baik, D. S. & Fray, D. J. Electrodeposition of zinc from high acid zinc chloride solutions. *J. Appl. Electrochem.* **31,** 1141–1147 (2001).

91. Haller, H. & Riedel, S. Recent discoveries of polyhalogen anions - from

bromine to fluorine. *Zeitschrift für Anorg. und Allg. Chemie* **640,** 1281–1291 (2014).

92. Mader, M. J. A Mathematical Model of a Zn∕Br2 Cell on Charge. *J. Electrochem. Soc.* **133,** 1297 (1986).

93. Rajarathnam, G. P. & Vassallo, A. M. in *The Zinc/Bromine Flow Battery: Materials Challenges and Practical Solutions for Technology Advancement* 29–43 (Springer Singapore, 2016). doi:10.1007/978-981-287-646-1_3

94. Rajarathnam, G. P. & Vassallo, A. M. in *The Zinc/Bromine Flow Battery: Materials Challenges and Practical Solutions for Technology Advancement* 45–62 (Springer Singapore, 2016). doi:10.1007/978-981-287-646-1_4

95. Rajarathnam, G. P. & Vassallo, A. M. in *The Zinc/Bromine Flow Battery: Materials Challenges and Practical Solutions for Technology Advancement* 63–79 (Springer Singapore, 2016). doi:10.1007/978-981-287-646-1_5

96. Sigma-Aldrich. *Material Safety Data Sheet - Bromine*. (2014).

97. Yang, S.-C. An approximate model for estimating the faradaic efficiency loss in zinc/bromine batteries caused by cell self-discharge. *J. Power Sources* **50,** 343–360 (1994).

98. Chiu, S. L. & Selman, J. R. Determination of electrode kinetics by corrosion potential measurements: Zinc corrosion by bromine. *J. Appl. Electrochem.* **22,** 28–37 (1992).

99. Lim, H. S. Zinc-bromine secondary battery. *J. Electrochem. Soc.* **124,** 1154–1157 (1977).

100. Heintz, A. & Illenberger, C. Diffusion coefficients of Br2 in cation exchange membranes. *J. Memb. Sci.* **113,** 175–181 (1996).

101. Gregor, H. P. Ion-exchange membranes - Correlation between structure and function. *Pure Appl. Chem.* **16,** 329–350 (1968).

102. Cathro, K. J., Constable, D. C. & Hoobin, P. M. Performance of porous plastic separators in zinc/bromine cells. *J. Power Sources* **22,** 29–57 (1988).

103. Bellows, R. J. *et al.* Zinc-bromine battery design for electric vehicles. *IEEE Trans. Veh. Technol.* **32,** 26–32 (1983).

104. Eidler, P. *Development of Zinc/Bromine Batteries for Load-Leveling Applications: Phase 1 Final Report (Sandia Report SAND99-1853).* (1999).

105. Will, F. G. Recent advances in zinc-bromine batteries. in *Proceedings of the Eleventh International Symposium, September 25-28, 1978* 313–326 (Academic

Press, Inc. (London), Ltd., 1979).

106. Maurya, S., Shin, S.-H., Kim, Y. & Moon, S.-H. A review on recent developments of anion exchange membranes for fuel cells and redox flow batteries. *RSC Adv.* **5,** 37206–37230 (2015).

107. Gu, S., Gong, K., Yan, E. Z. & Yan, Y. A multiple ion-exchange membrane design for redox flow batteries. *Energy Environ. Sci.* **7,** 2986 (2014).

108. Arnold, C. & Assink, R. A. Development of sulfonated polysulfone membranes for redox flow batteries. *J. Memb. Sci.* **38,** 71–83 (1988).

109. Hinkle, K. R., Jameson, C. J. & Murad, S. Transport of Vanadium and Oxovanadium Ions Across Zeolite Membranes: A Molecular Dynamics Study. *J. Phys. Chem. C* **118,** 23803–23810 (2014).

110. Xiangguo, T., Jicui, D. & Jing, S. Effects of different kinds of surfactants on Nafion membranes for all vanadium redox flow battery. *J. Solid State Electrochem.* (2014). doi:10.1007/s10008-014-2713-7

111. Winardi, S. *et al.* Effect of Bromine Complexing Agents on the Performance of Cation Exchange Membranes in Second-Generation Vanadium Bromide Battery. *Chempluschem* **80,** 376–381 (2015).

112. Lee, K. J. & Chu, Y. H. Preparation of the graphene oxide (GO)/Nafion composite membrane for the vanadium redox flow battery (VRB) system. *Vacuum* **107,** 269–276 (2014).

113. Pop, V., Bergveld, H. J., Danilov, D., Regtien, P. P. L. & Notten, P. H. L. *Battery Management Systems: Accurate State-of-Charge Indication for Battery-Powered Applications (Volume 9 of Philips research book series).* (Springer Science+Business Media B.V., 2008).

114. Piller, S., Perrin, M. & Jossen, A. Methods for state-of-charge determination and their applications. *J. Power Sources* **96,** 113–120 (2001).

115. Pang, S., Farrell, J., Du, J. & Barth, M. Battery state-of-charge estimation. in *Proceedings of the 2001 American Control Conference. (Cat. No.01CH37148)* **2,** 1644–1649 (IEEE, 2001).

116. Ng, K. S., Moo, C.-S., Chen, Y.-P. & Hsieh, Y.-C. Enhanced coulomb counting method for estimating state-of-charge and state-of-health of lithium-ion batteries. *Appl. Energy* **86,** 1506–1511 (2009).

117. Lukic, S. M., Bansal, R. C., Rodriguez, F. & Emadi, A. Energy Storage Systems for Automotive Applications. *IEEE Trans. Ind. Electron.* **55,** 2258–2267

(2008).

118. Bhangu, B. S., Bentley, P., Stone, D. A. & Bingham, C. M. Nonlinear Observers for Predicting State-of-Charge and State-of-Health of Lead-Acid Batteries for Hybrid-Electric Vehicles. *IEEE Trans. Veh. Technol.* **54,** 783–794 (2005).

119. Vasebi, A., Partovibakhsh, M. & Bathaee, S. M. T. A novel combined battery model for state-of-charge estimation in lead-acid batteries based on extended Kalman filter for hybrid electric vehicle applications. *J. Power Sources* **174,** 30–40 (2007).

120. Vasebi, A., Bathaee, S. M. T. & Partovibakhsh, M. Predicting state of charge of lead-acid batteries for hybrid electric vehicles by extended Kalman filter. *Energy Convers. Manag.* **49,** 75–82 (2008).

121. Santhanagopalan, S. & White, R. E. Online estimation of the state of charge of a lithium ion cell. *J. Power Sources* **161,** 1346–1355 (2006).

122. Plett, G. L. Extended Kalman filtering for battery management systems of LiPB-based HEV battery packs. *J. Power Sources* **134,** 277–292 (2004).

123. Lee, S., Kim, J., Lee, J. & Cho, B. H. State-of-charge and capacity estimation of lithium-ion battery using a new open-circuit voltage versus state-of-charge. *J. Power Sources* **185,** 1367–1373 (2008).

124. Skyllas-Kazacos, M. & Kazacos, M. State of charge monitoring methods for vanadium redox flow battery control. *J. Power Sources* **196,** 8822–8827 (2011).

125. Rodrigues, S., Munichandraiah, N. & Shukla, A. K. A review of state-of-charge indication of batteries by means of a.c. impedance measurements. *J. Power Sources* **87,** 12–20 (2000).

126. Huet, F. A review of impedance measurements for determination of the state-of-charge or state-of-health of secondary batteries. *J. Power Sources* **70,** 59–69 (1998).

127. Thele, M., Bohlen, O., Sauer, D. U. & Karden, E. Development of a voltage-behavior model for NiMH batteries using an impedance-based modeling concept. *J. Power Sources* **175,** 635–643 (2008).

128. Sabatier, J. *et al.* Fractional system identification for lead acid battery state of charge estimation. *Signal Processing* **86,** 2645–2657 (2006).

129. Takano, K., Nozaki, K., Saito, Y., Kato, K. & Negishi, A. Impedance Spectroscopy by Voltage-Step Chronoamperometry Using the Laplace Transform Method in a Lithium-Ion Battery. *J. Electrochem. Soc.* **147,** 922–929

(2000).

130. Delaille, A., Perrin, M., Huet, F. & Hernout, L. Study of the 'coup de fouet' of lead-acid cells as a function of their state-of-charge and state-of-health. *J. Power Sources* **158,** 1019–1028 (2006).

131. Verbrugge, M. & Tate, E. Adaptive state of charge algorithm for nickel metal hydride batteries including hysteresis phenomena. *J. Power Sources* **126,** 236–249 (2004).

132. Rong, P. & Pedram, M. An analytical model for predicting the remaining battery capacity of lithium-ion batteries. *IEEE Trans. Very Large Scale Integr. Syst.* **14,** 441–451 (2006).

133. Shen, Y. Adaptive online state-of-charge determination based on neuro-controller and neural network. *Energy Convers. Manag.* **51,** 1093–1098 (2010).

134. Cai, C., Du, D., Liu, Z. & Ge, J. State-of-charge (SOC) estimation of high power Ni-MH rechargeable battery with artificial neural network. in *Proceedings of the 9th International Conference on Neural Information Processing, 2002. ICONIP '02.* **2,** 824–828 (Nanyang Technol. Univ, 2002).

135. Grewal, S. & Grant, D. A. A novel technique for modelling the state of charge of lithium ion batteries using artificial neural networks. in *Twenty-Third International Telecommunications Energy Conference. INTELEC 2001* **2001,** 174–179 (IEE, 2001).

136. Singh, P., Vinjamuri, R., Wang, X. & Reisner, D. Design and implementation of a fuzzy logic-based state-of-charge meter for Li-ion batteries used in portable defibrillators. *J. Power Sources* **162,** 829–836 (2006).

137. Salkind, A. J., Fennie, C., Singh, P., Atwater, T. & Reisner, D. E. Determination of state-of-charge and state-of-health of batteries by fuzzy logic methodology. *J. Power Sources* **80,** 293–300 (1999).

138. Lee, D.-T., Shiah, S.-J., Lee, C.-M. & Wang, Y.-C. State-of-Charge Estimation for Electric Scooters by Using Learning Mechanisms. *IEEE Trans. Veh. Technol.* **56,** 544–556 (2007).

139. Cai, C. H., Du, D. & Liu, Z. Y. Battery state-of-charge (SOC) estimation using adaptive neuro-fuzzy inference system (ANFIS). in *The 12th IEEE International Conference on Fuzzy Systems, 2003. FUZZ '03.* **2,** 1068–1073 (IEEE, 2003).

140. Lee, Y., Wang, W. & Kuo, T. Soft Computing for Battery State-of-Charge

(BSOC) Estimation in Battery String Systems. *IEEE Trans. Ind. Electron.* **55,** 229–239 (2008).

141. Kim, I. Nonlinear State of Charge Estimator for Hybrid Electric Vehicle Battery. *IEEE Trans. Power Electron.* **23,** 2027–2034 (2008).

142. Viswanathan, V. V., Salkind, A. J., Kelley, J. J. & Ockerman, J. B. Effect of state of charge on impedance spectrum of sealed cells Part II: Lead acid batteries. *J. Appl. Electrochem.* **25,** 729–739 (1995).

143. Gopikanth, M. L. & Sathyanarayana, S. Impedance parameters and the state-of-charge. II. Lead-acid battery. *J. Appl. Electrochem.* **9,** 369–379 (1979).

144. Hammouche, A., Karden, E. & De Doncker, R. W. Monitoring state-of-charge of Ni–MH and Ni–Cd batteries using impedance spectroscopy. *J. Power Sources* **127,** 105–111 (2004).

145. Blanke, H. *et al.* Impedance measurements on lead–acid batteries for state-of-charge, state-of-health and cranking capability prognosis in electric and hybrid electric vehicles. *J. Power Sources* **144,** 418–425 (2005).

146. Singh, P., Fennie, C., Reisner, D. E. & Salkind, A. Fuzzy Logic Enhanced Electrochemical Impedance Spectroscopy (FLEEIS) to Determine Battery State-of-Charge. in *Proceedings of the 15th Annual Battery Conference on Applications and Advances (January 11-14, 2000)* 199–204 (2000).

147. Arenas, L. F., Walsh, F. C. & de Leon, C. P. 3D-Printing of Redox Flow Batteries for Energy Storage: A Rapid Prototype Laboratory Cell. *ECS J. Solid State Sci. Technol.* **4,** P3080–P3085 (2015).

148. Peng, M. *et al.* Efficient fiber shaped zinc bromide batteries and dye sensitized solar cells for flexible power sources. *J. Mater. Chem. C* **3,** 2157–2165 (2015).

149. Desai, D., Wei, X., Steingart, D. A. & Banerjee, S. Electrodeposition of preferentially oriented zinc for flow-assisted alkaline batteries. *J. Power Sources* **256,** 145–152 (2014).

150. Jorné, J., Kim, J. T. & Kralik, D. The zinc-chlorine battery: half-cell overpotential measurements. *J. Appl. Electrochem.* **9,** 573–579 (1979).

151. Bard, A. J. & Faulkner, L. R. *Electrochemical Methods: Fundamentals and Applications*. (John Wiley & Sons, Inc., 2001).

152. Neufeld, A. K., Cole, I. S., Bond, A. M. & Furman, S. A. The initiation mechanism of corrosion of zinc by sodium chloride particle deposition. *Corros. Sci.* **44,** 555–572 (2002).

153. Thomas, B. K. & Fray, D. J. Leaching of zinc and zinc alloys with chlorine and chlorine hydrate. *Metall. Trans. B* **12,** 559–563 (1981).

154. Kim, J. T. The Kinetics and Mass Transfer of Zinc Electrode in Acidic Zinc-Chloride Solution. *J. Electrochem. Soc.* **127,** 8–15 (1980).

155. Mackinnon, D. J., Brannen, J. M. & Lakshmanan, V. I. The effects of chloride ion and organic extradants on electrowon zinc deposits. *J. Appl. Electrochem.* **10,** 321–334 (1980).

156. Rajarathnam, G. P., Schneider, M., Sun, X. & Vassallo, A. M. The Influence of Supporting Electrolytes on Zinc Half-Cell Performance in Zinc/Bromine Flow Batteries. *J. Electrochem. Soc.* **163,** A5112–A5117 (2016).

157. Kim, D. & Jeon, J. Study on Durability and Stability of an Aqueous Electrolyte Solution for Zinc Bromide Hybrid Flow Batteries. *J. Phys. Conf. Ser.* **574,** 12074 (2015).

158. Abbott, A. P., Barron, J. C., Frisch, G., Ryder, K. S. & Silva, A. F. The effect of additives on zinc electrodeposition from deep eutectic solvents. *Electrochim. Acta* **56,** 5272–5279 (2011).

159. Ganne, F. *et al.* Impedance spectroscopy and modelling of zinc deposition in chloride electrolyte containing a commercial additive. *J. Appl. Electrochem.* **30,** 665–673 (2000).

160. McBreen, J. Electrodeposition of Zinc on Glassy Carbon from ZnCl2 and ZnBr2 Electrolytes. *J. Electrochem. Soc.* **130,** 1667–1670 (1983).

161. Jugović, B. Z., Trišović, T. L., Stevanović, J. S., Maksimović, M. D. & Grgur, B. N. Comparative studies of chloride and chloride/citrate based electrolytes for zinc-polyaniline batteries. *Electrochim. Acta* **51,** 6268–6274 (2006).

162. Iokibe, K., Azumi, K. & Tachikawa, H. Surface Diffusion of a Zn Adatom on a Zn(001) Surface: A DFT Study. *J. Phys. Chem. C* **111,** 13510–13516 (2007).

163. Siahrostami, S. *et al.* First principles investigation of zinc-anode dissolution in zinc-air batteries. *Phys. Chem. Chem. Phys.* **15,** 6416–21 (2013).

164. Şahin, H. & Ciraci, S. Chlorine Adsorption on Graphene: Chlorographene. *J. Phys. Chem. C* **116,** 24075–24083 (2012).

165. Gao, W. *et al.* Chlorine adsorption on Au(111): Chlorine overlayer or surface chloride? *J. Am. Chem. Soc.* **130,** 3560–3565 (2008).

166. Zheleva, Z. V., Dhanak, V. R. & Held, G. Experimental structure determination of the chemisorbed overlayers of chlorine and iodine on Au{111}. *Phys. Chem.*

Chem. Phys. **12,** 10754 (2010).

167. Peljhan, S. & Kokalj, A. Adsorption of Chlorine on Cu(111): A Density-Functional Theory Study. *J. Phys. Chem. C* **113,** 14363–14376 (2009).

168. Pašti, I. A. & Mentus, S. V. Halogen adsorption on crystallographic (111) planes of Pt, Pd, Cu and Au, and on Pd-monolayer catalyst surfaces: First-principles study. *Electrochim. Acta* **55,** 1995–2003 (2010).

169. Liu, M., Jin, Y., Zhang, C., Leygraf, C. & Wen, L. Density-functional theory investigation of Al pitting corrosion in electrolyte containing chloride ions. *Appl. Surf. Sci.* **357,** 2028–2038 (2015).

170. Williamson, G. . & Hall, W. . X-ray line broadening from filed aluminium and wolfram. *Acta Metall.* **1,** 22–31 (1953).

171. Khorsand Zak, A., Abd. Majid, W. H., Abrishami, M. E. & Yousefi, R. X-ray analysis of ZnO nanoparticles by Williamson–Hall and size–strain plot methods. *Solid State Sci.* **13,** 251–256 (2011).

172. Materials Design Inc. MedeA. (2016).

173. Perdew, J. P., Burke, K. & Ernzerhof, M. Generalized Gradient Approximation Made Simple. *Phys. Rev. Lett.* **77,** 3865–3868 (1996).

174. Methfessel, M. & Paxton, A. High-precision sampling for Brillouin-zone integration in metals. *Phys. Rev. B* **40,** 3616–3621 (1989).

175. Henkelman, G., Uberuaga, B. P. & Jónsson, H. A climbing image nudged elastic band method for finding saddle points and minimum energy paths. *J. Chem. Phys.* **113,** 9901 (2000).

176. Almora-Barrios, N., Novell-Leruth, G., Whiting, P., Liz-Marzán, L. M. & López, N. Theoretical description of the role of halides, silver, and surfactants on the structure of gold nanorods. *Nano Lett.* **14,** 871–5 (2014).

177. Kairys, V. & Head, J. D. Quantum chemical cluster study of hydrated halide adsorption on the cathodic Al(111) surface. *Surf. Sci.* **440,** 169–186 (1999).

178. Mathew, K., Sundararaman, R., Letchworth-Weaver, K., Arias, T. A. & Hennig, R. G. Implicit solvation model for density-functional study of nanocrystal surfaces and reaction pathways. *J. Chem. Phys.* **140,** 84106 (2014).

179. Koper, M. T. . & van Santen, R. A. Interaction of halogens with Hg, Ag and Pt surfaces: a density functional study. *Surf. Sci.* **422,** 118–131 (1999).

180. Jungwirth, P. & Tobias, D. J. Chloride Anion on Aqueous Clusters, at the Air−Water Interface, and in Liquid Water: Solvent Effects on Cl -

Polarizability. *J. Phys. Chem. A* **106,** 379–383 (2002).

181. Uematsu, M. & Frank, E. U. Static Dielectric Constant of Water and Steam. *J. Phys. Chem. Ref. Data* **9,** 1291 (1980).

182. Suresh, S. *et al.* Zinc–bromine hybrid flow battery: effect of zinc utilization and performance characteristics. *RSC Adv.* **4,** 37947 (2014).

183. Balzar, D. Profile fitting of X-ray diffraction lines and Fourier analysis of broadening. *J. Appl. Crystallogr.* **25,** 559–570 (1992).

184. Thrower, P. A. & Nagle, D. C. The importance of strain in crystallite size determinations in graphite. *Carbon N. Y.* **11,** 663–664 (1973).

185. Delhez, R., Keijser, T. H. de & Mittemeijer, E. J. The X-ray diffraction line broadening due to the diffractometer condition as a function of 2θ. *J. Phys. E.* **11,** 649–652 (1978).

186. Momma, K. & Izumi, F. VESTA 3 for three-dimensional visualization of crystal, volumetric and morphology data. *J. Appl. Crystallogr.* **44,** 1272–1276 (2011).

187. Darwent, B. deB. *National Standard Reference Data Series No. 31: Bond Dissociation Energies in Simple Molecules*. (1970).

188. Pauling, L. The Nature Of The Chemical Bond. IV. The Energy Of Single Bonds And The Relative Electronegativity Of Atoms. *J. Am. Chem. Soc.* **54,** 3570–3582 (1932).

189. Pavlova, T. V., Andryushechkin, B. V. & Zhidomirov, G. M. First-Principle Study of Adsorption and Desorption of Chlorine on Cu(111) Surface: Does Chlorine or Copper Chloride Desorb? *J. Phys. Chem. C* **120,** 2829–2836 (2016).

190. Bohinc, K., Kralj-Iglič, V. & Iglič, A. Thickness of electrical double layer. Effect of ion size. *Electrochim. Acta* **46,** 3033–3040 (2001).

191. Abd El Rehim, S. S., Abd El Wahaab, S. M., Fouad, E. E. & Hassan, H. H. Effect of some variables on the electroplating of zinc from acidic acetate baths. *J. Appl. Electrochem.* **24,** 350–354 (1994).

192. Sun, X., Souier, T., Chiesa, M. & Vassallo, A. Effect of surface transport properties on the performance of carbon plastic electrodes for flow battery applications. *Electrochim. Acta* **148,** 104–110 (2014).

193. Mackinnon, D. J., Brannen, J. M. & Lakshmanan, V. I. Zinc deposit structures obtained from synthetic zinc chloride electrolyte. *J. Appl. Electrochem.* **9,** 603–613 (1979).

194. Youssef, K. M. S., Koch, C. C. & Fedkiw, P. S. Influence of Additives and Pulse Electrodeposition Parameters on Production of Nanocrystalline Zinc from Zinc Chloride Electrolytes. *J. Electrochem. Soc.* **151,** C103–C111 (2004).

195. Trejo, G. *et al.* Nucleation and Growth of Zinc from Chloride Concentrated Solutions. *J. Electrochem. Soc.* **145,** 4090 (1998).

196. Cachet, C. *et al.* EIS investigation of zinc dissolution in aerated sulfate medium. Part I: bulk zinc. *Electrochim. Acta* **47,** 509–518 (2001).

197. Cachet, C. *et al.* EIS investigation of zinc dissolution in aerated sulphate medium. Part II: zinc coatings. *Electrochim. Acta* **47,** 3409–3422 (2002).

198. Mackinnon, D. J. & Brannen, J. M. Zinc deposit structures obtained from high purity synthetic and industrial acid sulphate electrolytes with and without antimony and glue additions. *J. Appl. Electrochem.* **7,** 451–459 (1977).

199. Alfantazi, A. M. & Dreisinger, D. B. An investigation on the effects of orthophenylene diamine and sodium lignin sulfonate on zinc electrowinning from industrial electrolyte. *Hydrometallurgy* **69,** 99–107 (2003).

200. Saba, A. E. & Elsherief, A. E. Continuous electrowinning of zinc. *Hydrometallurgy* **54,** 91–106 (2000).

201. Lockett, V., Sedev, R., Ralston, J., Horne, M. & Rodopoulos, T. Differential capacitance of the electrical double layer in imidazolium-based ionic liquids: Influence of potential, cation size, and temperature. *J. Phys. Chem. C* **112,** 7486–7495 (2008).

202. Grier, D. G., Allen, K., Goldman, R. S., Sander, L. M. & Clarke, R. Superlattices and long-range order in electrodeposited dendrites. *Phys. Rev. Lett.* **64,** 2152–2155 (1990).

203. Cachet, C. & Wiart, R. Zinc deposition and passivated hydrogen evolution in highly acidic sulphate electrolytes: Depassivation by nickel impurities. *J. Appl. Electrochem.* **20,** 1009–1014 (1990).

204. Rajarathnam, G. P. *et al.* The influence of ionic liquid additives on zinc half-cell electrochemical performance in zinc/bromine flow batteries. *RSC Adv.* **6,** 27788–27797 (2016).

205. Morris, D. F. C., Short, E. L. & Waters, D. N. Zinc chloride and zinc bromide complexes—III. *J. Inorg. Nucl. Chem.* **25,** 975–983 (1963).

206. Quicksall, C. O. & Spiro, T. G. Raman Spectra of Tetrahalozincates and the Structure of Aqueous ZnCl 4 2. *Inorg. Chem.* **5,** 2232–2233 (1966).

207. Dreier, P. & Rabe, P. EXAFS-STUDY OF THE Zn 2+ COORDINATION IN AQUEOUS HALIDE SOLUTIONS. *Le J. Phys. Colloq.* **47,** C8-809-C8-812 (1986).

208. Irish, D. E., McCarroll, B. & Young, T. F. Raman Study of Zinc Chloride Solutions. *J. Chem. Phys.* **39,** 3436 (1963).

209. Heumen, J. Van, Ozeki, T. & Irish, D. E. A Raman spectral study of the equilibria of zinc bromide complexes in DMSO solutions. *Can. J. Chem.* **67,** 2030–2036 (1989).

210. Abe, Y. & Ishiguro, S. Thermodynamics of complexation of zinc(II) with chloride, bromide and iodide ions in hexamethylphosphoric triamide. *J. Solution Chem.* **20,** 793–803 (1991).

211. Kanno, H. & Yamauchi, S. Raman spectral changes of alcoholic zinc chloride solutions from liquid state to glassy state. *J. Solution Chem.* **20,** 589–594 (1991).

212. Kanno, H. & Hiraishi, J. Raman spectroscopic study of glassy aqueous zinc halide solutions. *J. Raman Spectrosc.* **9,** 85–89 (1980).

213. Takamuku, T., Yoshikai, K., Yamaguchi, T. & Wakita, H. Structure of Supercooled Aqueous Zinc(II) Bromide Solutions by Raman and X-Ray Scattering Methods. *Zeitschrift für Naturforsch. A* **47,** 841–848 (1992).

214. Macklin, J. W. & Plane, R. A. Raman study of stepwise formation of bromide complexes of zinc, cadmium, and mercury in aqueous solution. *Inorg. Chem.* **9,** 821–827 (1970).

215. Takamuku, T., Ihara, M., Yamaguchi, T. & Wakita, H. Raman Spectroscopic and X-ray Diffraction Studies on Concentrated Aqueous Zinc (II) Bromide Solution at High Temperatures. *Zeitschrift für Naturforsch. A* **47,** 485–492 (1992).

216. Marley, N. A. & Gaffney, J. S. Laser Raman Spectral Determination of Zinc Halide Complexes in Aqueous Solutions as a Function of Temperature and Pressure. *Appl. Spectrosc.* **44,** 469–476 (1990).

217. Liu, W., Borg, S., Etschmann, B., Mei, Y. & Brugger, J. An XAS study of speciation and thermodynamic properties of aqueous zinc bromide complexes at 25–150°C. *Chem. Geol.* **298–299,** 57–69 (2012).

218. Mibe, K., Chou, I.-M., Anderson, A. J., Mayanovic, R. a. & Bassett, W. a. The speciation of aqueous zinc(II) bromide solutions to 500 °C and 900 MPa

determined using Raman spectroscopy. *Chem. Geol.* **259,** 48–53 (2009).

219. Yang, M. M., Crerar, D. A. & Irish, D. E. Raman spectral studies of aqueous zinc bromide solutions to 300C at pressures of 9 MPa. *J. Solution Chem.* **17,** 751–762 (1988).

220. Powell, D., Gullidge, P. & Neilson, G. Zn 2+ hydration and complexation in aqueous electrolyte solutions. *Mol. Phys.* **71,** 1107–1116 (1990).

221. Bock, C. W., Markham, G. D., Katz, A. K. & Glusker, J. P. The arrangement of first- and second-shell water molecules around metal ions: Effects of charge and size. *Theor. Chem. Acc.* **115,** 100–112 (2006).

222. Harris, D. J., Brodholt, J. P., Harding, J. H. & Sherman, D. M. Molecular Dynamics simulation of aqueous ZnCl2 solutions. *Mol. Phys.* **99,** 825–833 (2001).

223. Bauer, G., Drobits, J., Fabjan, C., Mikosch, H. & Schuster, P. Raman spectroscopic study of the bromine storing complex phase in a zinc-flow battery. *J. Electroanal. Chem.* **427,** 123–128 (1997).

224. Pell, W. Zinc/bromine battery electrolytes: Electrochemical, physicochemical and spectroscopic studies. (University of Ottawa, 1995).

225. Asthagiri, D., Pratt, L. R., Paulaitis, M. E. & Rempe, S. B. Hydration Structure and Free Energy of Biomolecularly Specific Aqueous Dications, Including Zn 2+ and First Transition Row Metals. *J. Am. Chem. Soc.* **126,** 1285–1289 (2004).

226. Trachtman, M., Markham, G. D., Glusker, J. P., George, P. & Bock, C. W. Interactions of Metal Ions with Water: Ab Initio Molecular Orbital Studies of Structure, Bonding Enthalpies, Vibrational Frequencies and Charge Distributions. 1. Monohydrates. *Inorg. Chem.* **37,** 4421–4431 (1998).

227. Cooper, T. E., Carl, D. R. & Armentrout, P. B. Hydration Energies of Zinc(II): Threshold Collision-Induced Dissociation Experiments and Theoretical Studies. *J. Phys. Chem. A* **113,** 13727–13741 (2009).

228. Rudolph, W. W. & Pye, C. C. Zinc(II) hydration in aqueous solution. A Raman spectroscopic investigation and an ab-initio molecular orbital study. *Phys. Chem. Chem. Phys.* **1,** 4583–4593 (1999).

229. Pye, C. C., Black, S. M. & Rudolph, W. W. An Ab Initio Investigation of Zinc Bromo Complexes. *J. Solution Chem.* **40,** 1932–1954 (2011).

230. Pye, C. C., Corbeil, C. R. & Rudolph, W. W. An ab initio investigation of zinc chloro complexes. *Phys. Chem. Chem. Phys.* (2006). doi:10.1039/b610084h

231. Parchment, O. G., Vincent, M. a. & Hillier, I. H. Speciation in Aqueous Zinc Chloride. An ab Initio Hybrid Microsolvation/Continuum Approach. *J. Phys. Chem.* **100,** 9689–9693 (1996).

232. Harris, D. J., Brodholt, J. P. & Sherman, D. M. Zinc Complexation in Hydrothermal Chloride Brines: Results from ab Initio Molecular Dynamics Calculations. *J. Phys. Chem. A* **107,** 1050–1054 (2003).

233. Karoui, K. *et al.* Theoretical studies of vibrational spectra of [N(CH 3) 4] 2 ZnCl 4− y Br y compounds with y = 0, 2 and 4. *Phase Transitions* **87,** 613–628 (2014).

234. Wopenka, B. & Pasteris, J. D. Limitations to Quantitative Analysis of Fluid Inclusions in Geological Samples by Laser Raman Microprobe Spectroscopy. *Appl. Spectrosc.* **40,** 144–151 (1986).

235. Parlinski, K., Li, Z. Q. & Kawazoe, Y. First-Principles Determination of the Soft Mode in Cubic ZrO_2. *Phys. Rev. Lett.* **78,** 4063–4066 (1997).

236. Hoobin, P. M., Cathro, K. J. & Niere, J. O. Stability of zinc/bromine battery electrolytes. *J. Appl. Electrochem.* **19,** 943–945 (1989).

237. Vogel, I. & Moebius, A. The addition of bromine to quaternary ammonium compounds - basis of the bromine storage in zinc-bromine batteries. *Power Sources* **13,** 237–243 (1991).

238. Jeon, J.-D. D., Yang, H. S., Shim, J., Kim, H. S. & Yang, J. H. Dual function of quaternary ammonium in Zn/Br redox flow battery: Capturing the bromine and lowering the charge transfer resistance. *Electrochim. Acta* **127,** 397–402 (2014).

239. Gomes, A., Viana, A. S. & Silva, M. I. Potentiostatic and AFM Morphological Studies of Zn Electrodeposition in the Presence of Surfactants. *J. Electrochem. Soc.* **154,** 452–461 (2007).

240. Liu, Z., Abedin, S. Z. El & Endres, F. Electrodeposition of zinc films from ionic liquids and ionic liquid/water mixtures. *Electrochim. Acta* **89,** 635–643 (2013).

241. Abbott, A. P. & McKenzie, K. J. Application of ionic liquids to the electrodeposition of metals. *Phys. Chem. Chem. Phys.* **8,** 4265 (2006).

242. Kar, M., Winther-Jensen, B., Forsyth, M. & MacFarlane, D. R. Chelating ionic liquids for reversible zinc electrochemistry. *Phys. Chem. Chem. Phys.* **15,** 7191–7 (2013).

243. Sitnikova, T. G. & Sitnikov, A. S. The Effect of Organic Additives on the Kinetics of Zinc Electroplating. *Prot. Met.* **41,** 607–609 (2005).

244. Boto, K. Organic additives in zinc electroplating. *Electrodepos. Surf. Treat.* **3,** 77–95 (1975).

245. Wilcox, G. D. & Mitchell, P. J. Electrolyte additives for zinc-anoded secondary cells I. Brighteners, levellers and complexants. *J. Power Sources* **28,** 345–359 (1989).

246. Rajarathnam, G. P., Schneider, M., Easton, M. E. & Vassallo, A. M. Electrochemical characterization and comparison of three bromine-sequestering agents for zinc/bromine flow battery applications. in *Asia Pacific Confederation of Chemical Engineering Congress 2015: APCChE 2015, incorporating CHEMECA 2015* 1929–1940 (Engineers Australia, 2015).

247. Burrell, A. K., Sesto, R. E. Del, Baker, S. N., McCleskey, T. M. & Baker, G. A. The large scale synthesis of pure imidazolium and pyrrolidinium ionic liquids. *Green Chem.* **9,** 449–454 (2007).

248. Lockett, V., Horne, M., Sedev, R., Rodopoulos, T. & Ralston, J. Differential capacitance of the double layer at the electrode/ionic liquids interface. *Phys. Chem. Chem. Phys.* **12,** 12499–12512 (2010).

249. Nayana, K. O., Venkatesha, T. V., Praveen, B. M. & Vathsala, K. Synergistic effect of additives on bright nanocrystalline zinc electrodeposition. *J. Appl. Electrochem.* **41,** 39–49 (2010).

250. Vatamanu, J., Cao, L., Borodin, O., Bedrov, D. & Smith, G. D. On the Influence of Surface Topography on the Electric Double Layer Structure and Differential Capacitance of Graphite/Ionic Liquid Interfaces. *J. Phys. Chem. Lett.* **2,** 2267–2272 (2011).

251. Contreras, J. G., López, C. A. & Seguel, G. V. The Raman and IR Spectra of (C 3 H 7) 4 N ZnBr 3. *Spectrosc. Lett.* **18,** 601–607 (1985).

252. Rajarathnam, G. P., Schneider, M., Easton, M. E. & Vassallo, A. M. Electrochemical Performance of Three Novel Bromine-Sequestering Agents for Zinc/Bromine Flow Battery Electrolytes. in *228th Meeting of the Electrochemical Society* (The Electrochemical Society, 2015).

253. Fabjan, C. & Hirss, G. On the kinetics and mechanism of bromine/bromide redox electrodes. *Dechema Monogr.* **102,** 149–161 (1986).

254. Rajarathnam, G. P. & Vassallo, A. M. in *The Zinc/Bromine Flow Battery:*

Materials Challenges and Practical Solutions for Technology Advancement 11–28 (Springer Singapore, 2016). doi:10.1007/978-981-287-646-1_2

255.   Rajarathnam, G. P. & Vassallo, A. M. in *The Zinc/Bromine Flow Battery: Materials Challenges and Practical Solutions for Technology Advancement* 81–97 (Springer Singapore, 2016). doi:10.1007/978-981-287-646-1_6

256.   The University of Sydney. Centre for Sustainable Energy Development - School of Chemical and Biomolecular Engineering - The University of Sydney. (2015). Available at: http://sydney.edu.au/engineering/chemical/research/centre-sustainable-energy-development.